Growth and characterization of II-VI semiconductor nanowires grown by Au catalyst assisted molecular beam epitaxy

Dissertation zur Erlangung des naturwissenschaftlichen Doktorgrades
der Bayerischen Julius-Maximilians-Universität Würzburg

vorgelegt von
Rebekka Christina Pfeuffer
aus Würzburg

Würzburg 2016

Eingereicht am: 19.08.2016

bei der Fakultät für Physik und Astronomie

1. Gutachter: PD Dr. Charles Gould
2. Gutachter: Prof. Dr. Grzegorz Karczewski
3. Gutachter: ...
der Dissertation.

1. Prüfer: PD Dr. Charles Gould
2. Prüfer: Prof. Dr. Grzegorz Karczewski
3. Prüfer: Prof. Dr. Giorgio Sangiovanni
im Promotionskolloquium.

Tag des Promotionskolloquiums: 18.11.2016

Doktorurkunde ausgehändigt am: ...

Contents

ListofAbbreviationsandSymbols

1 Introduction **1**
1.1 Motivation . . . 1
1.1.1 Top-Down and Bottom-Up Approach . . . 1
1.1.2 Nanowire Electronic Devices . . . 3
1.1.3 Nanowire Optoelectronic Devices . . . 5
1.1.4 Nanowire FET Sensors for the Detection of Biological Species . . . 6
1.2 Basic Material Information . . . 9
1.2.1 Crystal Structure of ZnSe . . . 9
1.2.2 The Wide-Band Gap Semiconductor: ZnSe . . . 10
1.2.3 Low Dimensional Objects . . . 12
1.2.4 Molecular Beam Epitaxy . . . 13
1.2.5 Synthesis of Semiconductor Nanowires . . . 15
1.3 ZnSe Nanowires - State of the Art . . . 18

2 Experimental Techniques and Procedures **23**
2.1 Molecular Beam Epitaxy Setup . . . 23
2.2 Reflection High Energy Electron Diffraction . . . 25
2.3 Scanning Electron Microscopy . . . 26
2.4 Transmission Electron Microscopy . . . 27
2.5 Photoluminescence . . . 28
2.6 Transport . . . 30

3 Results: Formation of Catalyst Nanoseeds **35**
3.1 Deoxidation of GaAs:Si . . . 35
3.2 The Au-Ga Catalyst Particle . . . 37
3.3 Density and Diameter of Au-Ga Nanoseeds . . . 39
3.4 Ga Free Au Catalyst Particles . . . 43
3.5 Effects of Elemental Flux on Au-Ga Nanoseeds . . . 44
3.6 Redistribution of Nanoseeds at the Growth Start of ZnTe Nanowires . . . 47
3.7 Nanoseeds Formed with an Amorphous Te or Zn Layer . . . 51

4 Results: Morphology of ZnSe Nanowires **55**
4.1 Influence of the Growth Process on the Morphology of ZnSe Nanowires . . 55
4.1.1 Diameters and Densities of Nanoseeds and Diameters and Densities of Nanowires 56
4.1.2 Influence of the Growth Temperature on the Morphology of ZnSe Nanowires 58
4.1.3 Influence of the Zn to Se Flux Ratio on the Morphology of ZnSe Nanowires 59
4.1.4 The Control of the Morphology of ZnSe Nanowires with Regards to the Growth Rate, Growth Time and Substrate Orientation 61
4.2 Crystalline Quality 63
4.2.1 Singularization of the Nanowires 64
4.2.2 Transmission Electron Microscopy Investigations on ZnSe Nanowires 65

5 Optical and Transport Investigations of Single ZnSe Nanowires **69**
5.1 Optical Investigation of ZnSe Nanowires 69
5.1.1 Photoluminescence Spectrum of Embedded (Zn,Cd)Se Quantum Dots in As-Grown ZnSe Nanowires 70
5.1.2 Photoluminescence Spectrum of Embedded (Zn,Cd)Se Quantum Dots in Single ZnSe Nanowires 71
5.1.3 Photoluminescence Excitation Spectrum of Single Nanowire Quantum Dots 74
5.1.4 Time-Dependent Quenching of Quantum Dot Photoluminescence in Polytypic ZnSe Nanowires 76
5.2 ZnSe Nanowires for Transport Measurements 78
5.2.1 Coordinate Systems to Localize the Single Nanowires 78
5.2.2 Contacts on Single Nanowires 80
5.2.3 Transport Measurements 81

6 Summary **85**

Zusammenfassung

Bibliography

Publication

Danksagung

List of Abbreviations and Symbols

0D	zero-dimensional
1D	one-dimensional
2D	two-dimensional
3D	three-dimensional
a_0	lattice constant
Ag	silver
Al	aluminium
ALE	atomic layer epitaxy
Ar	argon
As	arsenic
Au	gold
Be	beryllium
C	carbon
CCD	charge-coupled device
Cd	cadmium
CdS	cadmium sulfide
CdSe	cadmium selenide
CdTe	cadmium telluride
CMT	cadmium mercury telluride
CT	cadmium telluride
CVD	chemical vapor deposition
cw	continuous wave
DC	direct current
DOS	densities of states
EELS	electron loss spectroscopy
EDX	energy dispersive X-ray
fcc	face-centered cubic
FET	field effect transistor
Ga	gallium
GaAs	gallium arsenide
GaMnAs	gallium manganese arsenide
GaP	gallium phosphide
H_2O	water
HAADF	high-angle annular dark field

HF	hydrofluoric acid
HgTe	mercury telluride
HRTEM	high-resolution transmission electron microscopy
I	iodine
In	indium
InP	indium phosphide
LED	light emitting diode
LPE	liquid phase epitaxy
MBE	molecular beam epitaxy
Mg	magnesium
Mn	manganese
MOVPE	metal organic vapor phase epitaxy
N_2	nitrogen
Ni	nickel
PBN	pyrolytic boron nitride
Pd	palladium
PL	photoluminescence
PLE	photoluminescence excitation
PMMA	poly(methyl methacrylate)
PVD	physical vapour deposition
RHEED	reflection high energy electron diffraction
SAED	selected-area electron diffraction
Se	selenium
SEM	scanning electron microscopy
SiO_2	silicon dioxide
STEM	scanning transmission electron microscopy
Te	tellurium
TEM	transmission electron microscopy
Ti	titanium
UHV	ultra high vacuum
VLS	vapor liquid solid
VSS	vapor solid solid
VPE	vapor phase epitaxy
WZ	wurtzite
XPS	X-ray photoelectron spectroscopy
ZB	zinc blend
Zn	zinc
ZnI	zinc iodide
ZnSe	zinc selenium
ZnTe	zinc tellurium
ZnMnSe	zinc manganese selenide

Chapter 1

Introduction

1.1 Motivation

Nowadays NWs are studied both for fundamental research and for potential device applications. They offer advantages in various areas of science and technology ranging from electronics, optoelectronics, and energy to healthcare. Regarding to their diameter and geometry, the crucial task of this topic for the basic chemistry and physics research is that NWs are on the one hand fabricated with controlled dimensionality and size and on the other hand it is important to find out the intrinsic and potentially unique physical properties of them. To fabricate NWs with controlled dimensionality and size two approaches, the top-down and the bottom-up approach, showed up in recent researches. With these two approaches it is possible to control the particle size, the particle shape, the size distribution, the particle composition and the degree of particle agglomeration. These approaches can be used in gas, liquid, supercritical fluids, solid states, or in vacuum. The advantages and disadvantages of these two approaches are illustrated next in this section before a view NW electronic devices are presented.

1.1.1 Top-Down and Bottom-Up Approach

The meaning of top-down in general is analogous to making a stone statue. A bulk piece of material is modified by carving or cutting as long as it has the desired shape. The general meaning of bottom-up, on the other hand, is building a house with a lot of building blocks.

As already mentioned, in nanotechnology these two approaches are used for creating small objects. The basis of the top-down approach is a bulk material, which is patterned into small features by cutting, milling and shaping. This is done with a combination of various types of lithographic techniques, such as photo-, ion beam-, electron- or X-ray-lithography, etching and deposition. Since now the top-down approach has been successful in many sectors, for example, in microelectronics. This approach is used to form functional devices and their integrated systems, for example, in the miniaturization of computer chips. Furthermore, it is used for the fabrication of quantum well lasers and high-quality

optical mirrors. The top-down approach involves material wastage and actual studies show that the resolution of this approach is limited by lithography. To avoid the limits and the scientific challenges of the top-down approach, like making nanostructures with near-atomic perfection and incorporating materials with distinct chemical and functional properties, the bottom-up approach is a central theme nowadays.

The basis of the bottom-up process is constructing structures by adding atom by atom in a controlled way. The advantages of this process compared to the top-down process are the fact that the wastage is less and that this approach is not limited by the resolution of lithography but rather in how big the structures can be made. Chemical synthesis, self-assembly and molecular fabrication are examples for a bottom-up approach. In this work a kind of self-assembly, which occurs when components spontaneously come together to form ordered nanoscale structures, for instance in the formation of NWs, is used. In the case of the formation of NWs the bottom-up approach has another advantage. With the bottom-up approach it is possible to dope the NW heterostructure in-situ directly during growth. This is compared to conventional doping methods, such as diffusion and ion implantation, an advantage of the top-down approach, because of the high aspect ratio of the ZnSe NWs. In general and due to their high aspect ratio these NWs are somehow the most attractive building blocks for the bottom-up approach. The bottom-up approach limits the critical dimension, the nanowire diameter, not by lithography precision. The diameter of the NWs is controlled during chemical synthesis with atomic resolution. Furthermore, it is possible to realize axial and radial heterostructure NWs as well as branched NWs. Because of that, it is possible to create new device concepts and functional systems and it will be possible to combine chemically distinct nanoscale building blocks.

Radial heterostructure NWs are NWs, which have a radial shell of different material along the radial direction. These NWs are called core-shell NW structures. The heterointerface of these NWs is parallel to the wire axis and their shell is formed under bulk-like conditions. One advantage of core-shell heterostructure NWs is that they can be tailored through band structure engineering to provide better electrical and optical properties. For example, it is possible to realize an one dimensional electron and hole gas by choosing a core and a shell material with appropriate band alignment [Lu 05]. Using these properties it is possible to realize novel phenomena and high-performance transistors. Furthermore, with bandstructure engineering and modulation doping, for example, it is possible to obtain high-efficiency light-emitting diodes [Qian 05], [Qian 04]. Complex core-shell NWs are, for example, the basis of high-performance coaxially gated nanowire FET devices.

Axial heterostructure NWs are NWs, which consist of sections of different material with the same diameter. Dependent on the thickness of the NW it is possible to combine non-lattice-matched materials, due to efficient strain relaxation. The heterointerface of axial heterostructure NWs is perpendicular to the wire axis and the band gap can be tuned locally along the length of the NW to form tunnel-barrier and quantum-confined structures, like quantum dots and superlattices. Axial heterostructure NWs are formed during the NW growth itself with a reaction with the catalyst by switching the materials. They are used as novel thermoelectric devices [Li 03] or simply as quantum dot devices

[Thel 03], [Thel 05]. The quantum dot devices reveal the advantage that strain due to lattice mismatch can relax, to a certain extent, through sidewall elastic deformation, which would allow more freedom in choosing the quantum dot height. This is used to tune the emission wavelength. The second advantage of these heterostructures is that the NW geometry eliminates the problem of the wetting layer, which normally represents an efficient thermal escape route for the confined carriers. Unusual electrical and optical properties can be potentially obtained by the synthesis of NWs with a high degree of structural complexity. Very complex NW structures like branched and tree-like NW structures are used for optoelectronic devices [Kind 02], [Keem 04], [Park 04], [Kone 04], field effect transistors [Arno 03], [Park 05], ultra-sensitive nanoscale gas sensors [Arno 03], [Li 04], [Wan 04], [Wang 05], [Fan 05] and filed emitters [Lee 02], [Jo 03]. To implement these NW-based structures into future devices and to test novel fundamental properties the key requirement on these structures is a high control of the modulation of composition and doping.

If this is realized, electronic or optoelectronic NW devices reveal peculiar and interesting properties [Yan 11], [Jie 10], [Hoch 10], [Chua 13] and they are promising building blocks for high-efficiency and high-integration device applications [Fan 08], [Nguy 10]. They are ,for example, used for field effect transistors [Wu 10], photodetectors [Jian 07], solar cells [Tian 07] and sensors [Jie 06]. The variety of applications of semiconductor NWs is an evidence that devices of semiconductor NWs impact many areas of society, from simple household appliances and multimedia systems to communication, computing and medical instruments. To get a better impression of this topic a few detailed examples of NW device applications are given next.

1.1.2 Nanowire Electronic Devices

Nanowire electronic devices are in most cases diodes, transistors and logic gates. Already more than ten years ago in 2001 Huang *et al.* reported that well-defined semiconductor NW building blocks are used for functional device elements and element arrays in [Huan 01]. They studied the electronic properties of crossed p-Si/n-GaN junctions.

A SEM image of such a crossed NW device is shown in the inset inside the top right inset of Fig. 1.1A [Huan 01]. The current-voltage measurements of these structures exhibit that their current rectification characteristics are comparable with those of p-n diodes with a typical turn-on voltage of about 1.0 V. Most of the investigated devices in the low turn-on voltage range show turn-on voltages between 0.6 V and 1.3 V, indicated by the green cross-hatched area in Fig. 1.1A. The top left inset of this Fig. 1.1A shows the corresponding histogram of turn-on voltages for over 70 crossed NW devices. The red cross-hatched area of Fig. 1.1A marks high turn-on voltage devices. The distribution of these turn-on voltages is broad and lies generally in the range of 5 V to 10 V. The top right inset of Fig. 1.1A is an example of an $I-V$ response for low, marked in green, and high, marked in red, turn-on voltage devices.

Based on the results of the crossed NW device elements Huang *et al.* also explored the properties of integrated p-n junction arrays [Huan 01]. Fig. 1.1B shows an $I-V$

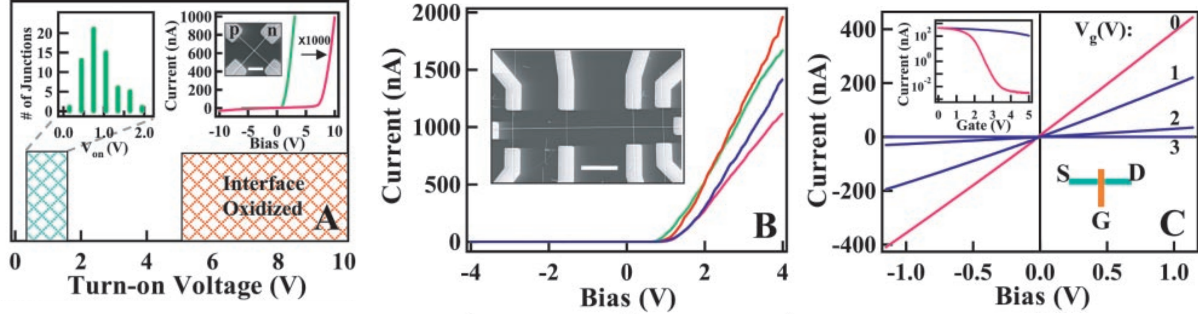

Fig. 1.1: A crossed NW device element of Huang *et al.* [Huan 01]. A) Turn-on voltage distribution for crossed NW device elements. The green cross-hatched area indicates low turn-on voltage junctions and the red cross-hatched area high turn-on voltage junctions. The top left inset is a histogram of turn-on voltages for over 70 samples. The top right inset is the $I-V$ response for low and high turn-on voltages with a SEM image of such a device. B) $I-V$ characteristic of a multiple junction array with the SEM image of this junction in the inset. The different curves are the responses for the four junctions of the SEM image. C) Gate-dependent $I-V$ characteristic of a crossed NW-FET with the corresponding I versus V_{gate} characteristic and the measurement configuration.

characteristic and a SEM image of a typical 4 by 1 crossed p-Si/n-GaN junction array. The four curves of different colors represent the $I-V$ response for each of the four junctions. These crossed NW p-n devices are the first step to create more complex devices like logic gates.

But not only the low turn-on voltage diodes are important electronic devices, high turn-on voltage p-n junctions are also of great interest. Huang *et al.* used high turn-on voltage p-n junctions as nanoscale FETs [Huan 01]. For example, they formed a p-channel FET with a nanoscale conducting channel and a nanoscale gate from a n-GaN/p-Si crossed NW structure. The gate-dependent $I-V$ characteristic of such a crossed NW-FET is shown in Fig. 1.1C. The different gate voltages are indicated 0 V, 1 V, 2 V and 3 V. The measurement configuration of these measurements is shown in the bottom right inset. The top left inset is an I versus V_{gate} characteristic for n-NW gates shown in red and global back gates shown in blue. The bias is set at 1 V.

With these NW device elements they have the possibility to investigate diode- and FET-based logic. For example, the NW logic OR gate is realized by using a crossed p-n junction array of two p-Si NWs and one n-GaN NW. A schematic, a SEM image and the symbolic electronic circuit of this array is shown in Fig. 1.2A. The two p-Si NWs are used as inputs and the n-GaN NW is used as the output. The graph in Fig. 1.2B exhibits the output voltages versus the four possible logic address levels and the inset illustrates the output-input $(V_o - V_i)$ voltage response. This device reveals that the output is low if both input voltages are low and it is high if one or both of the input voltages are high. If one input is set low the $(V_o - V_i)$ voltage response exhibits that V_o increases linearly with V_i, red curve in the inset of Fig. 1.2B. The blue curve in this inset shows that the output is constant high if the second input is high. Fig. 1.2C summarizes the input and output

response and confirms that the discussed NW device operates as a logic OR gate.

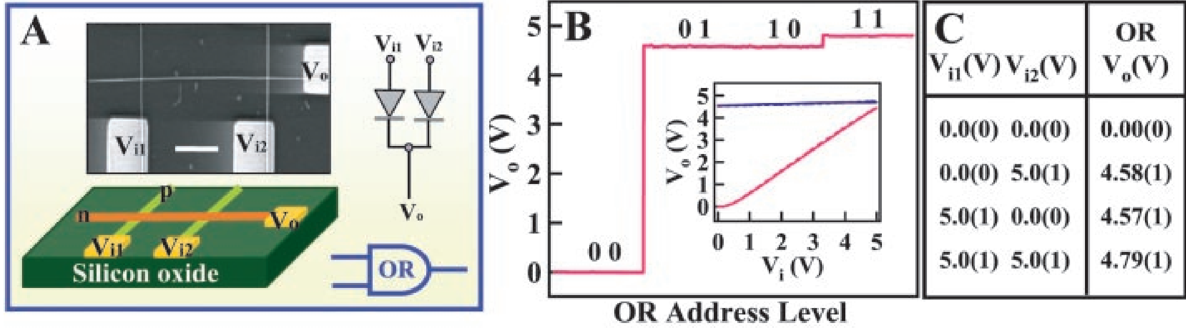

Fig. 1.2: Or gate device of Huang *et al.* [Huan 01]. A) Schematic, SEM image and symbolic electronic circuit of a logic OR gate. It is constructed from a 2 by 1 crossed NW p-n junction. B) Characteristic of the output voltage versus the four adress level inputs: (0,0), (0,1), (1,0), (1,1). C) Experimental truth table for the OR gate.

1.1.3 Nanowire Optoelectronic Devices

Not only NW electronic devices but also NW optoelectronic devices play a crucial role in the trend of miniaturization in technology. In recent years, NW lasers have been attracting intensive attention for both fundamental research and technological applications ranging from optical sensing, signal processing, and on-chip communications to quantum optics.

Duan *et al.*, for example, investigated in one of their reports a NW electrical injection laser [Duan 03]. A cross section of this laser is illustrated in Fig. 1.3a. The laser device is assembled of a CdS NW on a heavily p-doped planar substrate and on top of the CdS NW is a Al_2O_3 layer and a Ti/Au layer. To investigate the emission output from the device one end of the NW is left uncovered. An optical and an electroluminescence image of this device is shown in Fig. 1.3b. The arrow in the optical image marks the end of the CdS NW which will be exposed. In the electroluminescence image marks the arrow the emission from the end of the CdS NW and the dashed line marks the NW. Fig. 1.3c shows a graph where the emission density is plotted against the injection current. At about 90 μA reveals the emission an initial increase in the intensity and at about 200 μA the increase in the intensity is more rapid and highly nonlinear. This highlights the onset of the lasing. The graph in the inset in Fig. 1.3c shows the current versus voltage characteristic of this device. Fig. 1.3d shows the corresponding electroluminescence spectra of the NW end. The red curve exhibits the electroluminescence spectra obtained with injection currents of 120 μA and the green curve exhibits the electroluminescence spectra obtained with injection currents of 210 μA. The red curve shows a broad peak which is consistent with spontaneous emission and the green curve exhibits that the spectrum of the NW end emission collapses into sharp peaks above 200 μA. The sharp peaks are limited and they have an average spacing of about 1.8 nm. The average spacing of the peaks is consistent with Fabry-Perot cavity modes, with regards to the length of the NW device. The green emission spectrum shows a dominant emission with a linewidth of 0.3 nm at 509.6 nm.

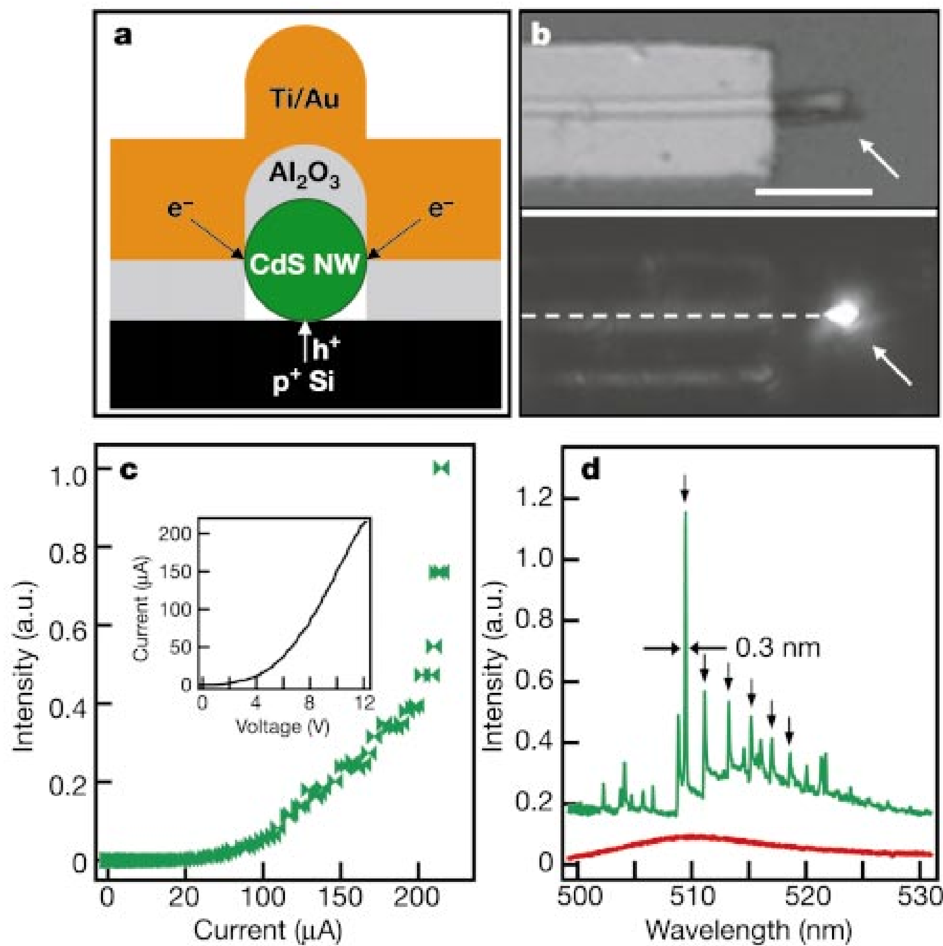

Fig. 1.3: NW electrical injection laser of Duan *et al.* [Duan 03]. a) Schematic of a NW electrical injection laser. b) Optical images of a NW electrical injection laser. c) Characteristic of the emission intensity versus the injection current and the corresponding current versus voltage characteristic. d) Electroluminescence spectra of the end of a NW electrical injection laser.

In this case the linewidth is limited by the instrument resolution. To distinguish the two emission spectra the green spectrum is shifted upwards by 0.15 intensity units. These observations are an evidence of the lasing from the NW electrical injection laser at room temperature.

1.1.4 Nanowire FET Sensors for the Detection of Biological Species

NW FET devices are not only used for logic gates they can also be used for the detection of biological species. Si NWs, for example, have a high-performance switching characteristic, which is one of the factors affecting the sensitivity to overcome the sensitivity limitations of previous planar FET sensors. Furthermore, NWs are interesting for sensing because of their 1D morphology. Compared to the surface region of a planar device, binding to the

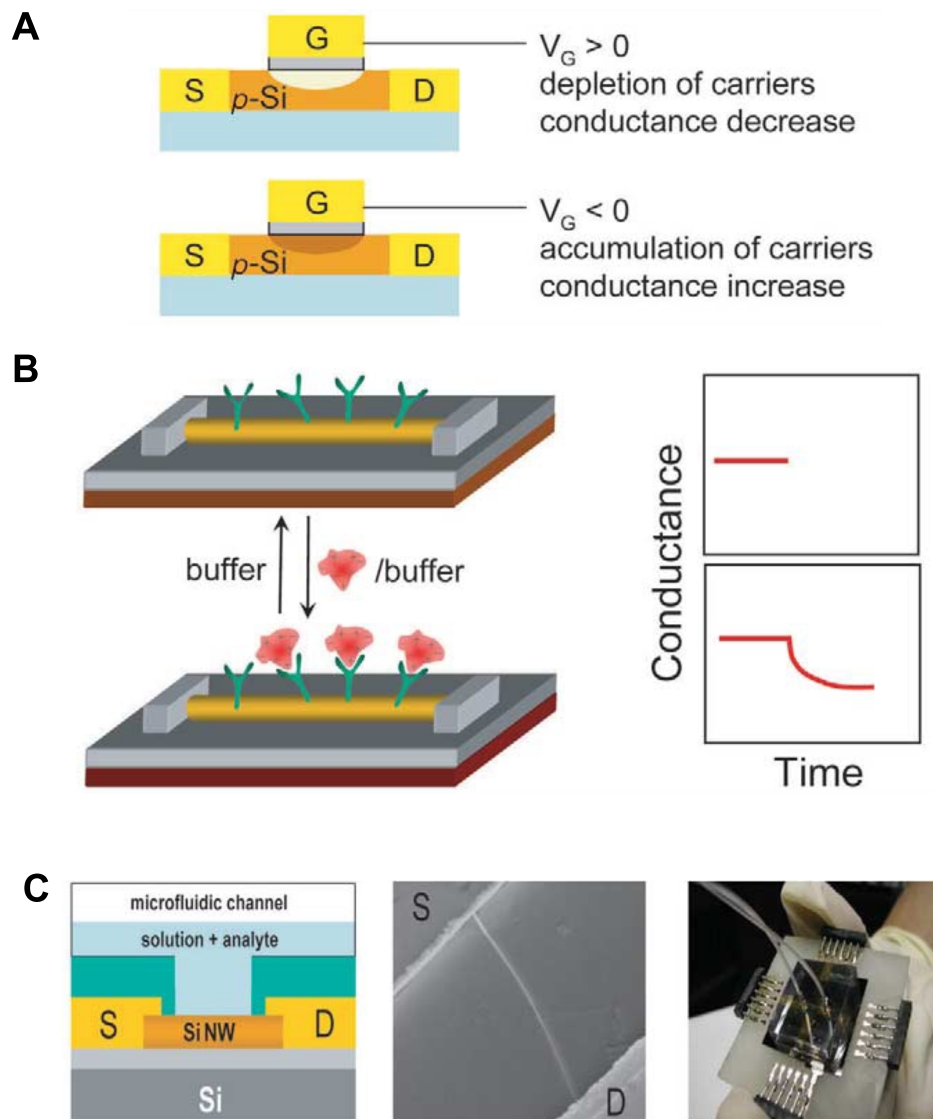

Fig. 1.4: A) Schematic of a planar FET device [Pato 05]. B) Schematic of a NW FET device configured as a sensor with antibody receptors in green and proteins in red [Pato 05]. C) Cross sectional schematic, SEM image and a NW sensor biochip of a NW sensor device [Pato 05].

surface of a NW leads to a depletion or a accumulation of the carriers in the bulk of the NW and increases the sensitivity up to single-molecule detection.

To get an idea of a standard FET, the underlying mechanism of a NW sensor, Fig. 1.4A shows a cross-sectional schematic of a regular planar FET device. The letters S, G, and D correspond to source, gate and drain. In this case the FET is realized with a p-type silicon connected to a metal source and drain electrode. The current of this device is injected and collected through this electrodes and the conductance of the semiconductor is switched with a gate electrode. The gate electrode is coupled via a thin dielectric layer. The schematic in Fig. 1.4A shows, in the case of a p-type silicon, leads a positive gate voltage to a depletion of the carriers and as a consequence to a conductance decrease.

In contrast, a negative gate voltage leads to an accumulation of the carriers and to an increase in the conductance. Instead of planar semiconductors it is also possible to use semiconductor NWs as FET devices.

Fig. 1.4B, for example, shows a schematic of a Si NW based FET device. This device is configured as a sensor with antibody receptors sketched in green. It is illustrated that the sensing or binding of proteins with a positive charge sketched in red leads to a decrease in the conductance.

Fig. 1.4C illustrates a cross sectional schematic of a NW sensor device, an electron microscopy image of a single NW sensor device and a photograph of the corresponding NW sensor biochip. The NW sensor device consists of a NW FET device and a microfluidic device.

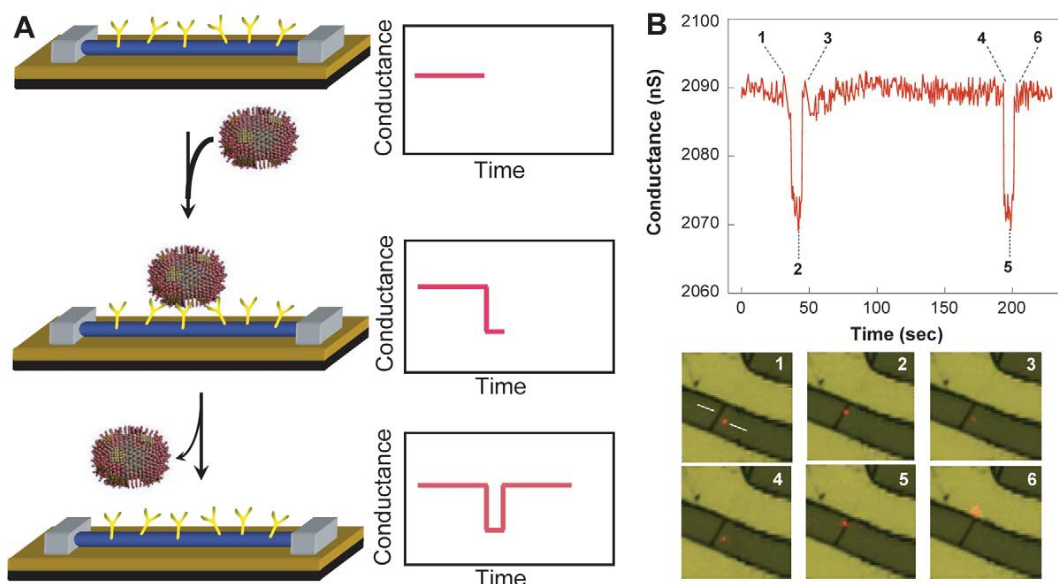

Fig. 1.5: A) Schematic of a single virus binding and unbinding with the corresponding time-dependent change in the conductance. B) The corresponding optical and electrical data [Pato 05].

To define the ultimate sensitivity of such a NW FET Patolsky and Lieber carried out studies of the detection of viruses [Pato 05]. A schematic of the concept of these studies is shown in Fig. 1.5A. The schematic illustrates a single virus binding and unbinding to the surface of a Si NW. The Si NW device is modified with antibody receptors. The graphs on the right side of Fig. 1.5A exhibit the corresponding time-dependent change in the conductance. The schematic in the left upper corner in Fig. 1.5A illustrates the NW device with its antibody receptors without any virus particle. As long as there are no binding virus particles the time-dependent change in the conductance reveals a baseline value. If a virus particle binds to the antibody receptors of the NW device, there is a time-dependent change in the conductance, shown in the middle in Fig. 1.5A. As long as the virus particle binds, the conductance changes compared to the baseline value and it returns to the baseline value as soon as the virus particle unbinds from the NW device,

illustrated in the bottom region of Fig. 1.5 A.

Furthermore, they demonstrated the evidence that the conductance change from the baseline value depends on binding or unbinding virus particles with simultaneous optical and electrical measurements [Pato 05]. Fig. 1.5B shows the corresponding optical and electrical data. The virus appears as a red dot in the optical pictures 1 to 6 in the bottom region of Fig. 1.5B and the electrical data shows well-defined discrete conductance changes when the virus, red dot, reaches the NW device. These discrete conductance changes are marked by the time points 2 and 5. The time points 1 and 3, and 4 and 6 in the conductance data highlight the baseline value of the conductance of the NW device before and after binding. This is the proof that the virus must be in contact with the NW device to get an electrical response. As a consequence the minimum size scale of the NW device depends on the size of the virus. At least they illustrated in their report in [Pato 05] that it is possible to detect multiplexed single-viruses if the Si NW devices are modified with the antibody receptors for specific viruses.

1.2 Basic Material Information

This section addresses the properties and peculiarities of the semiconductor ZnSe and the advantages of 1D systems realized with MBE, such as ZnSe NWs.

1.2.1 Crystal Structure of ZnSe

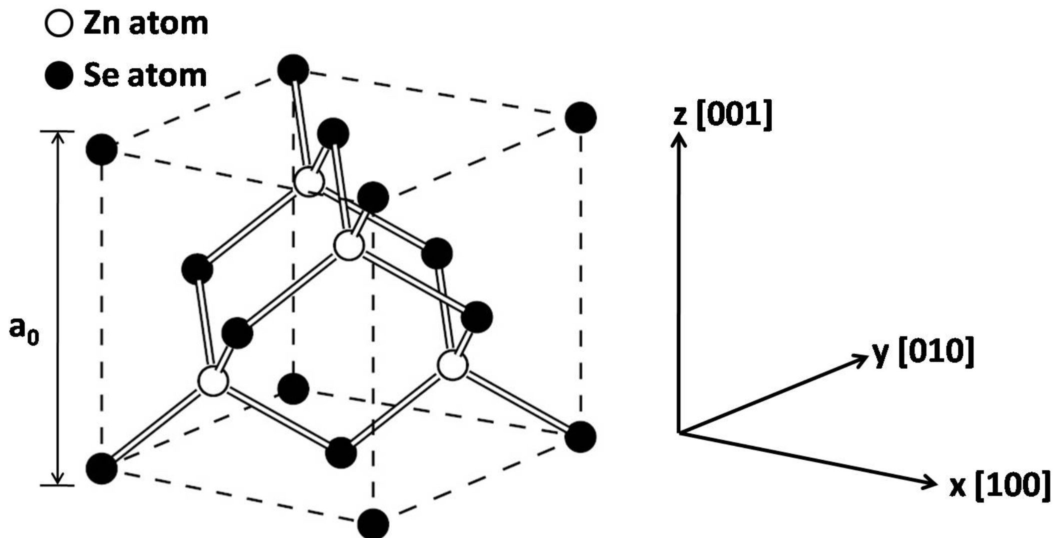

Fig. 1.6: Zinc blend crystal structure of ZnSe. The white spheres are Zn atoms and the black ones are Se atoms. a_0 is lattice constant.

ZnSe is a II-VI compound semiconductor composed of Zn, an element from group II of the periodic table, and Se, an element of group VI of the periodic system. The crystal

structure of the semiconductor ZnSe is a zinc blend crystal structure with a two atomic basis shown in Fig. 1.6.

The zinc blend structure consists of two interpenetrating face-centered cubic lattices, like the diamond structure. The two lattices are displaced to each other with a shift of 1/4 of the face center. In contrast to the diamond structure, where the atomic basis is built of C atoms, the two atomic basis of the ZnSe zinc blend crystal structure consists of alternating Zn and Se atoms. The distance between the atoms is $\sqrt{3}/4a_0$ and a_0 is the lattice constant. The value of the ZnSe lattice constant is 5.6676 Å [Sega 67].

Furthermore, it has to be considered that, each crystal structure is a 3D periodic repetition of an unique arrangement of atoms with a certain symmetric pattern. The directions of the surfaces and planes of these crystals are defined by the so called Miller-Indizes. [hkl] defines the crystallographic direction, [100], for example, defines the x-axes. (hkl) indicates the plane perpendicular to the [hkl] axes. To get a better image of the directions and planes they are shown in Fig. 1.7.

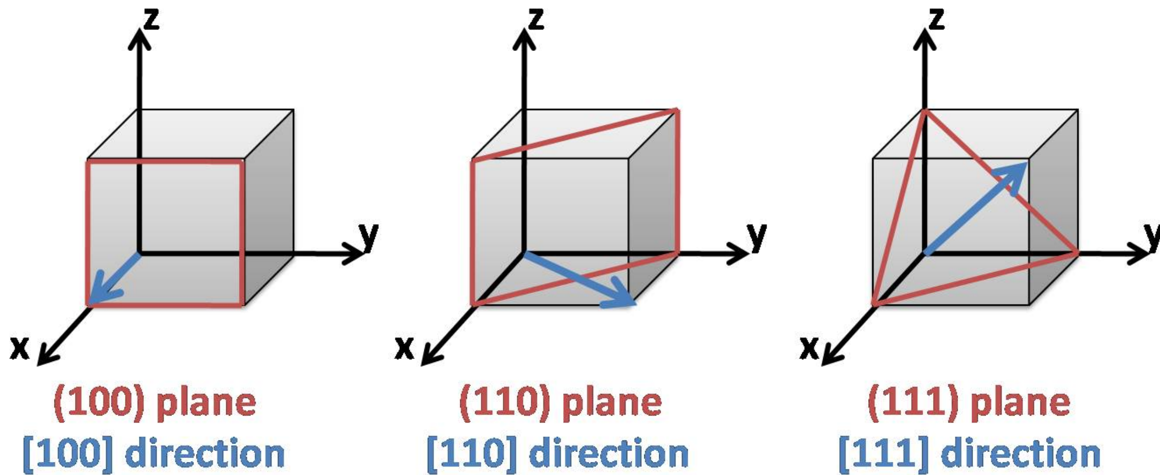

Fig. 1.7: Miller-Indizes of the [100], [110] and [111] direction and the according planes (100), (110) and (111).

In general, the crystal directions, which are shown in Fig. 1.7, influence the physical properties of the investigated material. In the case of the NW growth, for example, the growth direction of the NWs depends on the crystallographic orientation of the used substrate.

1.2.2 The Wide-Band Gap Semiconductor: ZnSe

The II-VI compound semiconductor ZnSe is a solid state with a specific electric conductivity. Depending on the electric conductivity solid states are class divided. There are three classes insulators, semiconductors and metals. The description of the electric conductivity and the corresponding electronic properties of these classes is given by an electronic band

model. This model is a quantum mechanical model and describes the electronic energy states based on an ideal single crystal.

Characteristic for this band structure model is, that the bound states of the electrons of the different classes are confined to a number of intervals of the energy scale. In the case of an ideal single crystal, these intervals are continuous areas which represent the bands of energy. Depending on the considered class there are regions which are energetically forbidden between the bands. The forbidden region is in general between the highest fully occupied band and the next higher one. It is the band gap between the valance band and the conduction band. This band gap characterizes the physical properties of the three classes. If there is no band gap, that means the valance band overlaps the conduction band or the valance band is not fully occupied and the not fully occupied region replaces the conduction band, it is a metal. A semiconductor has a band gap in the range between 0,1 and 4 eV [Kitt 05] and an insulator has a band gap above 4 eV [Kitt 05].

ZnSe, the semiconductor dealt with in this work, has a band gap of 2,70 eV at 300 K and due to that it is a wide-band gap semiconductor. The high energy gap of wide-band gap semiconductors offers devices the ability to operate at higher temperatures than devices created with normal semiconductors with a lower band gap. Another advantage of the devices formed with these semiconductors is that it is possible to realize light-emitting diodes and semiconductor lasers that emit in the visible spectrum or produce ultraviolet emission. As an example, ZnSe has a relatively large band gap in the blue-green spectral region.

Besides the wide-band gap, has the material ZnSe a direct band gap. The minimum of the conduction band is directly above the maximum of the valence band. This is another reason why ZnSe is applied to optoelectronic devices, especially light-emitting devices in the short-wavelength region of visible light.

To manipulate the above mentioned properties, it is possible to add various atoms of different materials to the semiconductor ZnSe. Referred to the electric conductivity, ZnSe can be easily n-type doped with Chlorine or Iodine. P-type doping, however, is a challenge. Iodine, for example, forms a shallow donor state in ZnSe with an ionization energy of 26 meV and carrier densities in the low 1019 cm^{-3} region [**?**], [Shib 88]. But not only the electric conductivity of a semiconductor can be manipulated, it is also possible to influence the lattice constant, the band gap or the magnetic properties. Be, for example, increases the band gap and reduces the lattice constant. This feature is used to grow ZnSe lattice matched on GaAs. The lattice mismatch between ZnSe and GaAs is 0.27 %. Although Be is needed at a certain thickness of the ZnSe layer, this small mismatch makes it possible to grow ZnSe with a high quality on GaAs in heteroepitaxy and it is the reason why we use GaAs substrates for the ZnSe NW growth in this work. A Be concentration higher than 46 % causes a indirect band gap [Chau 00]. Adding Cd to ZnSe shows the opposite effect. It decreases the band gap and increases the lattice constant. This is usefully for optics.

Besides the conductivity and the lattice constant it is possible to influence the magnetic properties of ZnSe. ZnMnSe, for example, is a diluted magnetic semiconductor. Diluted magnetic semiconductors are based on traditional non magnetic semiconductors doped

with a few percent of magnetic elements, usually transition metals instead of electronically active elements. That means a small fractions of the cations of the host crystal are replaced by magnetic ions. In the case of ZnMnSe it is the transition metal Mn, which is incorporated isoelectric as Mn^{2+} Ions. Mn takes the place of a group II atom in ZnSe without doping, so it is not automatically accompanied by a acceptor state like in III-V materials. As a consequence it is possible to vary the magnetic and electrical properties of ZnSe independently of each other.

With regards to the properties of 1D ZnSe NWs not only the material plays a significant role but rather the dimensionality of these structures is important which will be illustrated in the next section.

1.2.3 Low Dimensional Objects

Low dimensional objects are, for example, the ZnSe NWs which are investigated in this work. In general there are four different kinds of dimensional objects, three low dimensional objects, which are zero-dimensional (0D), one-dimensional (1D) and two-dimensional (2D) objects and the three-dimensional (3D) or bulk object. The dimensionality of these objects determines the quantum mechanical properties of the electron gas. Having a n-dimensional electron gas the charge carriers are able to move freely in n dimensions. Depending on the dimensions it is possible to define different densities of states (DOS).

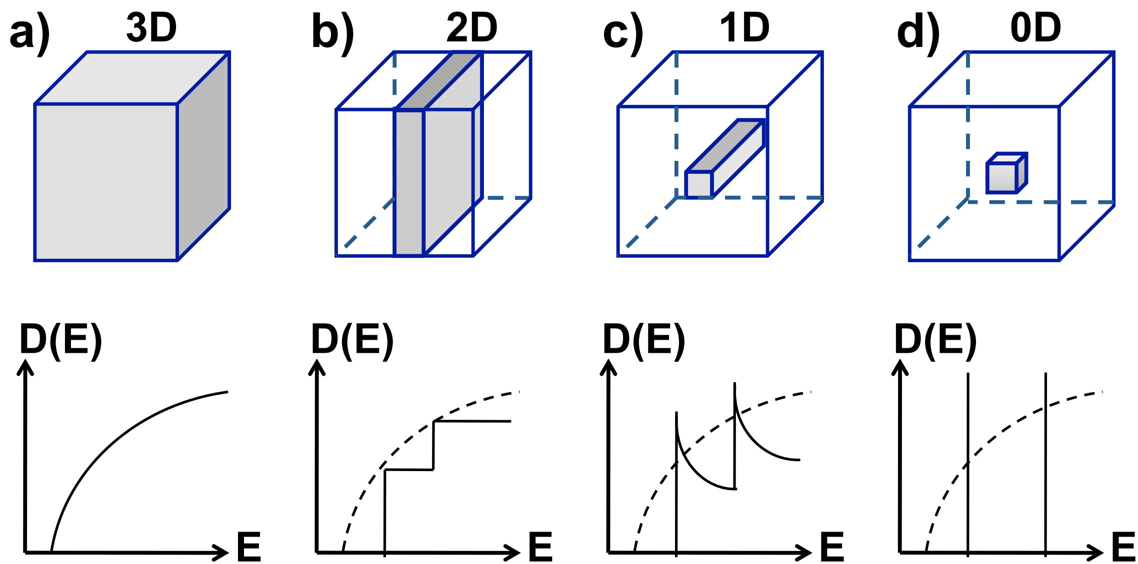

Fig. 1.8: Shape and density of states in 3D, 2D, 1D and 0D objects.

Fig. 1.8 illustrates the shape and the DOS of the electron gas of the different dimensions. Regarding the dimension not only the shape of the nanostructure changes drastically but also the DOS and as a consequence the quantum mechanical properties.

For a 3D system the relation between the DOS $D(E)$ and the energy E is given by $D(E) \propto \sqrt{E - E_C}$ shown in Fig. 1.8a). The energy E_C is the energy of the conduction

band edge. In the case of a 3D bulk system there is a large spectrum of possible energies. Reducing the mobility of the electrons in one dimension leads to discrete energy levels E_i in the limited dimension and the DOS is constant on these energy levels $D(E_i) = const.$. The shape and DOS step function of 2D systems is shown in Fig. 1.8b). Reducing the mobility in a second dimension reveals the following relation between the DOS $D(E)$ and the energy E for single energy ranges E_{ij}: $D(E) \propto \frac{1}{\sqrt{E - E_{ij}}}$. Fig. 1.8c) shows the shape and the DOS of such 1D systems. The DOS shows divergences at the energy positions of the confined states. A quantum dot, like it is shown in Fig. 1.8d) is at least limited to a few nanometers in all directions. The DOS in this case is an array of delta functions. It has values, different from zero only for discrete energies, shown in Fig. 1.8d). To sum up, it is observed that with decreasing dimensions the DOS is concentrated more and more at the band edges. Lower dimensions involve sharper DOS potentials which is an advantage for optical and electronic properties.

However, in spite of the enormous progress made in the development of 2D quantum wells and 0D quantum dots, the study of 1D structures, such as 1D NWs, remains rather behind. 1D NWs are distinguished by their aspect ratio. The length to width ratio of a typical NW exhibits 1000 or more. They are defined as cylindrical structures. The radial size, of such a NW is normally constrained to tens of nanometers or less. That means the NW is limited between 1 nm and 100 nm in two dimensions. The range of this size is equivalent to many physical characteristic lengths, such as the mean free path and the de Broglie wavelength. The third dimension of the NW, the longitudinal size, is unconstrained in the range of several hundred nanometers to a few micrometers, or even longer.

The comparison of the low dimensional systems and the 3D bulk reveals that, as long as the dimension of an object is as large that the electrons behave like free particles, their intrinsic physical properties, such as density, conductivity and chemical reactivity, are independent of their sizes. But, if the size of the nanostructure is comparable to the wavelength of the electrons, the electronic and optical properties change and become size dependent. If the dimension of the nanostructure reaches a certain optimal limit, the exciton Bohr radius, the energy spectrum of the nanostructure changes from continuous to discrete. As a result, the energy band gap becomes size dependent. The NWs investigated in this work reveal this effect if their diameter is below the exciton Bohr radius.

1.2.4 Molecular Beam Epitaxy

To fabricate low dimensional systems in the form of epitaxial layers or bodies there are different technical procedures. These techniques are divided in liquid phase epitaxy (LPE), chemical vapor deposition (CVD) and physical vapor deposition (PVD). Examples for CVD are vapor phase epitaxy (VPE), metal organic vapor phase epitaxy (MOVPE) and atomic layer epitaxy (ALE) and an example for PVD is molecular beam epitaxy (MBE). The basis of all these techniques is epitaxy, a kind of crystal growth which occurs during the growth of crystals on crystalline substrates. Epitaxy requires that at least one crystal-

lographic orientation of the grown crystal corresponds to one crystallographic orientation of the crystalline substrate. That means in the case of epitaxy the created crystal sustains always some information of the substrate.

The technique used in this work is MBE. In contrast to the other mentioned technical procedures, MBE does not need any chemical process. It is an outstanding process because of its precise control of the beam fluxes and the growth conditions.

The basis of the MBE process is its ultra high vacuum (UHV) and the absence of carrier gases, to guarantee the highest achievable purity of the grown material. The UHV conditions avoid any impurities remaining in the chamber and ensure that the mean free path length of the evaporated atoms is big enough, that during growth a beam of atoms reaches the substrate surface directly without interacting with each other or the vacuum chamber gases. The mean free path length λ_{mfp} is given by:

$$\lambda_{mfp} = \frac{k_B T}{\sqrt{2}\pi d^2 p}. \tag{1.1}$$

In this equation is k_B the Boltzmann constant, T is temperature, p is pressure and d is the diameter of the gas particles. λ_{mfp} for UHV is in the order of kilometers.

Furthermore, ensure the UHV conditions inside the MBE system a precise control of the temperature of the effusion cells and the shutters in front of these cells, and as a consequence a precise control of the layer material and the layer thickness down to a single layer of atoms. So it is possible to create multiple layer systems. Thus, the MBE process is mostly used to fabricate crystal films with high quality, it can also be used for self organized growth of structures like quantum dots or NWs. The detailed MBE setup with its several components and the UHV cluster used in this work is presented in chapter 2.

Besides all the requirements the MBE process itself is initiated by ultra-pure source materials which are evaporated from heated effusion cells. The molecular or atomic beams of these effusion cells are characterized by their flux, the number of atoms of the material reaching the substrate surface per time and area. These beams are directed beams of atoms or molecules, that condense on the substrate in the middle of the chamber, which is also heated. The directed beams have a certain energy distribution corresponding to the source temperature. In most cases is the substrate temperature lower than the source temperature and as a consequence lower than the arriving atoms or molecules. This situation reveals a temperature gradient between the arriving atoms and the substrate surface. Because of that, does the MBE process not proceed in thermodynamic equilibrium.

The MBE process is mainly driven by the surface kinematics of the substrate, which are actuated by the energy exchange between the arriving atoms and the atoms of the substrate. The interaction between the arriving atoms and the atoms of the substrate take place as long as they are in equilibrium and incorporate into the crystal. These interactions are described with different surface processes. The whole surface processes including diffusion, interdiffusion, nucleation and desorption are shown in a schematic in Fig. 1.9.

The surface processes are on the one hand the adsorption of the constituent atoms or

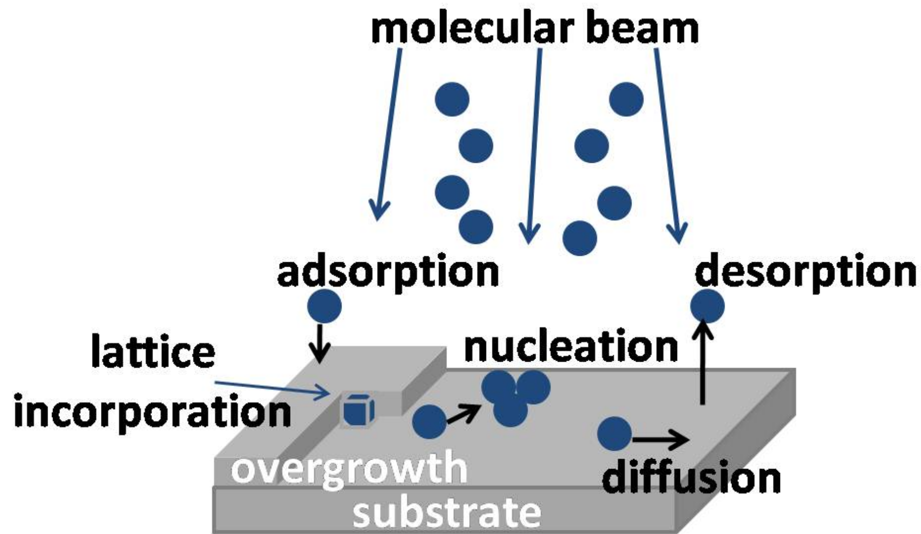

Fig. 1.9: Interactions between the source atoms and the atoms of the substrate during MBE growth [Herm 89].

molecules binding on the substrate surface and the surface migration and dissociation of the absorbed molecules and on the other hand the thermal desorption of the molecules which are not incorporated into the crystal lattice site. The important interactions of these surface processes for the crystal growth are the diffusion of the atoms along the substrate surface until they reach a step edge and the accumulation of the atoms. Depending on the diffusion and the nucleation of the atoms three different growth modes are distinguished. These growth modes are the Frank van der Merwe, the Volmer-Weber and the Stranski-Krastanov growth mode. In the Frank van der Merwe growth mode an atom diffuses along the substrate surface until it reaches a step edge at which it incorporates into the crystal. It is a layer by layer growth. The new layer growth starts as soon as the growth of the previous layer is completed. The Volmer-Weber growth mode describes island growth caused from three-dimensional nucleation and the Stranski-Krastanov or layer-plus-island growth mode is an intermediate process between the last two growth modes. These growth modes are well known and they are simplifications ignoring the growth kinetics. Although these growth modes give an overview over the most common growth procedures, they are not able to describe the whole growth phenomena. For example, they do not describe the growth mode used in this work. The NWs studied in this work are grown by MBE in the VLS growth mode assisted by Au catalysts.

1.2.5 Synthesis of Semiconductor Nanowires

For the NW growth not the MBE process, the epitaxy, but rather the MBE machine itself is used. The growth process in the case of NWs is a catalyst assisted VLS growth mode. This mechanism has been suggested already 60 years ago, in 1964 by Wagner and Ellis, as an explanation for the growth of Si NWs [Wagn 64].

Although the NWs of this work are out of ZnSe grown on a GaAs substrate the used growth mechanism is the same. The single steps of the growth procedure exploited in this work are all done in the UHV cluster presented in chapter 2 and they are illustrated in a schematic in Fig. 1.10.

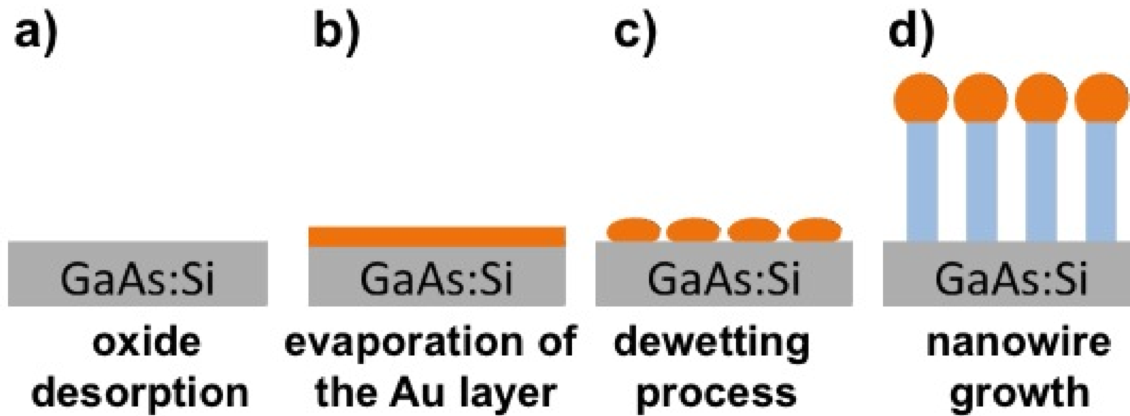

Fig. 1.10: Different steps of the NW growth procedure: a) Removing of the oxide, b) evaporation of the Au layer, c) dewetting process and d) nanowire growth.

The first step of the experimental growth procedure, illustrated in Fig. 1.10a), is to achieve a clean GaAs surface. To get such a clean GaAs surface the oxide layer and the contamination of the Si doped GaAs substrate are removed by heating the substrate up to 640° C. Fig. 1.10b) illustrates the clean GaAs surface with a layer of a high purity Au film on top. This Au film is a few nanometers thick and evaporated on the GaAs surface by thermal evaporation in a connected electron beam evaporation chamber. To get the liquid alloy nanoseeds on the GaAs surface shown in Fig. 1.10c) the Au film of Fig. 1.10b) is heated up. This process is called dewetting process. The best results during this work are achieved with a deweeting process at 460° C in the II-VI growth chamber. Detailed investigations on the parameters of this process are revealed in chapter 3. The last step of the growth mechanism, the NW growth itself is illustrated in Fig. 1.10d). This figure shows NWs with a certain length, with the liquid alloy nanoseed on top on a GaAs substrate. To start the NW growth the substrate is cooled down or stabilized at the growth temperature, which is around 460° C, after the dewetting process. Afterwards, the growth is initiated by opening the shutters in front of the heated evaporation cells. The growth process is the so called VLS process, which describes the way of the a priory gaseous atoms, captured by a liquid alloy nanoseed, which diffuse through this nanoseed and crystallize to a NW at the substrate surface. The final length of the NWs depends on the growth time, the growth temperature, which is the substrate temperature, and the Zn to Se flux ratio. Investigations on this topic are discussed in chapter 4.

A precise observation of the above mentioned VLS growth mechanism based on Fig. 1.11 shows that the process consists of four steps, which are consisting with the theory [Wagn 64]. These steps are:

- (1) material transport in the vapor phase from the material source to the substrate,

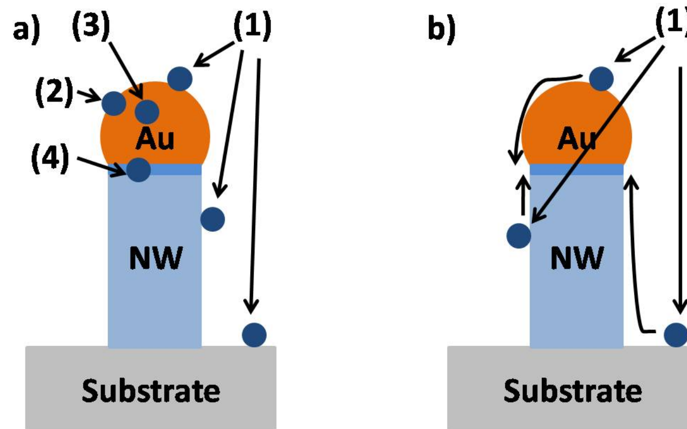

Fig. 1.11: a) Different steps of the VLS mechanism. (1) mass transport in the vapor phase, (2) absorption of semiconductor atoms, (3) diffusion of the atoms through the metal semiconductor alloy, (4) incorporation of the semiconductor atoms in the crystal of the NWs. b) (1) Material transport in the vapor phase and diffusion of the atoms along the substrate surface, the nanowire body and the surface of the nanoseed until they reach the growth front and incorporate into the crystal.

the metal semiconductor alloy surface or the vapor liquid interface,

- (2) chemical reaction on the vapor liquid interface,
- (3) dissolution into and diffusion through the liquid droplet until reaching the liquid solid interface at the growth front,
- (4) precipitation on the liquid solid interface.

The steps can be explained as follows. If the temperature during the VLS growth is above the temperature of the eutectic liquid alloy the atoms from the vapor phase are captured by the liquid alloy. The NW growth starts as soon as the liquid alloy is supersaturated with atoms of the NW material and stops as soon as the concentration of the atoms in the liquid alloy reaches a certain threshold pressure.

Analogue to the NW growth with the VLS growth mechanism above the eutectic temperature of the liquid alloy, it is also possible to grow NWs below the eutectic temperature of the liquid alloy. In that case the growth mechanism is called vapor solid solid (VSS) mechanism. The requirements for this mechanism is also a supersaturation of the atoms of the NW material in the solid catalyst. There should even be a solid mixed phase of the NW material and the catalyst. The topic, if the ZnSe NWs of this work grow in the VLS or the VSS growth mode is discussed in chapter 4.

Besides the question of the growth mode, one should keep in mind that further observations of the growth process of the NWs reveal that the atoms from the vapor phase do not only dissolute at the vapor liquid interface of the liquid alloy and the substrate but also diffuse along the liquid alloy and the substrate surface to the liquid solid interface. This diffusion is illustrated in a schematic in Fig. 1.11b). It seems that the diffusion

of the atoms is not random. Referring to the diffusion, it has to be considered that the activation energy for incorporation at the surface of the crystal is very low compared to the activation energy for incorporation at the volume of the crystal and that the atoms prefer a certain direction while they diffuse. They diffuse along the substrate surface and the surface of the NW to the growth front of the NW. Responsible for this diffusion is the concentration gradient between the substrate surface and the metal semiconductor alloy.

To summarize, there are a few aspects, which have to be considered during the NWs growth. Some of these aspects are shown in the literature review in the next section and some of them are discussed in chapter 3 and 4 in this work.

1.3 ZnSe Nanowires - State of the Art

The interest on NWs increases nowadays because of their novel physical properties. As previously mentioned, ZnSe NWs are promising for building blocks for electronic and optoelectronic devices, as an example. Nevertheless the topic of the growth of the NWs started more than 60 years ago and has even a history. Already during the 1950s it has been discovered that wire growth results from screw dislocations in a substrate via vapor depositions [Treu 75]. Even so more important, for the investigations on NWs today, are the studies of Wagner and Ellis in 1964. In their review [Wagn 64] from 1964 they describe the growth of Si whiskers with the aid of metal impurities, such as Au, Ag and Pd, through the VLS mechanism. They explain the presence of a metal silicon liquid alloy at temperatures higher than the eutectic temperature of this liquid alloy. At this temperature the Si vapor is caught by the liquid droplet. Furthermore, they claim that the interface between the liquid and the substrate is circular and the arising NW has the diameter of this circular.

Wagner and Ellis are the pioneers in the 1D semiconductor NW topic and they started their investigations with the common semiconductor Si. Today the used mechanism for the NW growth, the catalyst assisted VLS mechanism is the same as in 1964, but the variety on the used materials increases. Nowadays there are still investigations on Si NWs but there are also a great number of investigations on NWs of compound semiconductors like III-V or II-VI. The investigations of this work are concentrated on NWs out of the II-VI compound semiconductor ZnSe grown by Au catalyst assisted MBE in the VLS growth mode. These NWs are primarily studied for their optical reasons as it has already pointed out in the motivation of this work and as the following literature report summarizes.

The literature report starts in 2003, when the group of N. Wang of The Hong Kong University of Science and Technology started their studies on ZnSe NWs grown by MBE. They focused on growth on crystalline GaP or GaAs surfaces and they use a ZnSe compound cell for all samples. In their first studies Chan *et al.* observed a large diameter distribution of ZnSe NWs grown directly on a deoxidized GaAs substrate [Chan 06]. Furthermore, they investigated the dependence of the growth direction of the NWs on the diameter of the NWs. Their results reveal that NWs with diameters smaller than 10 nm grew mainly along the $\langle 110 \rangle$ direction on all substrates with the different directions $\langle 001 \rangle$,

⟨111⟩ and ⟨110⟩. Therefore NWs with diameter smaller than 10 nm grow vertically on substrates with the orientation ⟨110⟩. NWs with diameters between 10 nm and 20 nm grow along the ⟨110⟩ or ⟨112⟩ direction on all substrates independent of their direction with a very low defect density. Those, which are thicker than 20 nm, grow along the ⟨111⟩ direction with a large amount of stacking faults.

To explain the dependence of the growth orientation on the diameter of the NWs, observed in the group of N. Wang, Cai *et al.* postulated a phenomenological model based on the minimization of surface and interface energies [Cai 06], [Chan 06]. In this model the NWs are considered as columns with two interface planes and a cylindrical side surface. One of the interface planes is the interface with the catalyst and the other one is the interface with the substrate. The surface and interface energies of this model determine the growth direction of the NWs, when the bulk energy depends on the volume and not on the crystal structure. Additionally, is the surface to volume ratio of these NWs high compared to other object, for example, 2D objects. As long as the NWs are short and the interface between the catalyst and the NW dominates the surface area, they grow in the ⟨111⟩ direction. If the NWs become taller the area of the sidewalls dominates the surface and the advantageous growth direction changes from ⟨111⟩ to ⟨110⟩. The change of the growth direction is based on the minimization of the surface energy at a critical length of the NW. Furthermore, it has to be mentioned that the thickness of the nearly molten area, the area between the NW crystal an the liquid alloy nanoseed, is responsible for the growth direction independent of the discussed model. The thickness of this region depends on the temperature of the substrate during the growth of the NWs. The fact that this area is molten makes it possible that the atoms of the crystal are able to rearrange themselves easily in this area and as a consequence they are able to change the growth direction.

A further observation made by this group is that not only the diameter of the NWs has an influence on the orientation of the NWs also the substrate temperature during growth has an influence. Although the NWs have the same diameter their orientations are different for NWs grown at two different substrate temperatures 390° C and 530° C [Chan 07], [Cai 07]. At least they report that the crystal quality of the NWs consist of a high density of stacking faults and nanotwins at low temperatures [Cai 08].

The reports of the group of N. Wang are in contrast to the observations of Philipose *et al.*. Philipose *et al.* studied ZnSe NWs grown by vapor phase growth and their defect studies show that NWs, which are free of defects are grown in stoichiometric conditions [Phil 08] and at low substrate temperatures [Wang 07].

Back to ZnSe NWs grown with MBE, for example, to the studies of Colli *et al.*, they reveal that ZnSe NWs grown with an excess of Se on an amorphous SiO_2 surface are also randomly oriented [Coll 05]. Nevertheless, the results of Collis group are difficult to compare with the results of N. Wangs group. The results that Colli *et al.* obtain straight NWs with diameters around 10 nm at a growth temperature of $\geq 400°$ C and tapered NWs at $\sim 300°$ C are rather comparable to the results of T. Aichele *et al.* in [Aich 08].

T. Aichele and his group in Grenoble made an enormous progress in the control of the morphology and crystal quality of ZnSe NWs with regards to the optic properties. They

reported on CdSe quantum dots in ZnSe NWs as a source for single photons up to room temperature [Boun 12], [Trib 09], [Aich 09]. To perform such optical studies on ZnSe NWs with a CdSe quantum dot, ZnSe NWs with high crystalline quality are needed. In general, ZnSe NWs are full of stacking faults and it is hard to control the growth of these NWs. To suppress these stacking faults T. Aichele *et al.* developed a growth process with two regimes, which depend on the growth temperature and on the Zn to Se flux ratio.

Low temperature growth or growing under an excess of Zn forms nanoneedles with a wide base and a sharp tip. The sharp tip in this case has a high structural quality in contrast to the wide base. This has its origin due to the fact, that the defects in the nanoneedle are disorientated with respect to the nanoneedle axis. The disorientation hinders the propagation of the defects along the growth direction and because of that the defect zones are blocked on the side walls. In contrast, growing under an excess of Se or with higher temperatures results in long irregular NWs which have a thin uniform diameter over their entire length. These NWs are full of stacking faults because of non ideal growth conditions at the growth start. With the combination of the two discussed growth steps this group achieved mostly defect free ZnSe NWs, which is the basis for a high quality CdSe quantum dot insertion [Aich 08], [Aich 09].

Two years later, also in this group, reported E. Belle-Amalric and M. den Hertog on high quality ZnSe NWs with CdSe quantum dots on ZnSe Buffer layers [Bell 10], [Hert 11a], [Hert 11b], [Bell 12]. The ZnSe Buffer layer reduces the surface roughness [Hert 11a], obtains an epitaxial relation between the substrate and the NWs [Hert 11b] and shields from Ga and As dopants of the substrate [Bell 12]. The suppression of the mentioned effects enables the growth of ZnSe NWs with CdSe quantum dots which can emit single photons up to room temperature [Boun 12]. Besides the advantages of the ZnSe buffer layer for the optical properties of ZnSe NWs, ZnSe NWs grown on a ZnSe buffer layer exhibit homogeneous diameters compared to the large diameter distribution of ZnSe NWs grown directly on a deoxidized GaAs substrates. Further investigations of this group with regards to the ZnSe buffer layer topic, show, that ZnSe NWs, which are grown on a ZnSe buffer layer grow in the vapor solid solid (VSS) growth mode and not in the VLS growth mode [Bell 12].

Concerning the VSS growth mode of ZnSe NWs the group around S. Rubini in Trieste made interesting observations recently. Zannier *et al.* observed in [Zann 14] that the growth mode of ZnSe NWs can be tuned from VLS to VSS based on the interaction among seeds, substrates and beam fluxes. Their studies reveal that ZnSe NWs grown in Se rich conditions are hair like, disoriented and kinked. Contrary to this ZnSe NWs grown in Zn rich conditions are straight and ordered. In [Zann 14] they illustrate XPS measurements on pure Au-Ga eutectic nanoseeds and on Au-Ga eutectic nanoseeds after their interaction with Zn and Se. The results reveal that there is no Ga in the nanoseed after the interaction with Se. Detailed investigations show that Se extracts the Ga atoms of the Au-Ga eutectic nanoseeds and as a consequence the nanoseeds solidify.

Having all the above mentioned studies in mind and especially the work of the group of N. Wang and S. Tatarenko and their difficulties depending on the control of the morphology of ZnSe NWs, this work was initiated in our group in Würzburg in 2011 with the

aim to control the morphology of ZnSe NWs for optical and transport advantages. For optical measurements in most case ZnSe NWs with diameters in a range between 10 nm and 20 nm are used, like it is shown in literature. But to do transport measurements on these thin NWs is very difficult or even impossible, taking into account that the probable depletion layer on the NW surface, a conducting channel in the middle of the wires could not be sufficiently broad enough for electron transport. Based on this fact, the increase and control on the NW diameters becomes the crucial task for the research of this project.

Chapter 2

Experimental Techniques and Procedures

The goal of this chapter is to explain the experimental techniques and procedures used for the realization of this work. First the MBE setup is explained, followed by a description of the in-situ characterization technique RHEED and standard ex-situ characterization setups, such as SEM and TEM. At the end it summarizes the theoretical background of photoluminescence and transport measurements.

2.1 Molecular Beam Epitaxy Setup

The MBE setup used for the growth of the ZnSe NWs in this work is the cluster of the laboratory of the Experimentelle Physik III in Würzburg, which is a two inch wafer system and consists of six different MBE growth chambers, such as a GaAs, GaMnAs, CT, Heusler and two CMT chambers, an electron beam evaporation chamber, a sputter chamber, a X-ray photoelectron spectroscope and a heating station. The whole cluster is under UHV conditions and the single components of the system can be separated or connected from each other with different valves. Furthermore, there are two options to load or unload the samples over an UHV load lock or a nitrogen box. If a sample is loaded into the system there are different possibilities to move the sample in the system. The sample is moved through the systems with grapplers, transport trollies running on a chain and manipulators. At least the growth process itself takes place in one of the different MBE growth chambers, which are connected with the UHV cluster via plate valves.

The UHV conditions of the whole system are generated by different high-speed pumps and cooling shrouds operating with liquid nitrogen. In principle there are two kinds of pumps. One of them are turbo molecular pumps and rotary vane pumps. These pumps transfer the residual gas out of the system and create a residual pressure of 10^{-9} mbar. The other pumps, lowering the pressure further on, are pumps which absorb the residual gas permanent at a surface instead to transferring it out of the system. These are, for example, getter-ion pumps, titanium sublimation pumps and cryogenic pumps. The getter-ion pumps ionize the residual gas, accelerate it in a high voltage field and bind it

at surfaces, for example, out of titanium. Titanium sublimation pumps are pumps, which create from time to time a new layer of titanium on the inner surface of the system, which permanently adheres atoms of the residual gas and cryogenic pumps are pumps, which bond the atoms of the residual gas on cool surfaces. The cool surfaces of these pumps are generated while compressed helium gas expands and quenches a porous activated carbon surface down to 10 K. These pumps reach pressures up to 10^{-11} mbar. This pressure range enables a mean free path length of the atoms of the different materials which is much larger than the dimensions of the system.

The single MBE chambers of the cluster are equipped with different materials. These materials are placed in a boron nitride crucible in effusion cells. The effusion cells are equipped with filaments, to heat the material in the boron nitride crucibles, to create the vapor of the materials for the growth. The incoming power at the filaments regulates the temperature of the cells and the following amount of the material beam. In the middle of the chamber, where the particle beams of the effusion cells should reach the sample, there is a molybdenum block on a substrate holder called manipulator. The manipulator is swiveling and can be heated and rotated during growth. To heat the manipulator it is equipped with a tantalum heater sandwiched by pyrolytic boron nitride discs which provide a homogeneous heat distribution. The temperature is detected with a thermocouple which is placed behind the substrate heater. The distance between the thermocouple and the substrate causes an offset between the measured temperature and the actual sample temperature. Because of that, it is not possible to determine the absolute temperature during growth and the growth parameters are usually relative values. Furthermore, it is possible to interrupt the particle beams by shutters mounted in front of the effusion cells and directly beneath the manipulator, to enable abrupt changes of the material composition. The whole system, that means, the activation of the effusion cells, the shutters in front of them and the heating system at the manipulator is controlled by a computer system to be precise and reproducible.

The amount of effusion cells and their material depends on the kind of the used MBE chamber. The MBE chamber mainly used in this work is the CT chamber, which is a Riber Compact 21 chamber with eight effusion cells with different materials, such as Zn, Te, Cd, Se, Be, Mn, Mg and ZnI. The materials mainly used during this project are Zn and Se.

To analyze the condition in the MBE growth chamber before growth, during growth and after growth there are a few possibilities. The growth chambers are equipped with a quadrupole mass spectrometer, with hot cathode gauges of the Bayard-Albert Type and with a RHEED system. One of the hot cathode gauges of the Bayard-Albert Type is placed at the manipulator to determine the composition of the residual gas and the particle beams of the effusion cells. The RHEED system, explained in the next section, is an in-situ characterization method consisting of an electron gun and a phosphor screen.

At least it has to mentioned that the UHV conditions of the whole cluster demand high requirements on the different components. The seals of the cluster, for example, are out of copper instead of plastic. The advantage in this case is that copper seals have no volatile chemicals, which pollute the UHV system.

2.2 Reflection High Energy Electron Diffraction

As already mentioned Reflection High Energy Electron Diffraction (RHEED) is a common technique used in MBE systems to get in-situ information on the growth process and the crystal structure. The two main advantages of this characterization method are on the one hand the high surface sensitivity and on the other hand the in-situ compatibility with the crystal growth.

The RHEED setup itself requires an electron gun, a flat crystalline sample surface and a fluorescent screen. Furthermore, requires the surrounding and the area of application of the RHEED UHV conditions, so that the electrons exhibit a long mean free path. The energy of the electron beam in the used MBE system is 12 keV and the incidence angle of the beam is $\leq 1°$, to get a high surface sensitivity with a low depth of penetration and to reduce the influence of lattice vibrations. At the end, to get a qualitative information of the crystal surface and its symmetries with the RHEED setup the diffraction patterns on the fluorescent screen have to be observed with the naked eye or a camera setup.

The basis of this method, already indicated by the setup, is the diffraction of high-energy electrons during their total reflection on a crystal structure, which is congruent to the scanning of the reciprocal space. The vertical penetration depth of the electron beam in the substrate is limited to a few monolayers, because of the coulomb interaction between the electron beam and the orbitals of the crystal. Thus, the acquired information are mainly information about the surface structure of the substrate. The mapped diffraction peaks on the fluorescent screen occur due to the periodic structures of the highest crystal layer. The frequency of the periodic structures influences the intensity of each peak.

To get an idea of such a RHEED pattern, Fig. 2.1 compares the RHEED pattern of a sample with a planar 2D surface structure in a) with the pattern of a sample with a 3D surface structure in b).

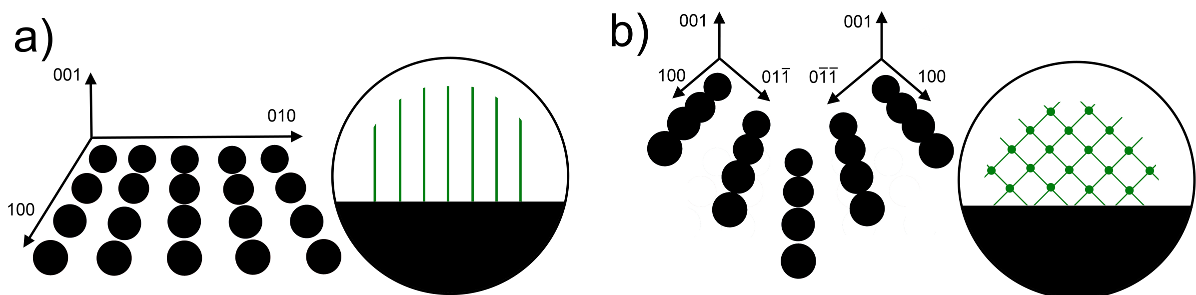

Fig. 2.1: A schematic of the surface structure and the corresponding RHEED pattern of a) a 1D planar sample surface and b) a 3D surface structure. The 3D structure reveals facets which are non parallel to the growth direction [Kess 12].

Fig. 2.1a) shows a pattern of directed lines perpendicular to the substrate surface. These lines reveal the 1D reflection peak and the corresponding higher diffraction orders of a 2D object, such as a crystal lattice. This diffraction is comparable with a diffraction on a multi-slit, due to the fact that the electron distribution of a planar sample surface

consists of many 1D arrays with periodic scatter centers. The number of the directed lines and the distance between them on the diffraction pattern depend on the periodicity of the scatter centers and on the orientation of the sample surface referred to the growth direction.

The sample with the 3D surface structure in Fig. 2.1b) shows a mapped pattern of a crossed lattice with dots. This crossed lattice is built of lines, which are perpendicular to stepped surfaces. Considering that a stepped 3D surface in contrast to a flat 2D surface consists of tilted planar surfaces. In the case of 3D structures the sample surface is rough and the 1D arrays with periodic scatter centers are 2D lattices with scatter centers. The dots in the RHEED signal in Fig. 2.1b) are caused by small objects on the substrate surface. The dots in the RHEED signal appear, thus the small objects on the substrate surface are partially penetrated by the electron beam. So is the 3D information of the real space a 3D diffraction image of the reciprocal space.

Furthermore, it is possible to observe the reconstructions of the sample surface in different directions and to vary the RHEED signal over time, because of the rotation of the sample during the growth process. Due to the fact that the sample is rotated during the growth process in the MBE, it is possible to draw conclusions about the symmetry of the crystal lattice with the periodicity of certain diffraction patterns.

In the case of the growth of NWs, which have side surfaces perpendicular to the substrate, it is possible to determine their number and their orientation with the analysis of the rotating diffraction patterns on the basis of the distribution of the dot shaped RHEED signal. If the NWs are straight during the hole growth process, this analysis is possible as long as the NWs grow, although the lower part of the sample is shadowed during growth and only the upper part of the wires is illuminated by the electron beam. This reveals that also for the NW growth RHEED can be used for real time growth control and the signal on the screen is attributed to the latest grown part of the NW.

2.3 Scanning Electron Microscopy

For analyzing and characterizing the Au-Ga eutectic nanoseeds and the as grown NWs without any preparation as well as the single NWs after singularization a scanning electron microscope is used. It is used to rapidly image the sample to get a first impression. The study of these images is the basis of the control of the morphology of the NWs. Based on the results of these studies elaborated in chapter 3 and in chapter 4 the NWs are used for optical and transport applications. Optical microscopy is not an available option because of the size of the NWs and the resolution of the optical microscopes. The NWs have diameters ≤ 100 nm, the length of the NWs is around 1 μm but the resolution of optical microscopes is fundamentally limited to ~ 200 nm.

To analyze the samples with SEM a focused beam of electrons scans the sample. The electron beam interacts with the atoms in the sample. Different detectors collect on the one hand the electrons which are backscattered from the surface of the sample and on the other hand the secondary electrons which are emitted from excited atoms. The

number of detected secondary electrons depends on the topography of the sample. The secondary electrons are produced in that way that the electron beam ionizes the surface by transferring kinetic energy to conduction electrons. Their very low energy of $\sim$ 50 eV is the reason that they are produced close to the surface within a depth of $\sim$ 10 nm and they are detected before being reabsorbed. They contain not only information about the topography of the sample surface but also about the composition of the structures on the sample surface. The contrast of the image produced with secondary electrons is mostly linked to the topography but it can also translate a chemical contrast in the case of a large change in the atomic number. The images in this work show that the ZnSe NWs with $Z_{Zn} = 30$ and $Z_{Se} = 34$ have a different contrast than the Au-Ga nanoseeds with $Z_{Au} = 79$. Generally the samples are scanned in a raster scan pattern and the image is a combination of the beam position and the detected signal. The resolution of a SEM is normally better than 1 nm.

In this work top view and side view SEM images are used to analyze the investigations done regarding the Au-Ga eutectic nanoseeds and the morphology of the NWs. To receive these images two microscopes are used. The field emission microscope Zeiss Leo 1525 with a acceleration voltage from $\leq$ 1 kV up to 30 kV and the field emission microscope Zeiss Ultra Plus with a acceleration voltage between 0.02 kV and 30 kV.

2.4 Transmission Electron Microscopy

Besides RHEED and SEM there are some more techniques to observe the changes of a crystal on a very small scale. Transmission Electron Microscopy (TEM), discussed in this section is one more of these techniques to analyze materials on the atomic scale, but it is very expensive and time consuming because of the technical requirements.

In contrast to the imaging of the surface of a sample or in the case of this work the imaging of the morphology of the NWs with SEM, TEM obtains crystallographic information. The information on a nanometric scale received with TEM imaging is not only about the crystal structure and the orientation, but also about the types of defects and their locations. Additional to the crystallographic information it is also possible to get information on the chemical composition of the materials on the nanometric scale with the use of electron loss spectroscopy (EELS), High Angle Annular Dark Field Scanning TEM (HAADF-STEM or Z-Contrast Imaging) and Energy Dispersive X-Ray Spectroscopy (EDX).

The basis of the TEM investigations is the transmission. Transmission means to pass through something. Due to this basis the main requirement on the investigated samples is that they are able to transmit electrons. A conventional TEM image is a bright field image and comparable with a shadow puppetry. To get such a image the investigated samples are illuminated with a beam of highly energetic electrons, which transmit the sample. The information of the transmitted electrons are collected with a detector. This is all done in a high vacuum. Depending on the material of the sample some parts stop or deflect the electrons more than other parts. The resulting images have many grey levels.

These grey levels depend on the interaction or scattering of the electrons with the sample. Regions where electrons to not pass through the sample are dark in the image. Regions where the electrons pass unscattered through the sample are brighter.

Although TEM as a characterizing tool is multifaceted with many advantages like, for example, high resolution and high magnification imaging, it has its disadvantages. The main problem as already mentioned is that the measurements are time consuming and the fact that the sample preparation is very delicate.

The TEM studies in this work are carried out with a FEI Titan 80-300 (S)TEM operating at 300 kV. It is equipped with an EDAX energy dispersive X-ray (EDX) microanalysis detector. The investigated NWs were distributed on a holey carbon film supported on a CU grid by gentle scraping of the substrate wafer. All the measurements are done by N. Tarakina.

2.5 Photoluminescence

Another method to study the crystal quality of a material is photoluminescence. It relies on the excitation of the electrons of a material, for example, a semiconductor. The excitation of the electrons can occur thermally with an increasing temperature or non thermal with light. If the electrons are excited with light, they are excited with a laser beam in most cases. The energy of the laser beam should be in the range of the band gap of the investigated material or higher. The laser beam excites the electrons, for example, from the valance band to the conduction band to generate a charge carrier with a remaining hole in the valance band. The number of generated charge carriers depends on the excitation density, the number of photons per time and area, and on factors which are material specific, like the absorption coefficient of each wavelength. With regards to the excitation, it is possible to distinguish between continuous wave (cw) excitation and pulsed excitation. Cw excitation means that there is a balance between charge carrier generation and recombination. Pulsed excitation in contrast means that there is a excess of charge carriers in the semiconductor during the pulse period, which is short compared to the life time of the generated charge carriers. In the illustrated example, the electrons recombine with the holes after relaxation and emit the energy difference, which is in the range of the band gap. There are two possibilities to emit the energy, a non radiative and a radiative. The non radiative emission causes lattice oscillations. The radiative emission emits light which is called photoluminescence.

The radiative emission is caused by different transitions, for example, transitions from band to band, free excitons, bound excitons or transitions from band to impurities. If a electron of the conduction band recombines with a hole of the valance band, it is called band to band transition. Free excitons are quasi particles where a electron of the conduction band is bounded on a hole of the valance band based on the coulomb interaction. Bound excitons are excitons which are localized at impurities of the periodic lattice. Band to impurities transitions are transitions of doped semiconductors. Possible band to impurities transitions are the transition of an electron of the conduction band

to the acceptor level, the transition of an hole of the valence band to the donor level, or the recombination of a donor electron with an acceptor hole. The intensity of these transitions increases with the number of the dopants and it is a size for the strength of the doping. Furthermore, gives the energy of the detected light information about the position of the energy level of the existing defects. To interpret the information about the electronic structure of the material, the emitted photons independent of the transition process are detected with a charge-coupled device (CCD) array, for example.

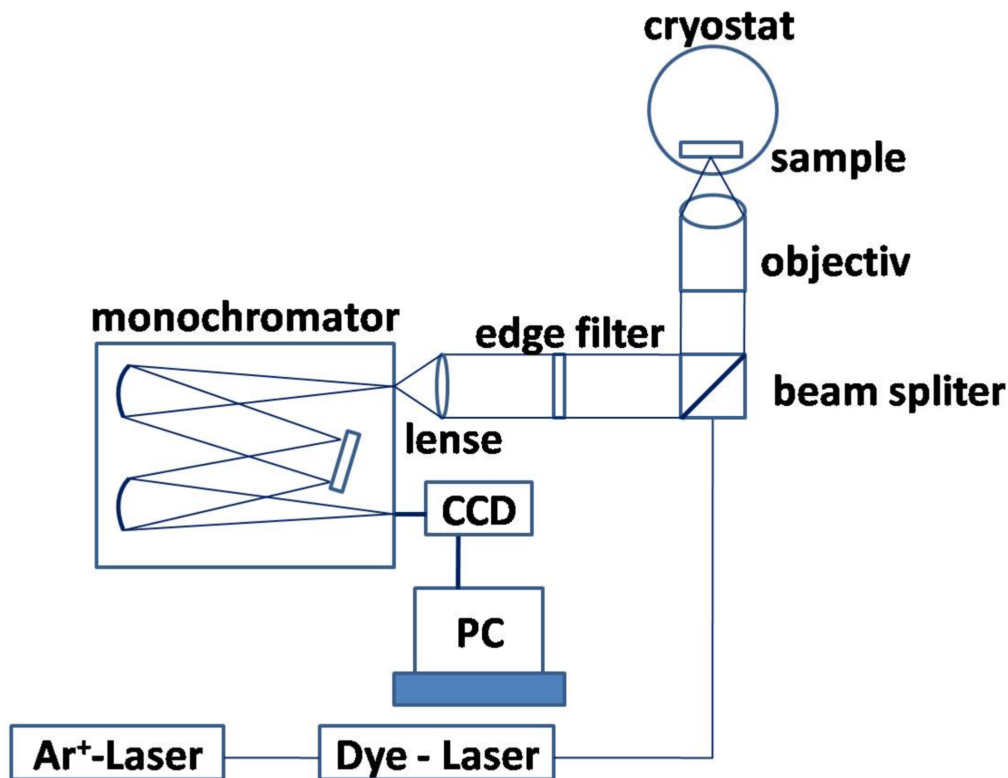

Fig. 2.2: Schematic of the PL measurement setup.

Fig. 2.2 illustrates a schematic of the PL measurement setup used in this work. The sample with the single NWs on top is mounted on the coldfinger of a liquid helium flow optical cryostat. To get a better resolution and to avoid heat stimulated transitions during the measurement the sample is cooled down. Heat stimulated transmission occurs, due to the fact that the line width of the luminescence depends directly on the temperature of the sample with regards to the mean interaction time. The used Stilbene-3 charged dye laser pumped by an Ar^+ laser provides the tunable optical excitation. The output power of the Ar^+ laser is stabilized to within 1 % accuracy by a liquid crystal laser stabilizer. The laser beam is directed to the sample via mirrors and beam splitters. Luminescence is collected in a confocal geometry by a 0.4 numerical aperture microscope objective, spectrally dispersed in an 1 m focal length monochromator equipped with a 1200 mm^{-1} grating, and detected by a liquid nitrogen cooled CCD array. All the photoluminescence measurements investigated in this work are done by S. Bieker of our optics group.

2.6 Transport

To characterize the NWs with regards to their electric conductivity, transport measurements are the characterization method of choice. Transport in solid states is driven by versatile charge carriers with the effective mass m^*. An external electric field causes the movement of these charge carriers. The specific electric conductivity σ of a material is defined as:

$$\sigma = qn_e(T)\mu_e(T) + qn_h(T)\mu_h(T). \tag{2.1}$$

In this equation is q elementary charge, n is charge carrier concentration and μ is the mobility of the charge carriers. The parameters n and μ are functions of the temperature T. The indexes e and h represent negative and positive charge carriers, electrons and holes. The specific resistance is defined as:

$$\rho = \frac{1}{\sigma}. \tag{2.2}$$

The charge carrier concentration $n(T)$ is given by the band structure of a solid state. In the case of semiconductors there is a gap between the valance and the conduction band. The charge carrier concentration depends on the density of states $N(E)$ in the conduction band and on the probability of occupancy, which is described by the Fermi-Dirac statistic $F(E,T)$. At room temperature (300 K) it is approximately the same as the Boltzmann distribution. So, that the charge carrier concentration can be described as follows:

$$n = N_c e^{-\frac{E_c - E_F}{k_B T}}. \tag{2.3}$$

The energy E_c is the edge of the conduction band, E_F is the Fermi energy, k_B is the Boltzmann constant, T is temperature and N_c is the effective density of states of the conduction band. This equation reveals that the charge carrier concentration depends exponentially on the temperature and on the energy difference between the Fermi energy and the edge of the conduction band. The charge carrier concentration can be varied by doping and the temperature dependence of the charge carrier concentration is exponentially. As a consequence it is necessary to avoid heating of the sample during transport measurements. Semiconductors are doped in most cases because of lattice defects or impurities. The density and the energetic position of these doped levels and the temperature of the system determine the charge carrier concentration of the semiconductor.

But, not only the charge carrier concentration also the charge carrier mobility is important for transport measurements and for the charge carrier mobility the external electric field plays an important role. The external electric field accelerates the charge carriers of the semiconductor. The drift velocity of these charge carriers is proportional to the electric field strength E for small field intensities:

$$v_d = \mu E. \tag{2.4}$$

In this equation is μ the constant of proportionality. The linear dependence between the drift velocity and the electric field is reflected in Ohms law $V = R \cdot I$. The movement of the charge carriers depends on different scattering mechanisms and is defined as:

$$\mu = \frac{q\tau}{m^*}. \tag{2.5}$$

Whereas τ is the mean free time between two scattering processes. The mobility increases with the increasing mean free time and the decreasing effective mass m^* and as a function of time decreases the charge carrier mobility with the increasing temperature. If the field strength is to high the drift velocity is non linear and can not be described by Ohm's law anymore.

This is all true for bulk materials, but if transport measurements are done on NWs, it has to be considered, that the mobility of the charge carriers in the NWs is diminished by scattering effects at the NW surface. NWs have a lower conductivity compared to bulk materials which makes the investigations based on transport measurements on 1D NWs so interesting.

Studying the surface of a solid state in general reveals that the atoms at the surface have no neighbors and so called dangling bonds originate. Dangling bonds are unsaturated bonds which are energetic unfavorable. To minimize the surface energy the surface atoms are rearranged. This rearrangement leads to a new electronic structure of the surface which is different to the volume. Furthermore, causes the rearrangement a band reflection at the surface or interface which can lead to a depletion zone. Referred to NWs the whole NW can be depleted if the diameter of the NW is too small. As a consequence it is not possible to measure any transport through the NW body.

The surface states increase the charge carrier concentration like a additional doping on the one hand, and on the other hand they reduce the mobility of the charge carriers because of the higher scattering rate. The order of the change in the conductivity depends on the surface to volume ratio.

Besides the charge carrier concentration and the mobility of the charge carriers the contacts on the NWs play a crucial role for the transport measurements. A contact between a metal and a semiconductor a Schottky contact. If there are no surface states the formation of such a contact can be described with Fig. 2.3 [Sze 69].

The metal in the example in Fig. 2.3 has the work function $q\phi_m$ and the semiconductor is a n-doped semiconductor with the electron affinity $q\chi$. If the metal and the semiconductor are spatially divided the energy scheme is shown in Fig. 2.3 a). Fig. 2.3 b) reveals the state where metal and semiconductor are connected. In this case the Fermi energies are in a thermodynamic equilibrium. Charge carriers of the interface of the semiconductor run into the metal. The negative charge carrier accumulate at the surface of the metal and the positive charge carriers accumulate at the interface of the semiconductor. The charge carrier concentration of the semiconductor is less than the charge carrier concentration of the metal. The needed volume in the semiconductor is bigger than in the metal. The absent negative charge carriers in the edge area with the width W of the semiconductor cause a band reflection. The resulting Schottky barrier, the difference between the work

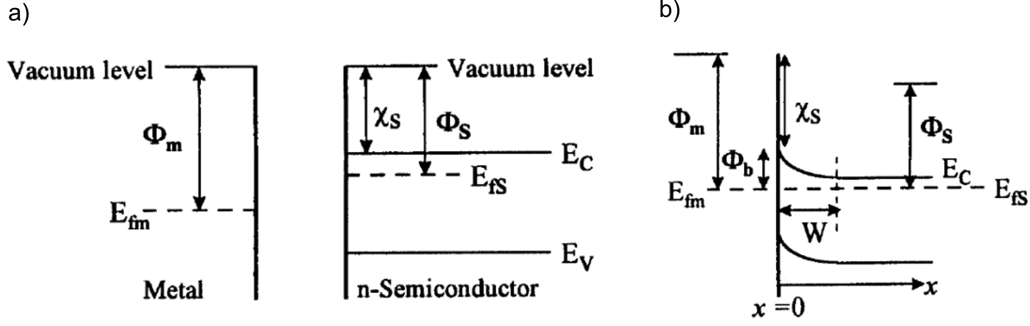

Fig. 2.3: Schematic of the band structure of a metal and a n-doped semiconductor a) before contact and b) after contact [Kim 00].

function of the metal and the electron affinity of the semiconductor is defined as:

$$q\phi_b = q(\phi_m - \chi). \tag{2.6}$$

The simplest structure to do transport measurements on NWs is a two point contact measurement. The characterizing NW is contacted with two metal contacts and a bias voltage is applied. The measured resistance in this system is the sum of the resistance of the two metal contacts and the resistance along the NW. The values of these resistances stick together, which makes it impossible to make a statement concerning the specific contact resistance. Indeed it is possible to estimate the higher limit values of the single components. If the length l and the cross section A of a NW is known the resistance of the NW can be estimated with the following formula:

$$R = \rho \cdot \frac{1}{A}. \tag{2.7}$$

Alternatively, if the contact area is known, the specific contact resistance can be estimated with

$$R_c = \frac{\rho_c}{A_c}. \tag{2.8}$$

The distance between the contacts of the samples investigated in this work is between 100 nm and 600 nm and the diameter of the used NWs is between 10 nm and 100 nm depending on the sample.

If the contacts between a metal and a semiconductor have a non linear asymmetric current voltage behavior with a back and forward direction, they are Schottky contacts. Characteristic for Schottky contacts are the height and the width of these contacts. The quality of these two parameters is the key for good contacts. The height depends on the contact material and the width can be influenced by doping of the material, which should be contacted.

The two point contact measurements done in this work are done with direct current (DC) voltage. A schematic of the used room temperature measurement setup is shown in Fig. 2.4. The sample of these setup is fixed in a chip carrier. The pins of the chip

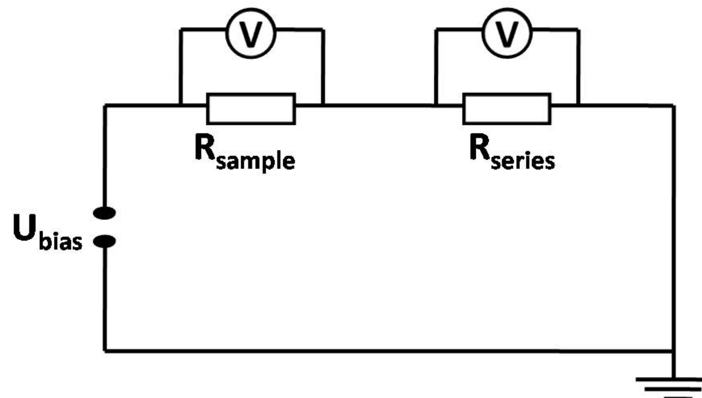

Fig. 2.4: Circuit of the room temperature measurement setup.

carrier are connected with the sample via a wire and these pins are the connection to the measurement setup. Depending on the used connections a measurement setup shown in the schematic of Fig. 2.4 can be realized.

The different measurement setups are controlled with LabView programs. The voltages are displayed by the voltage card of the computer, which has a 16-Bit Interface and a voltage range of ±10 V. The voltage measurements are done with a Agilent digital multimeter. The 1:1 preamplifier of the Agilent digital multimeter has a operating range of ±2 V. The results and measurement values are displayed in a graphic and saved with the LabView program. The potential drop is directly measured at the sample and at an additional series resistance as shown in Fig. 2.4. Based on the potential drop at the series resistance the current is calculated and as a consequence the resistance of the sample is determined. The resistance of the sample is used to determine the conductivity of the NWs and this is investigated and discussed in chapter 5.

Chapter 3

Results: Formation of Catalyst Nanoseeds

The following chapter deals with a detailed investigation on the catalyst nanoseeds of the NW growth. The diameter of these nanoseeds determines the diameter of the investigated NWs. As materials, it is possible to use various metals, such as Au, Ag, Ga or Ni. The most common choice, also used in this work, are catalyst nanoseeds out of Au. These nanoseeds can be generated and deposited by different methods, including generation with electron beam lithography [Mart 04], colloidal particles [Hoch 05] or nanoseeds formed by thermal dewetting of a GaAs surface covered by a thin Au film $\leq$ 10 nm, as applied in this work. The requirements for the formation of the catalyst nanoseeds and various dependencies on different parameters, such as Au layer thickness, dewetting temperature and dewetting time, during their formation, are investigated.

3.1 Deoxidation of GaAs:Si

The NWs investigated in this work are mostly grown on EPI-Ready Si doped GaAs substrates with different orientations (001), (110) and (111)B. Independently of the growth mode the overall start conditions play an important role for the MBE growth, as well as for the NW growth. Because of that, the GaAs:Si surface preparation matters a lot during this project. The used GaAs:Si wafers receive a special surface oxidization already by the producer company, to obtain the same surface conditions for all wafers.

In the case of the growth of NWs starts the GaAs:Si surface preparation with removing the special oxide layer and any chemical contamination. There are different possibilities to get rid of the surface oxide layer. It can be removed with several kinds of etching or through a thermal heating step. In this work two different kinds of heating procedures are investigated.

Related to the heteroepitaxy of ZnSe on GaAs the oxide is removed by thermal deoxidation with a supplied As flux in the III-V chamber. The As flux prevents the thermal degradation of the substrate surface during the heating process. The second way is removing the oxide by thermal deoxidation without any supplied flux in the II-VI growth

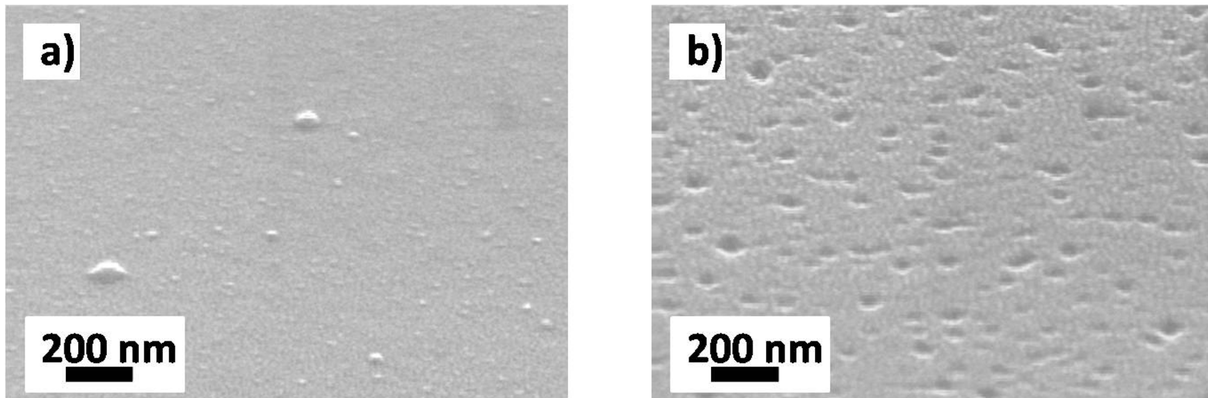

Fig. 3.1: SEM images of the surface of a GaAs:Si substrate after oxide desorption with a supplied As flux (a) and without a supplied As flux (b). To preserve the oxide free surface an 1 nm thick Au layer is evaporated in a connected evaporation chamber after thermal the deoxidation.

chamber.

The SEM images in Fig. 3.1 reveal the surfaces of GaAs:Si substrates after the thermal deoxidation with and without a supplied As flux. An 1 nm thick Au layer is evaporated in a connected evaporation chamber after the thermal deoxidation in both cases.

Fig. 3.1a) presents the SEM image where the oxide is removed with a supplied As flux in the III-V chamber. The first step of this process is heating the GaAs:Si substrate up to a temperature of about 560° C. At this temperature the arsenic cell is opened. Further heating under As flux reveals, with the aid of RHEED observations, that the desorption of the oxide happens at around 620° C in the III-V chamber. After that the substrate is cooled down in As flux to 550° C. Then the As cell is closed and the substrate is cooled down to 200° C. So it can be treated to further experiments in the MBE cluster.

Fig. 3.1b) shows the SEM image of the substrate surface where the oxide is removed by pure thermal heating in the II-VI chamber. In this case the substrate is heated up to around 650° C until the desorption of the oxide happens at around 620° C. This is also observed by RHEED. After the desorption of the oxide the substrate is cooled down to 200° C. At the end it can be treated to further experiments in the MBE cluster as well as the substrate where the oxide is removed under As flux.

The comparison of the two SEM images in Fig. 3.1a) and b) reveals that the substrate surface after the deoxidation with supplied As is smooth and the substrate surface after the deoxidation without supplied As has holes with different sizes. These holes are remarks for the evaporation of As. The evaporation of As starts at a substrate temperature around 550° C. In the case of the deoxidation with supplied As the evaporation is stopped and the As flux prevents that the crystalline quality of the wafer gets worse.

Concerning the growth of NWs it has to be mentioned, that the heating of the sample up to around 550° C without supplied As flux is not finished after removing the oxide. The substrate surface will be damaged again by heating after deoxidation. The addressed process is the dewetting process. It influences the surface of the substrate not only by

heating, but rather with different parameters, which are investigated and discussed in the following sections. Because of that, removing the oxide with additional As or not plays a secondary role for the growth of the NWs.

As a consequence, the oxide removal during this project is mostly done, without supplied As, directly in the II-VI growth chamber. Only, if a ZnSe buffer layer is used for the NW growth, the oxide is removed with supplied As in the III-V chamber.

After the removal of the oxide or the growth of the ZnSe buffer layer the sample is moved in ultra high vacuum through the MBE cluster to the electron beam evaporation chamber. Depending on the application of the produced NWs Au layers with different thickness are evaporated on these samples, before they are transferred in the growth chamber. The theoretical background of the different steps of the NW growth are already explained in detail in chapter 1. The experimental observations concerning the formation of the catalyst nanoseeds are summarized next.

3.2 The Au-Ga Catalyst Particle

As already mentioned for the growth of ZnSe NWs Au-Ga catalyst nanoseeds are used in this work. These nanoseeds are formed on Si doped GaAs substrates, and as illustrated in the last section, the first step to use the Si doped GaAs substrates for the growth of NWs, is to get rid of the oxide layer and any chemical contamination of their surface. If this is done, like it is explained in the last section, the second requirement for the formation of the Au-Ga catalyst nanoseeds is an Au layer. The Au layer is evaporated on top of the oxide free GaAs:Si substrate in a connected metal evaporation chamber.

Afterwards the Au-Ga catalyst particles are formed during a so called dewetting process, where the substrate with the Au layer on top is heated up. During this heating process the thermal energy of the substrate covered with Au increases and the Ga atoms start to diffuse into the Au layer. The occurring Au-Ga eutectic reduces the melting point of the pure Au layer (1064° C) and is getting liquid at a certain substrate temperature depending on the actual composition of the eutectic [Elli 81]. In [Pers 04] it is illustrated that the Ga concentration in the Au layer increases for temperatures higher than 350° C. Above 400° C starts As to escape out of GaAs and causes a degradation of the GaAs surface. Although As escapes out of the GaAs:Si substrate at these temperatures there is no measurable amount of As in the Au-Ga particle. Thus the solubility of As in solid Au is negligible up to 400° C [Owen 45]. In contrast the solubility of Ga increases with increasing temperatures. For a Ga concentration of 7,8 % at 282° C, exhibits the Au-Ga phase diagram different phases [Elli 81], in which the Ga saturation concentration in solid Au increases stepwise or stepless with increasing temperature. Depending on the occurring phase the melting temperature of the Au-Ga layer ranges between 375° C for 26,5 % Ga and 415° C for 22,1 % Ga.

The observed melting point, the point where the Au-Ga film becomes liquid in the system used during this work, is at around 460° C. This point is observed by RHEED as well as the point of the deoxidation of the substrate. The RHEED observations at

the beginning of the dewetting process reveal diffraction spots of rough solid and twinned cubic Au. During the dewetting process the diffraction spots of the solid Au-Ga vanish and the diffraction pattern of GaAs becomes visible, due to the fact that small Au-Ga droplets are formed with uncovered GaAs areas in between.

The separated Au-Ga droplets with different sizes and the uncovered GaAs areas in between occur because of the surface tension of the Au-Ga eutectic mixture. The surface to volume ratio of the so formed Au-Ga nanoseeds depends on their radius. According to this dependence the partial pressure p around the nanoseed is determined by its radius of curvature r. This relation is in principle described with the Gibbs-Thomson effect and the partial pressure can be calculated with the following equation:

$$p = p_{sat} \cdot e^{r_{crit}/r}. \tag{3.1}$$

In this equation is p_{sat} the saturation pressure of the nanoseed material and $r_{crit} = \frac{2\gamma}{k_B T} \cdot \frac{V}{N}$ is the critical radius with the surface energy γ in units of $\frac{J}{m^2}$, with the thermal energy $k_B T$ and the volume of the nanoseed per number of atoms $\frac{V}{N}$ [Moor 90]. This is the basis of the so called Ostwald ripening, describing the time dependent relative volume change of particles with different size [Voor 85]. This description is valid for particles interacting with the surrounding volume. In the case of Au-Ga nanoseeds the partial pressure is not a volume pressure, but a surface pressure. That means, that Ga diffuses only at the surface and does not evaporate into the vacuum depending on its boiling point of 2403° C [Holl 95]. This observation does not change the physical background of this behaviour apart from the dimensionality.

Taking equation 3.1 into consideration reveals that the partial pressure around small nanoseeds is higher than the partial pressure around bigger ones, due to the fact that the radius of curvature is higher for small nanosseds. So occurs a compensating material flux from the small droplet to the bigger one. The operating range of this redistribution is limited by the diffusion length, which depends on the sort of the used atoms and the roughness of the substrate surface.

To get a better idea of this behaviour the material exchange of two Au-Ga eutectic nanoseeds with different sizes is illustrates in a model in Fig. 3.2. The two Au-Ga droplets of these model have different sizes, the distance between them is shorter than the Ga mean free path length, and they are next neighbours. With these assumptions the influence of any other nanoseed is neglected. The material exchange between these two nanoseeds starts, as soon as the thermal energy of the system is high enough. The material exchange is indicated by arrows in the model in Fig. 3.2. The above mentioned Ostwald ripening effect causes a material transport towards the bigger droplet. This happens, due to the fact, that the surface to volume ratio of bigger droplets is smaller than the surface to volume ratio of smaller nanoseeds. Furthermore, absorbs the bigger nanoseed more of the diffusing material because of its cross section. This transport behaviour continues until the small nanoseed is solidified because of the missing Ga content. Additionally, leads the material exchange between the nanosseds to a material deposition on one side of each nanoseed. This enables the approximation of the two nanoseeds and at one point

the fusion of them, like it is indicated in Fig. 3.2. Although the dominant diffusion factor is Ga, because of its low melting point and high vapor pressure, it can be assumed that Au diffuses inside the nanoseed to prevent a concentration gradient, which otherwise prohibits a phase separation in the nanoseed.

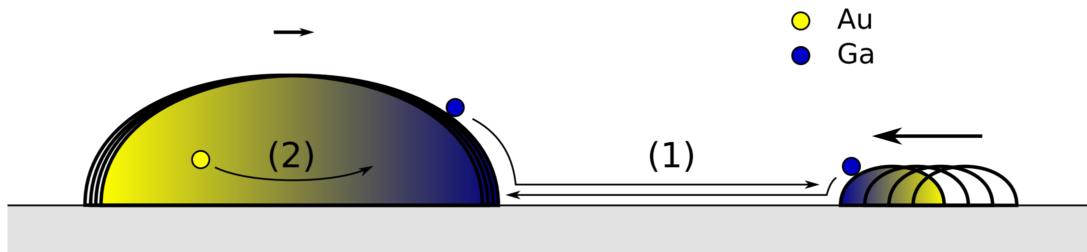

Fig. 3.2: The nanoseeds in the model move relative to each other. (1) Ga diffusion between the nanoseeds causes a agglomeration on one sidewall of each nanossed. (2) The diffusion of Au in the droplets prevents a concentration gradient.

To sum up, the observations above reveal that the material exchange and the effective movement of neighbouring nanoseeds lead to a redistribution of the statistical catalyst ensemble, which is influenced by the surface properties and the thermal energy of the dewetting process. This leads to the assumption that the diameter and the density of the Au-Ga eutectic nanoseeds depend on the material exchange that means on the amount of material and thermal energy of the system. The amount of material is regulated with the Au layer thickness on top of the substrate. If the Au layer is thin, below 1 nm, it might be that the Au layer does not cover the whole substrate surface. That means, the discussed material exchange between the nanoseeds is interrupted and the diameter of these nanoseeds should be smaller and the density higher than of those formed with a thicker Au layer. With an increasing Au layer thickness the Au layer covers the hole substrate surface without discontinuations and the exchange process can take place without interruptions. As a consequence, the diameter of the nanoseeds increases and the density decreases. But, the diameter and the density of the Au-Ga nanoseeds are not only influenced by the Au layer thickness, they should also be influenced by the dewetting temperature and time. These dependencies as well as the dependence on the Au layer thickness will be discussed in detail, next.

3.3 Density and Diameter of Au-Ga Nanoseeds

The dependencies of the densities and the diameters of the Au-Ga nanoseeds on the thickness of the Au layer are theoretically discussed in the last section. To get an idea of the investigations on the nanoseeds, which have been studied during this work, the following section outlines the studies on the dependencies of the density and the diameter of the Au-Ga nanoseeds on the parameters, such as the thickness of the Au layer, the dewetting temperature, the dewetting time or the substrate orientation.

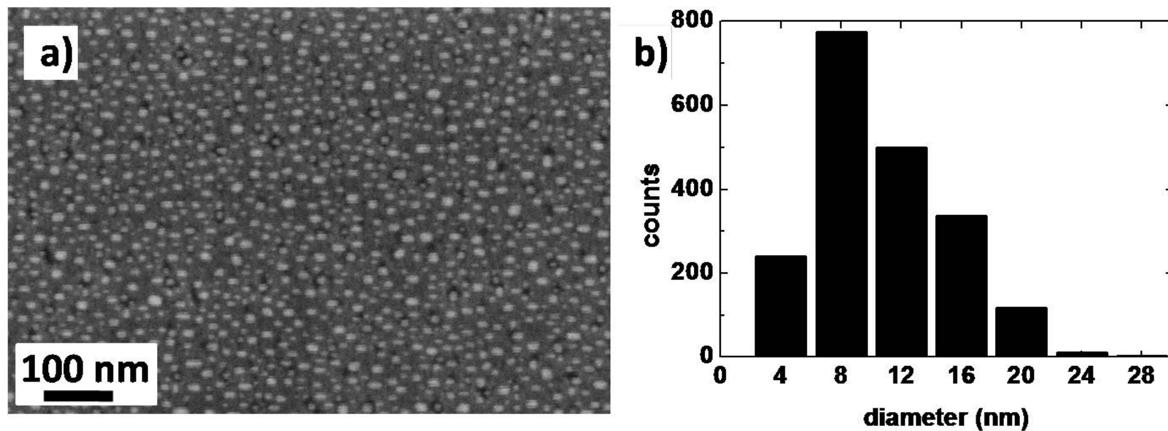

Fig. 3.3: a) Top view SEM image of the distribution of Au-Ga eutectic nanoseeds formed with a 1 nm thick Au layer at 460° C for 30 min. b) The corresponding histogram of the diameter distribution.

To check these dependencies samples with Au-Ga nanoseeds, produced in various dewetting conditions, are prepared and compared. "Various dewetting conditions" means that the thickness of the Au layer, the dewetting temperature, the dewetting time and the substrate orientations of the investigated samples are changed. The samples are compared by the help of SEM images, which are analyzed by using a script of a Mathematica program. The script of the Mathematica program determines the diameter and the density of the Au-Ga nanoseeds based on the brightness contrast differences between the nanoseeds and the substrate surface.

To get an idea how these analysis works Fig. 3.3a) shows a SEM image of typical Au-Ga nanoseeds on a GaAs:Si substrate and Fig. 3.3b) shows the corresponding histogram with the diameter distribution of these nanoseeds, determined with the skript of the Mathematica program. As an example, the Au-Ga droplets shown in the SEM image of Fig. 3.3a) are, formed with an 1 nm thick Au layer at 460° C for 30 min. The droplets of this SEM image have different sizes with a certain distance and they are fully developed. The average diameter of these nanoseeds is equal to 9 nm and their spread is ±5 nm. Besides the average diameter, the density of these droplets is determined with another script of the Mathematica program. As already mentioned this analysis procedure is employed to samples with Au-Ga nanoseeds prepared in different conditions.

The comparison of the collected results of the analysis of several samples is shown in Fig. 3.4. The graph in Fig. 3.4 presents the densities per μm^2 as a function of the diameter in nm of the Au-Ga nanoseeds. The dependencies are shown for thirteen different samples. Nine of these samples are formed with an 1 nm thick Au layer and four of them are formed with a 3 nm thick Au layer. For both groups, the samples formed with the 1 nm thick Au layer and those formed with the 3 nm thick Au layer the dewetting temperature, indicated with red dots, is varied between 380° C and 500° C with a constant dewetting time of 10 min and the dewetting time, indicated with blue triangles, is varied from 1 min to 30 min

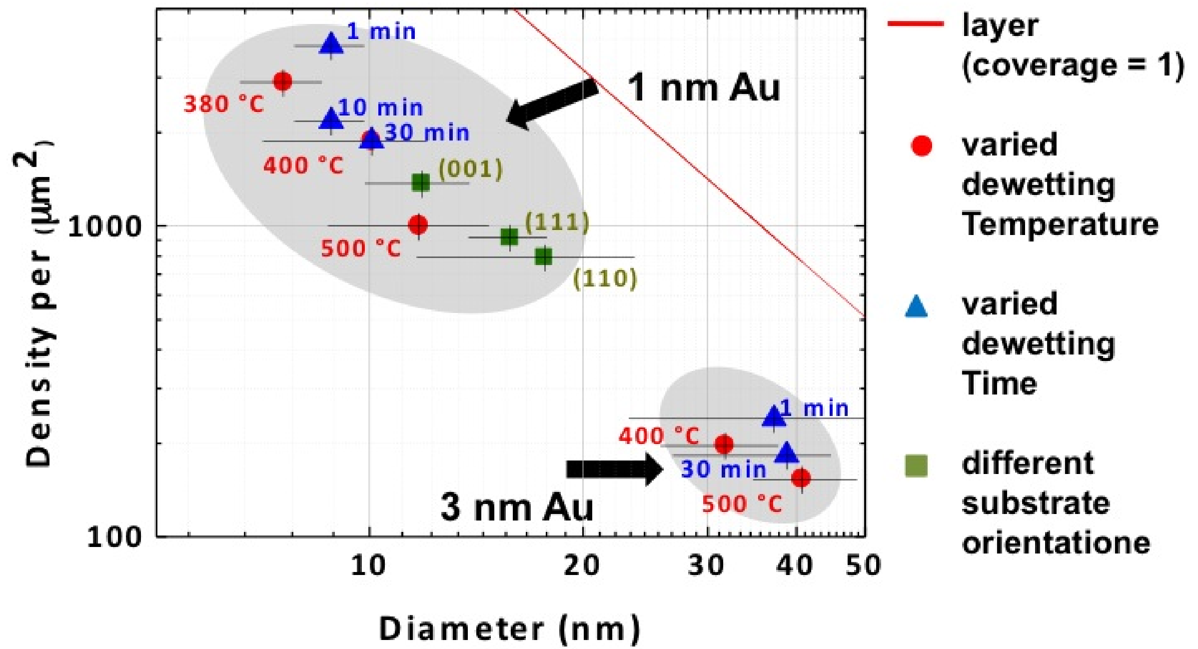

Fig. 3.4: Density and diameter dependence of Au-Ga eutectic nanoseeds formed with an 1 nm or 3 nm thick Au layer, varied dewetting temperatures, dewetting times and substrate orientations. The dewetting temperature is varied between 380° C and 500° C with a constant dewetting time of 10 min. The dewetting time is varied from 1 min to 30 min for a constant temperature of 400° C. The nanoseeds formed on the (001) substrate are dewetted at 460° C for 10 min those on the (110) and (111) substrate are dewetted at 480° C for 1 min.

for a constant dewetting temperature of 400° C. Furthermore, in the group of the samples formed with an 1 nm thick Au layer there are 3 samples where the dependencies on the substrate orientation are investigated, indicated with green rectangles. The nanoseeds formed on the (001) substrate are dewetted at 460° C for 10 min, those on the (110) and (111) substrate are dewetted at 480° C for 1 min.

The interpretation of these dependencies shown in Fig. 3.4 reveal that the effective thickness of the evaporated Au layer has the main influence on the distribution of the Au-Ga eutectic nanoseeds and divides the investigated samples into two groups, marked with grey areas. Nanoseeds formed with an 1 nm thick Au layer are much smaller and they have a higher density in relation to those formed with a 3 nm thick Au layer. The diameters of the nanoseeds formed with an 1 nm thick Au layer are around 10 nm and their density is around 2000 μm^{-2} independent of the other investigated parameters. For a 3 nm thick Au layer, the average diameter is around 35 nm, significantly thicker as compared to the diameter of nanoseeds formed with an 1 nm thick Au layer, and the average density is about 200 μm^{-2}, one order of magnitude lower.

But not only the thickness of the Au layer influences the morphology of the Au-Ga eutectic nanoseeds, also the dewetting temperature and the dewetting time, as already

mentioned. The dependence of the diameter and the density of the Au-Ga nanoseeds on these parameters causes the significant spread of data points of the grey areas. In detail the increase of the dewetting temperature for the samples formed with an 1 nm thick Au layer from 380° C to 500° C causes an increase of the average diameter of the Au-Ga nanoseeds from 7 nm up to 11 nm. At the same time the density of these nanoseeds decreases to one third, from 3000 μm^{-2} down to 1000 μm^{-2}. Furthermore, the increase of the dewetting time from 1 min to 30 min increases the diameter of the Au-Ga nanoseeds from 9 nm to 10 nm and decreases the density from 4000 μm^{-2} to 2000 μm^{-2}. The second grey area, which compares these dependencies for samples formed with a 3 nm thick Au layer reveals that a change in the dewetting temperature from 400° C to 500° C causes a change of nearly 10 nm in the diameter and the density changes from 150 μm^{-2} to 200 μm^{-2}. The change in the dewetting time has still less influence on the diameter and the density of the Au-Ga nanoseeds. The influence on the diameter is less than 5 nm and the difference in the density is around 50 μm^{-2}.

To sum up, the discussed investigations show that the dewetting temperature, as well as the dewetting time have a secondary influence on the diameter or the density of the Au-Ga eutectic nanoseeds compared to the thickness of the Au layer. This result is verified by the large diameter error bars, revealing the diameter distribution of the Au-Ga eutectic nanoseeds on one sample.

Next, the dependence of the diameter and the density of the Au-Ga nanoseeds on different substrate orientations, such as (100), (111)B and (110), is checked. As already mentioned these dependencies are shown with green rectangles in the grey area of the samples formed with an 1 nm thick Au layer. So the nanoseeds of these samples are all formed with an 1 nm thick Au layer. Those on the (100) substrate are formed at 460° C for 30 min and those formed on the (110) and (111)B substrate are dewetted at 480° C for 1 min. Although the dewetting time for the Au-Ga nanoseeds formed on the (100) substrate is longer the density of them is higher, and as a consequence the diameter is smaller compared to those formed on the substrate with the orientation (111)B and (110). This observation depends on the Ga diffusion length of the substrates and is consistent with the results of Lòpez *et al.*. They found that the Ga diffusion length on the (110) plane is longer than that on the (100) and (111) planes [Lope 95].

Besides the grey areas with the red dots, the blue triangles and the green rectangles there is a red line plotted in Fig. 3.4. This line marks the full coverage of the substrate surface by hypothetical Au-Ga nanoseeds, which is comparable with a surface filling factor of 1. Observations of Fig. 3.4 concerning this red line reveal that the experimental data points of the investigations summarized in the log-log plot of this figure determine a stripe, which is almost parallel to the red line. This means that in spite of the different diameters and densities the Au-Ga nanoseeds cover the same fraction of the GaAs area, about 20 %. Taking into consideration that the formation of Au-Ga nanoseeds is driven by the surface tension in the liquid phase of the eutectic, this result is to be expected.

To summarize the investigations of the whole section, the studies, based on the data points, shown in Fig. 3.4 indicate, that the diameter and density of Au-Ga nanoseeds are mutually related. As a consequence lowering the density of the Au-Ga nanoseeds while

keeping their diameter constant is impossible during the pure dewetting process without any other influence.

3.4 Ga Free Au Catalyst Particles

The particles examined in this section are also formed during the dewetting process of a thin Au layer ≤ 10 nm, like the Au-Ga nanoseeds. The difference is that they are formed on a ZnSe buffer layer with a different composition of the eutectic.

To reveal the difference between the above discussed Au-Ga eutectic nanoseeds, the new system, a thin Au layer on a ZnSe buffer layer, is investigated. First of all the phase diagrams of the several compounds are studied and the observations show that they differ significantly. The phase diagram of Au-Ga, as mentioned above, shows an Au-Ga eutectic point at 350° C for a Ga content of 30 % [Tche 06]. The phase diagram of Au-Zn has an eutectic point at 684° C and the Au-Se eutectic point is at 760° C [Mass 86]. So the eutectic points of Au-Zn or Au-Se are much higher in temperature than the eutectic point of Au-Ga. This fact matters if the eutectic temperatures of these materials are compared with the growth temperature of the ZnSe NWs, which is around 460° C. The eutectic point of Au-Ga is below the growth temperature and the eutectic points of Au-Zn or Au-Se are higher than the growth temperature. This might be the reason for the following observations made during this work.

To study the differences three samples with nanoseeds formed with different Au layer thicknesses on oxide free GaAs:Si substrates without and with a ZnSe buffer layer are prepared and compared. Fig. 3.5a) and b) show the SEM images of the nanoseeds formed on an oxide free GaAs:Si substrate with an 1 nm thick and 3 nm thick Au layer. Fig. 3.5c) shows the SEM image of the nanoseeds formed on a ZnSe buffer layer with a 3 nm thick Au layer. The two samples in Fig. 3.5a) and b) with nanoseeds formed on GaAs:Si show a clear dependence on the thickness of the Au layer as discussed in the previous section. The nanoseeds formed on a ZnSe buffer layer presented in Fig. 3.5c) have uniform small diameters and their density is very high compared to the Au-Ga nanoseeds formed with a 3 nm thick Au layer on a GaAs:Si substrate in Fig. 3.5b). Further observations show that the diameters of the nanoseeds, formed on the ZnSe buffer layer in Fig. 3.5c), are even smaller compared to the diameters of the Au-Ga nanoseeds, formed with an 1 nm thick Au layer on GaAs:Si, although they are formed with an effective 3 nm thick Au layer.

The comparison of the diameter and the density of the nanoseeds of the three samples shown in the SEM images in Fig. 3.5 indicates that the surface diffusion of Au on ZnSe is much lower than the surface diffusion of Au on GaAs. These observations and the comparison with the investigations described in literature reveal that the Au-Ga eutectic nanoseeds are liquid and the nanoseeds formed on ZnSe buffer are solid.

Chan *et al.*, for example, examined the formation of Au nanoseeds on ZnSe surfaces already a few years ago in [Chan 08]. They attributed that the reaction between Au and Zn causes a formation of nanotrenches and they proposed a model to describe the formation mechanism of these nanotrenches. They propose that Au reacts with ZnSe and

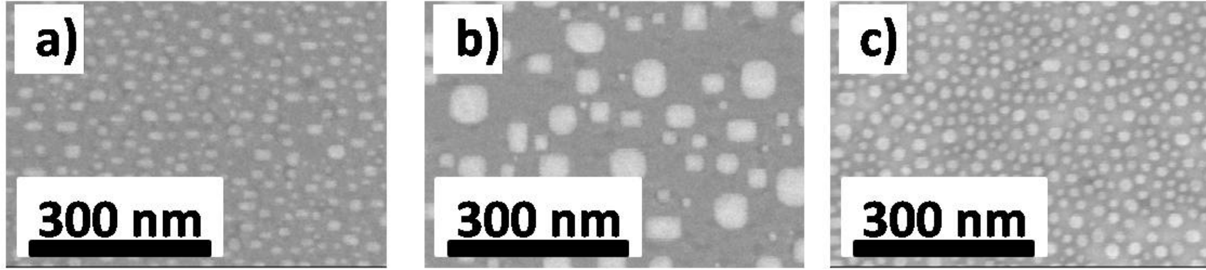

Fig. 3.5: SEM images of catalyst nanoseeds formed with an a) 1 nm and b) 3 nm thick Au layer on an oxide free GaAs:Si substrate and with a c) 1 nm thick Au layer on a ZnSe buffer layer. The nanoseeds are all formed at 460° C.

forms Au-Zn nanoseeds and Se vaporizes at a temperature of 530° C. Further heating and saturating the alloy leads to the migration of the nanoseeds [Chan 08].

With regards to the model of Chan *et al.* E. Bellet-Amalric *et al.* investigated the formation of Au nanoseeds on a ZnSe buffer layer with RHEED in-situ and ex-situ with different methods in [Bell 12]. Their RHEED observation show that the Au nanoseeds remain crystalline even at 510° C. Not only the lattice parameters of the RHEED but also the results of the ex-situ experiments like TEM and EDX indicate that the Au nanoseeds are not alloyed or show any presence of Zn or Se in the nanoseeds.

The fact that RHEED observations together with ex-situ investigations show that the Au nanoseeds on a ZnSe buffer layer remain crystalline even at 510° C revealed by E. Bellet-Amalric *et al.*, leads to the assumption that the Au nanoseeds during the ZnSe NWs growth on a ZnSe buffer layer during this work at 460° C are also solid. So the main difference between the Au-Ga nanoseeds formed on oxide free GaAs substrates and the nanoseeds formed on a ZnSe buffer layer is that in the first case the nanoseeds are liquid and in the second case the nanoseeds are solid. This has a consequence on the growth of the NWs. If the nanoseeds are liquid the NWs grow in the VLS growth mode and if the nanoseeds are solid the NWs grow in the VSS growth mode. These two growth modes are explained and compared in chapter 1. Further investigations during this work and reports in literature reveal that the control of the morphology of NWs grown in the VSS growth mode with a solid nanoseed is not as easy as in the VLS growth mode with a liquid nanoseed [Mess 09]. Because of that, focuses this work on Au-Ga eutectic nanoseeds formed on oxide free GaAs substrates and on the NWs grown from these nanoseeds.

3.5 Effects of Elemental Flux on Au-Ga Nanoseeds

As already mentioned and discussed in one of the previous sections Au-Ga eutectic nanoseeds are influenced by the Au layer thickness, the dewetting temperature and the dewetting time. Further experiences on the growth of ZnSe NWs compared with the growth of ZnTe NWs during this work reveal that the diffusion of the Au-Ga nanoseeds on the substrate surface does not stop at the end of the so called dewetting process. Because of that the influence of the elemental flux of the different materials used during the

growth of the NWs has to be checked. The materials distinguished and discussed are Ga, Zn, Te, Se and their compounds.

The following investigations on the effects of the elemental flux on Au-Ga eutectic nanoseeds is based on the observation of two SEM images of two samples with ZnSe and ZnTe NWs on top. The NWs of both samples are grown at the best growth conditions, concerning their material, on oxide free GaAs substrates with Au-Ga nanoseeds, prepared the same way. Given the fact that the Au-Ga nanoseeds of these two samples are prepared the same way, they have the same diameter distribution and the same density. Therefore the diameter and the density of the NWs of the two samples should be the same, if the diameter and the density of the Au-Ga nanoseeds determines the diameter and the density of the NWs.

Thus, comparing the SEM images of the samples with ZnSe and ZnTe NWs on top in Fig. 3.6a) and b) reveals that the diameter and the density of these NWs differs a lot.

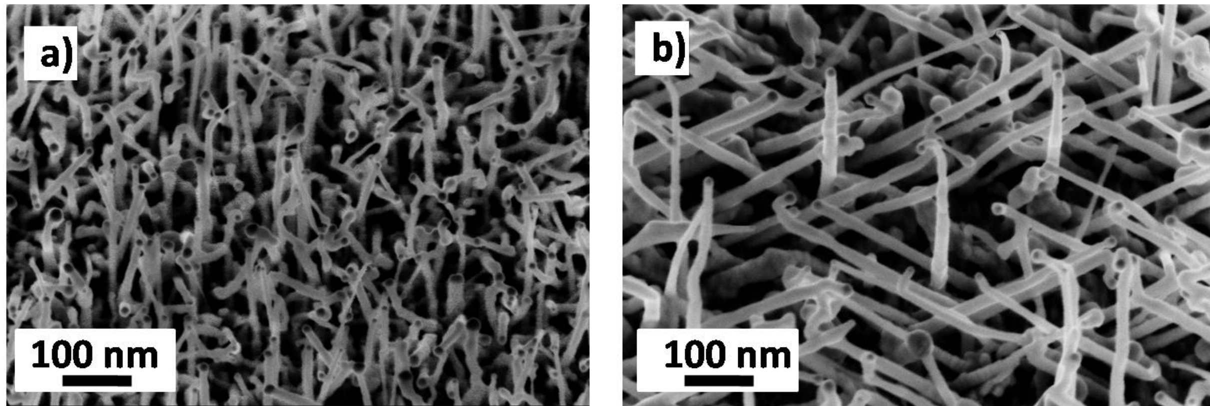

Fig. 3.6: SEM images of ZnSe NWs in a) and ZnTe NWs in b). The NWs are grown with an 1 nm thick Au layer on an oxide free GaAs:Si substrate at the best growth conditions concerning their material. The Au-Ga nanoseeds are prepared the same way for both samples.

The ZnSe NWs of the sample shown in the SEM image in Fig. 3.6a) have diameters in the range of 10 nm and the diameters of the ZnTe NWs shown in Fig. 3.6b) appear to be much thicker. Although the procedure used for the formation of the Au-Ga nanoseeds assures nanoseeds with an approximately 10 nm thick diameter and a density of around 2000 μm^{-2}. For the ZnSe NWs the diameter of the NWs and their distribution is nearly identical to the nanoseed distribution, but for the ZnTe NWs the density is much smaller, while the mean diameter is much larger. This is an indication that the catalysts, the Au-Ga eutectic nanoseeds, are influenced by the supplied materials.

First of all, the influence of the material Ga is investigated. To check the influence of additional Ga during the dewetting process samples with and without additional Ga are compared. The reference sample is a sample with Au-Ga nanoseeds formed without additional Ga and the investigated samples are samples where additional Ga is offered during the formation of the nanoseeds.

The SEM images of these samples are shown in Fig. 3.7. Fig. 3.7a) shows the SEM image of the nanoseeds formed without additional Ga. The mean diameter of these

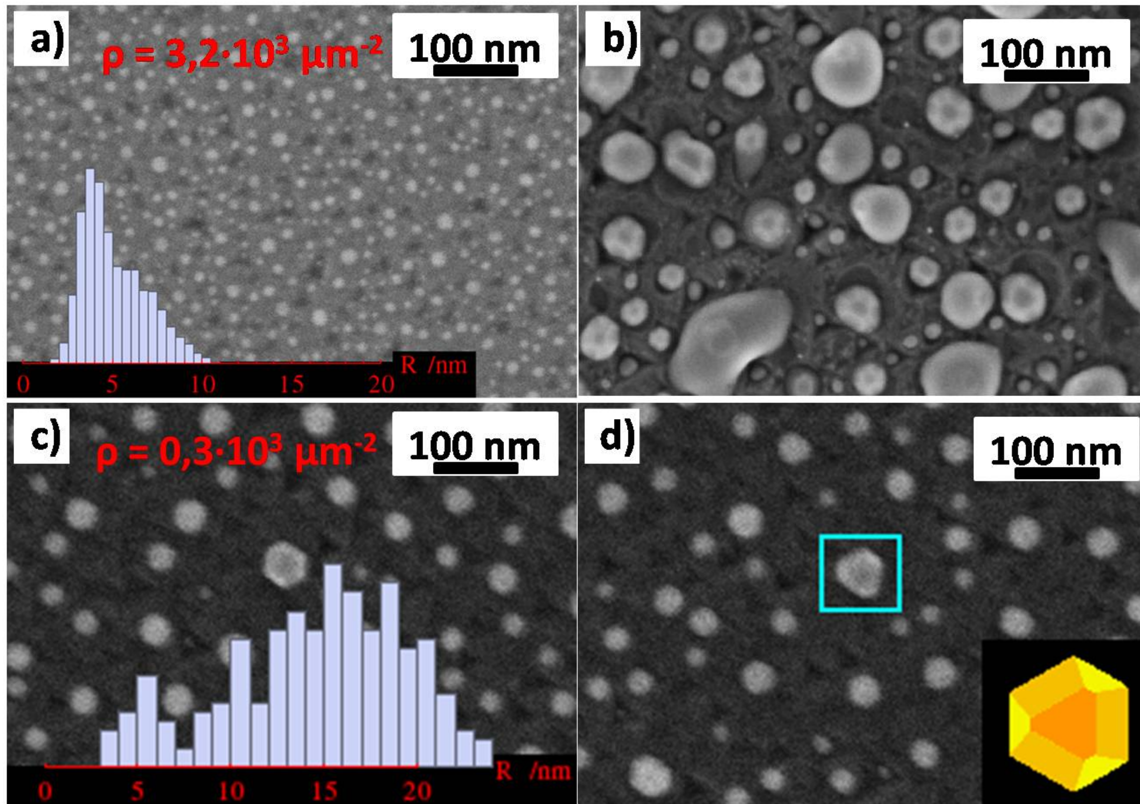

Fig. 3.7: SEM images of nanossets formed with and without additional Ga. a) SEM image of Au-Ga eutectic nanoseeds formed without additional Ga, the corresponding histogram of the diameter distribution and the value of the density of the droplets. b) SEM image of Au-Ga eutectic droplets formed with additional Ga. c) SEM image of Au-Ga eutectic nanoseeds formed with less additional Ga than in b), the corresponding histogram of the diameter distribution and the value of the density of the droplets. d) SEM images of Au-Ga nanoseeds formed with additional Ga with a schematic in the bottom right corner to highlight the facets of some nanoseeds.

nanoseeds is around 5 nm and their density is $\rho = 3{,}2{\cdot}10^3 \mu\text{m}^{-2}$. Fig. 3.7b) illustrates a SEM image of nanoseeds formed with an 1 nm thick Au layer and additional Ga, offered between 350° C and 385° C for 30 s. This image shows big nanoseeds, which are spherical with a crystalline core and some nanoseeds with diameters below 80 nm with facets. Fig. 3.7c) exhibits the SEM image of a sample where the nanoseeds are formed with a 0.4 nm thick Au layer and additional Ga for 2 s. These nanoseeds have a mean diameter of around 15 nm and their density is $\rho = 0{,}3{\cdot}10^3\ \mu\text{m}^{-2}$. The SEM image in Fig. 3.7d) highlights the facets of some nanoseeds of Fig. 3.7c).

The facets shown in the SEM image in Fig. 3.7b) originate, due to the fact that for a certain Au-Ga ratio the crystal lattice of the nanoseeds is stable, because of the local minimum in the liquidus line of Au-Ga [Elli 81]. If the Au-Ga eutectic mixture incorporates further Ga after reaching this local minimum, the illustrated facets are built.

A possible stoichiometry in this case could be Au_7Ga_3 [Elli 81]. The stability of this crystal prevents the incorporation of more Ga which is the explanation for the smaller nanoseeds in the SEM image in Fig. 3.7b). For the bigger nanoseeds the barrier of the stability is conquered and the nanoseeds consist of more or less liquid Ga with a crystalline core in the middle.

Comparing the nanoseeds of the SEM image of Fig. 3.7b) with the nanoseeds shown in the SEM images in Fig. 3.7c) and d) reveals that in Fig. 3.7c) and d) only the big nanoseeds in the middle have a crystal structure and in contrast all other nanoseeds are spherical. It seems that only the Ga concentration of the bigger nanoseeds reaches the crystalline Au-Ga phase. This is an evidence that the Ga content has an influence on the size of the nanoseeds, which is in agreement with the Ostwald ripening effect.

Another evidence of the influence of the Ga content on the diameter and the density of the nanoseeds shows the comparison of the nanoseeds shown in the SEM images of Fig. 3.7a) and c). The density $\rho = 0{,}3 \cdot 10^3\ \mu m^{-2}$ of the nanoseeds formed with additional Ga in Fig. 3.7c) is lower and the mean diameter, which is around 15 nm, of these nanoseeds is bigger than the density $\rho = 3{,}2 \cdot 10^3\ \mu m^{-2}$ and the mean diameter, which is around 5 nm, of those formed without any additional Ga in Fig. 3.7a).

To check the influence of Zn and Te on the Au-Ga eutectic nanoseeds two other samples are fabricated. For these samples Zn or Te is offered after the dewetting process during cool down for 4 min. The SEM images of these samples do not show any difference in diameter or density compared to nanoseeds formed without additional Zn or Te. Based on these analysis, it seems that the influence of additional Zn or Te is weaker than the influence of additional Ga.

In the case of Se it is known from literature that Se reacts with the Ga atoms of the nanoseeds and Ga_xSe_y precipitates. Zannier *et al.*, for example, show detailed studies on these topic referred to the morphology of ZnSe NWs in [Zann 14]. In this contribution this will be discussed in detail in chapter 4.

Although the SEM images in Fig. 3.6 show that the growth of ZnSe NWs differs significantly from the growth of ZnTe NWs, the influence of the elemental fluxes shows no significant influence on the diameter and the density of the Au-Ga eutectic nanoseeds. Hence the influence of the compounds ZnTe and ZnSe is investigated next.

3.6 Redistribution of Nanoseeds at the Growth Start of ZnTe Nanowires

The investigations above show, that the elemental fluxes Zn, Te and Se are not responsible for the morphological difference between pure Au-Ga eutectic nanoseeds, ZnSe and ZnTe NWs. To find an explanation for the differences in the morphology of pure Au-Ga eutectic nanoseeds and ZnTe NWs the growth start of the ZnTe NWs is studied in details.

For these investigations two samples are prepared. One sample is a sample with Au-Ga eutectic nanoseeds formed with a 0.6 nm thick Au layer at 480° C for 30 s without any growth. The second sample is a sample with Au-Ga eutectic nanoseeds formed with

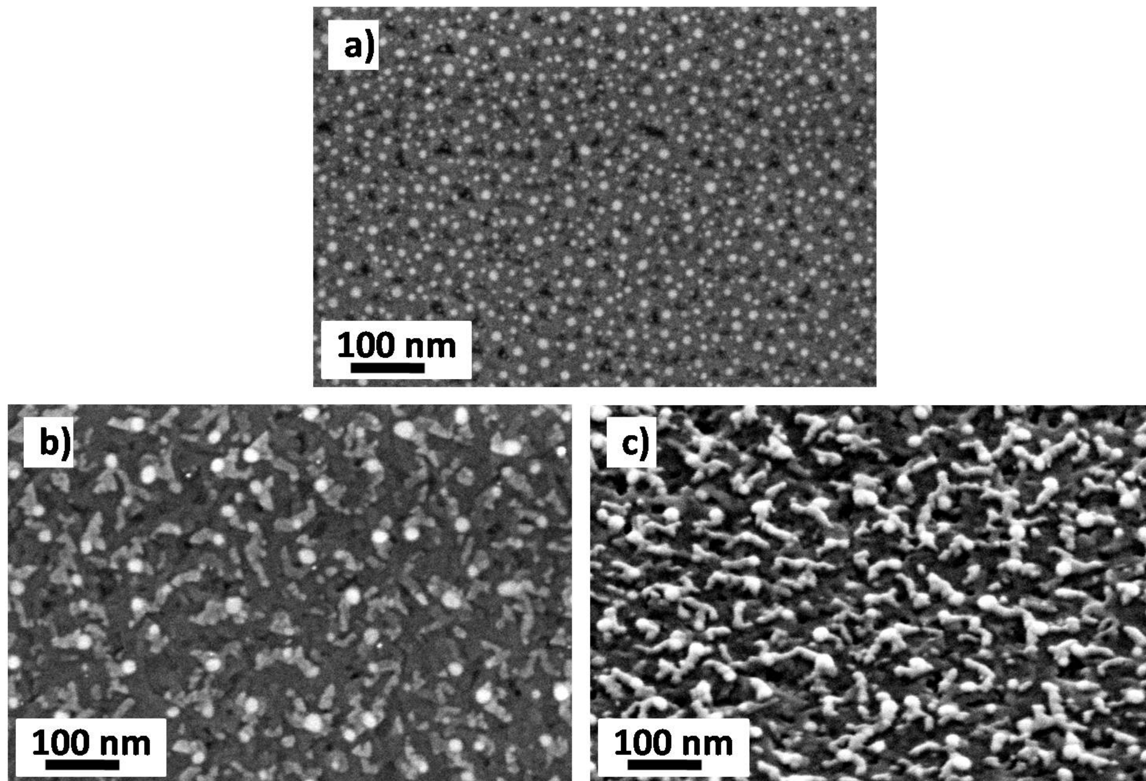

Fig. 3.8: a) SEM images of the distribution of pure Au-Ga eutectic nanoseeds formed with a 0.6 nm thick Au layer dewetted at 480° C for 30 s. b) Top view SEM image of Au-Ga eutectic nanoseeds formed the same way after an additional ZnTe growth start of 2 min. c) Side view SEM image with an angle of 45° of the nanoseeds shown in the SEM image in b).

a 0.6 nm thick Au layer at 480° C for 30 s and a following 2 min ZnTe growth at 400° C. The SEM images of these samples are shown in Fig. 3.8.

The comparison of the SEM images in Fig. 3.8 reveals a few differences. The main difference is that the nanoseeds after a short ZnTe growth in Fig. 3.8b) are less dense and homogeneous than nanoseeds without a ZnTe growth in Fig. 3.8a). Additionally to the white Au-Ga eutectic nanoseeds the top view in Fig. 3.8b) shows some kinked traces leading to the nanoseeds. These traces have a different brightness compared to the substrate, which is an indication that the material of these traces differs from the substrate material. In our system these traces consist of ZnTe. Observing the side view SEM image in Fig. 3.8c) with regards to this color or material contrast reveals that the NWs at this state do not grow perpendicular to the surface. At the initial stage of the growth, the ZnTe NWs lie on the GaAs surface and grow parallel to the substrate surface, before they change their growth direction and start to grow perpendicular to the substrate surface, what is visible in Fig. 3.10.

A statistical analysis of the diameter distribution of these Au-Ga eutectic nanoseeds is shown in the histograms in Fig. 3.9. The histogram in Fig. 3.9a) shows the diameter distribution of Au-Ga eutectic nanoseeds before growth and Fig. 3.9b) shows the diameter distribution of Au-Ga eutectic nanoseeds after a 2 min ZnTe growth. The densities ρ of

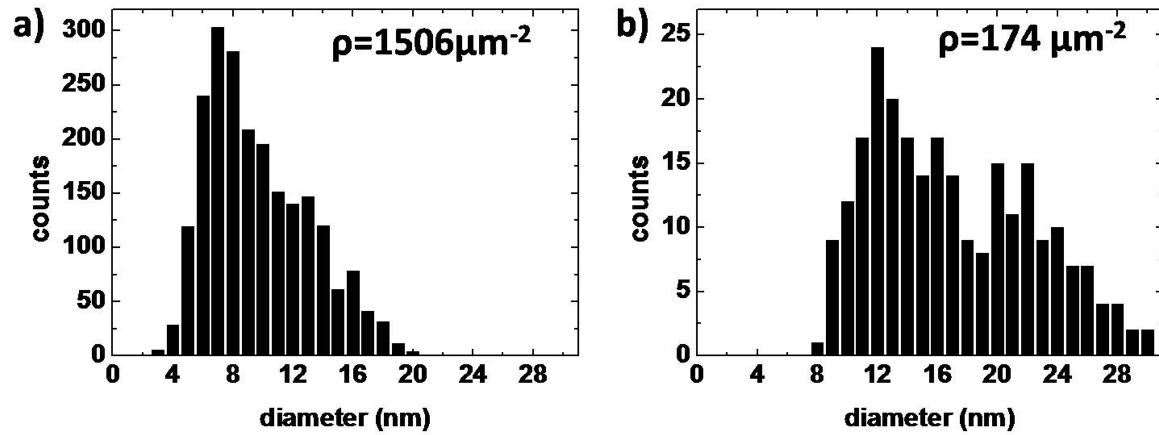

Fig. 3.9: Corresponding histograms to Fig. 3.8 of the diameter distribution of a) pure Au-Ga eutectic nanoseeds, b) Au-Ga eutectic droplets after a short ZnTe growth start. The density ρ of these distributions is noted in the upper right corner of the histograms.

these assemblies differ significantly. The initial density of $\rho = 1506\ \mu\text{m}^{-2}$ before the ZnTe growth drops by one order of magnitude to $\rho = 174\ \mu\text{m}^{-2}$ after a 2 min ZnTe growth. Furthermore, exhibit the histograms that not only the density of the Au-Ga eutectic nanoseeds changes, rather the diameters of the Au-Ga eutectic nanoseeds also changes drastically. The diameter distribution ranging from 3 nm to 20 nm with a maximum around 7 nm, changes to a broadened distribution with maximums around 12 nm and 22 nm.

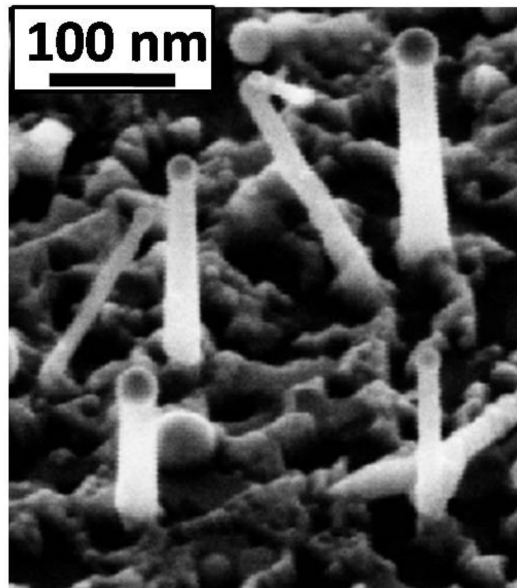

Fig. 3.10: SEM image of ZnTe NWs with drag marks of the nanoseed redistribution at the growth start of ZnTe NWs.

To study the ZnTe NWs growth start in more detail another sample has been prepared. Here the growth of the ZnTe NWs is proceeded for 10 min. The SEM image of this sample is shown in Fig. 3.10. This sample exhibits straight and uniform ZnTe NWs growing perpendicular to the substrate surface and on the substrate surface there are 1D structures which are presumably formed at the very beginning of the growth process.

These structures form traces to every NW and it looks like every wire crawls along the substrate surface before it raises. In Fig. 3.10 is every perpendicular NW surrounded by more than one surface 1D structure. This suggests that the growth proceeds in two phases, at the beginning ZnTe grows parallel to the substrate surface forming 1D structures at the surface. These 1D surface structures push the nanoseeds in every direction until two or more nanoseeds meet. The collision of these nanoseeds is unavoidable because of the coverage of the substrate surface with Au-Ga nanoseeds. If two or more such a structures merge, the nanoseeds get larger and less dense, the growth changes direction and perpendicular NWs emerge.

The observation of this behaviour in more detail and the comparison of the growth of ZnTe NWs with the growth of ZnSe NWs leads to a simple model explaining the growth start of ZnTe NWs. The observations reveal that the ZnTe NW growth starts with a redistribution of Au-Ga eutectic nanoseeds. The elaborated model in Fig. 3.11 illustrates how this redistribution starts and the single steps of the redistribution leading to the NW growth.

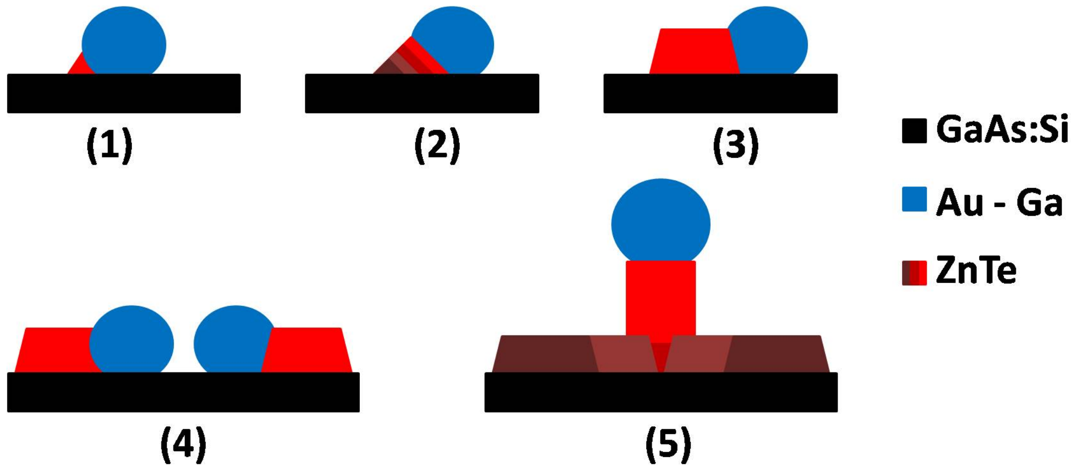

Fig. 3.11: Model of the five steps of the nanoseed redistribution at the growth start of ZnTe NWs.

Step (1) shows the catalytic precipitations of crystalline ZnTe at the triple-interface of vacuum, the droplet and the substrate. The ZnTe nucleus at the triple-interface is a crystalline ZnTe island. The island might have its origin in the lattice mismatch between ZnTe and GaAs. Regarding to the layer growth of ZnTe on GaAs it is known that the lattice mismatch of the two materials causes the formation of crystalline islands [Long 98]. Further precipitation leads to the formation of a crystal facet (2). The crystal facet grows as long as the contact angle between the solid-liquid and the liquid-vapor interface is $\geq$

90°. If this contact angle is ≤ 90°, the adhesive force is bigger than the cohesive force and the droplet spreads. The facet breakes the thermodynamic equilibrium of the surface energies of the liquid-vapor, solid-vapor and solid liquid interface. The resulting force causes a lateral movement of the droplet on the substrate surface (3) [Schw 99]. The lateral movement takes place as long as a droplet can move without any disturbance until it reaches an other droplet (4). If two or more of these droplets meet, the growth facets also meet each other, and at one point, the curvature of the droplet surface is the same at both facets, there is no resulting force in a lateral direction and the NWs grow perpendicular to the surface.

This model explains the observations shown in Fig. 3.10 and it exhibits why the diameter and the density of ZnTe NWs is different to the diameter and the density of ZnSe NWs, although they are grown from nanoseeds formed in the same conditions.

3.7 Nanoseeds Formed with an Amorphous Te or Zn Layer

Detailed studies on the formation of the nanoseeds show that with the usual parameters of the dewetting process, like Au layer thickness, dewetting temperature and dewetting time it is not possible to lower the density of Au-Ga eutectic nanoseeds independent of their diameter. Further investigations on the growth start reveal that some materials like ZnTe cause an redistribution of the nanoseeds at the growth start. For ZnSe this is not the case. This leads to the assumption that Te is the main activator in the redistribution process. Thinking about Te with regards to ZnSe leads to self assembled CdSe/ZnSe quantum dots with a Te cap layer of S. Mahapatra [Maha 07]. Having this in mind, we tried to form Au-Ga eutectic nanoseeds on oxide free GaAs:Si substrates with a Te cap layer on top of the Au layer to lower the density of the Au-Ga eutectic nanoseeds independent of their diameter.

The cap layer is evaporated on a GaAs substrate with a thin Au layer ≤ 10 nm on top in the II-VI chamber at a very low temperature of 150° C for 5 min. The dewetting process starts directly after this evaporation. RHEED observations during this process reveal that the characteristic change in the diffraction pattern for the nanoseed formation on GaAs appears at a different temperature for samples with and without a Te cap layer on top. To investigate this observation SEM images of two samples with nanoseeds prepared without and with a Te cap layer are compared.

Fig. 3.12 shows the SEM images of these samples. The Au-Ga nanoseeds of Fig. 3.12a) are pure Au-Ga eutectic nanossedsformed without a Te cap layer and those of Fig. 3.12b) are Au-Ga eutectic nanoseeds formed with a Te cap layer. Besides the Te cap layer the dewetting process of these two samples is the same. It was done at 460° C for 10 min. The results show, that the density of the nanoseeds formed with a Te cap layer in Fig. 3.12b) is very low compared to the density of the pure Au-Ga nanoseeds in Fig. 3.12a).

The fact that a Te cap layer reduces the density of the nanoseeds drastically might

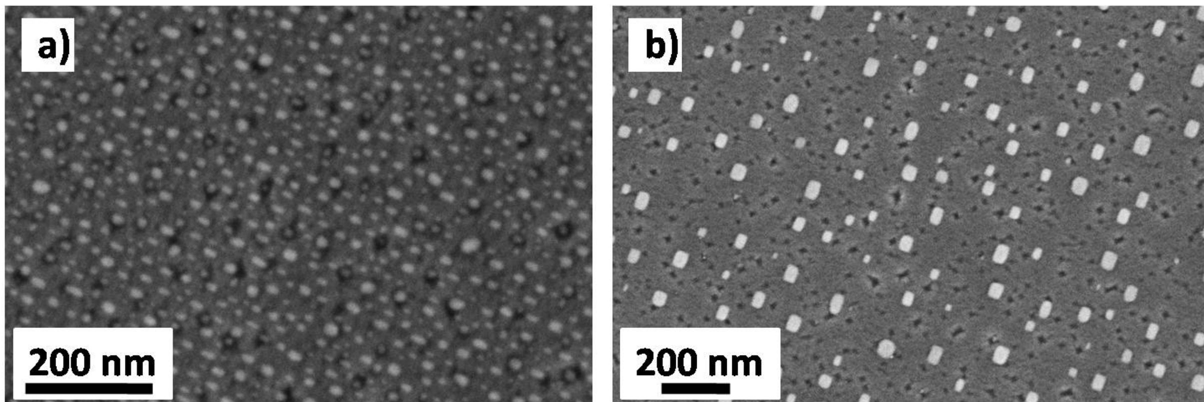

Fig. 3.12: a) Au-Ga eutectic nanoseeds formed with an 1 nm thick Au layer. b) Au-Ga eutectic nanoseeds formed with a Te cap layer on top of the 1 nm thick Au layer. The dewetting for the two samples was at 460° C.

be associated with the result that a thicker Au layer causes a lower density of the eutectic nanoseeds and a larger diameter. Tellurium has a melting temperature of 449.5° C [Holl 95], which is in the range of the Au-Ga eutectic temperature. Referred to this the effective liquid film on the substrate with a Te cap layer might be thicker than without this cap layer and the diffusion process during the nanoseed formation might be higher.

Besides the suggestions that the liquid film on top of the substrate is thicker with a Te cap layer as without, there must be another effect, which causes the low density of the eutectic droplets independent of the diameter. As it is known from Fig. 3.4 the coverage of the droplets formed with a pure Au layer is more or less fixed independent of the Au layer thickness.

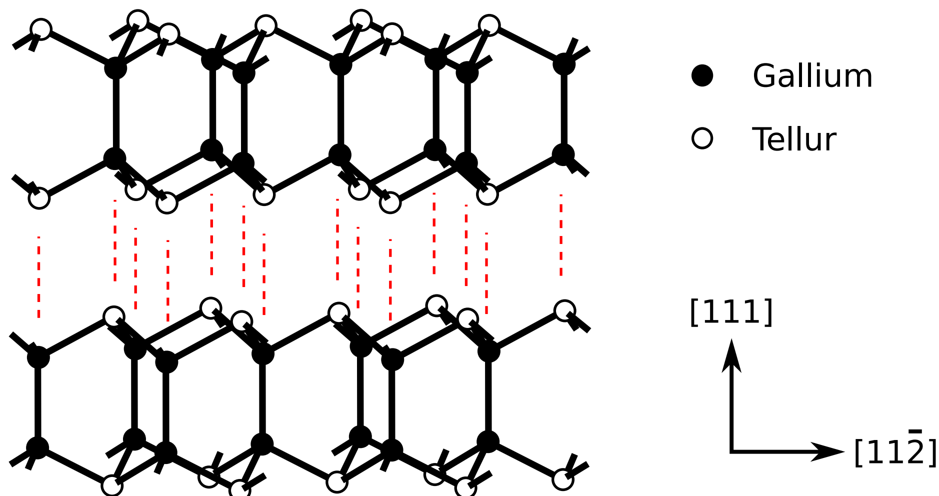

Fig. 3.13: Schematic of the crystal lattice of Ga_2Te according to [Juli 79]. The van-der-Waals interaction between the layers is indicated in red.

This effect might be based on GaTe bonds. The most stable state of these bonds is Ga_2Te. A schematic of the Ga_2Te crystal structure is shown in Fig. 3.13. The crystal

lattice of this compound consists of a Ga atom which is tetrahedral surrounded by three Te atoms and another Ga atom [Juli 79]. In the discussed case is the surface covered with Te bonded to the next crystal layer by van-der-Waals bonds without any dangling bonds. The low dispersion rate of this system causes a higher diffusion length of the Ga atoms. As a consequence and with regards to the model in Fig. 3.2 the material exchange of this system takes place over a wider range and bigger droplets with a significant lower density are formed, shown in Fig. 3.12b). To verify the formation of Ga_2Te on the substrate surface further investigations with X-ray photoelectron spectroscopy have to be done.

Independent of the effect which lowers the density of the Au-Ga eutectic nanoseeds, if they are formed with a Te cap layer, the Te cap layer might be a possibility to lower the density of the ZnSe NWs. To investigate this assumption ZnSe NWs are grown from nanoseeds formed with a Te cap layer and these NWs are compared to ZnSe NWs grown from nanoseeds formed without a Te cap layer. Fig. 3.14 shows the SEM images of these two samples. Fig. 3.14a) of the ZnSe NWs grown with Au-Ga eutectic nanoseeds formed without a Te cap layer and Fig. 3.14b) of the ZnSe NWs grown with nanoseeds formed with a Te cap layer.

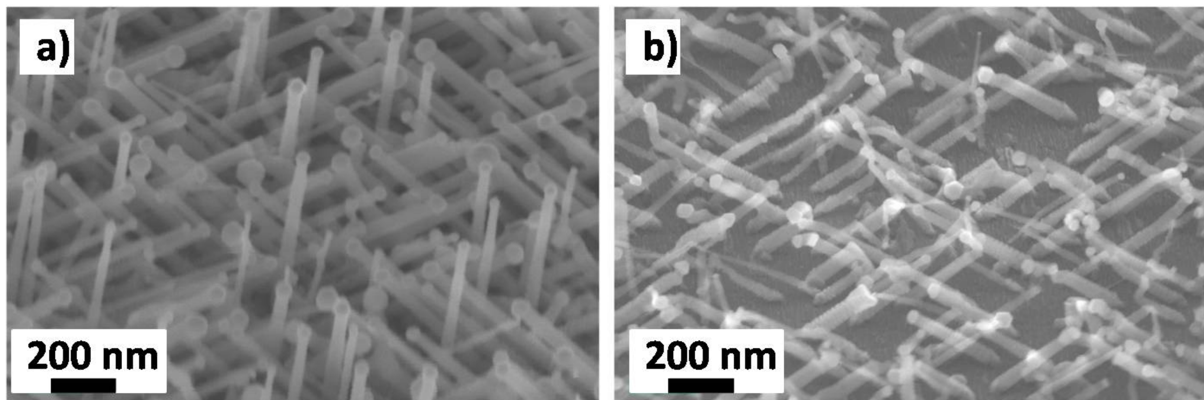

Fig. 3.14: a) SEM image of NWs grown at 460° C from Au-Ga eutectic nanosseds formed with a 3 nm thick Au layer. b) SEM image of NWs grown at 550° C from Au-Ga eutectic nanoseeds formed with a Te capped 1 nm thick Au layer.

The ZnSe NWs grown from the nanoseeds formed with a Te cap layer on top of the Au layer in Fig. 3.14b) are less dense then those grown from nanoseeds formed without a Te cap layer in Fig. 3.14a). The comparison shows that the diameter of the NWs of these two samples is nearly the same. However the Te cap layer has no influence on the diameter of the NWs, it influences the coverage of the substrate.

But, apart from the advantage that Te reduces the density of ZnSe NWs, it might be a problem for the ZnSe NW growth, because of the incorporation of Te into the nanoseeds during the dewetting process or into the ZnSe NWs during growth. To avoid this we tried to form nanoseeds with an amorphous Zn layer. Zn has a rather identical vapor pressure as Te. To investigate the behaviours of an amorphous Zn layer again two samples are prepared and compared. One sample with Au-Ga nanoseeds prepared without a Zn cap layer and another one with an amorphous Zn layer on top of the Au layer. SEM images

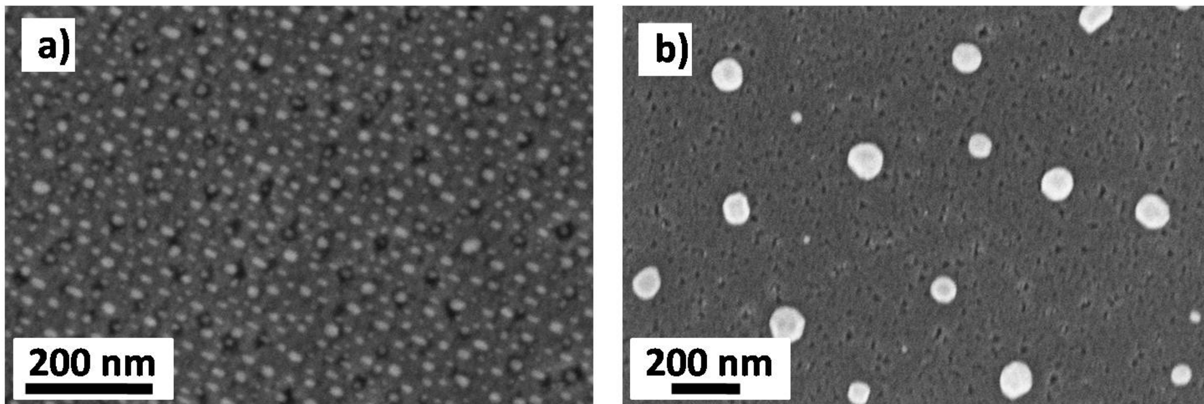

Fig. 3.15: a) SEM image of Au-Ga eutectic nanoseeds formed with an 1 nm thick Au layer at 460° C. b) SEM image of Au-Ga nanoseeds formed with a Zn cap layer on top of a 0.8 nm thick Au layer at 400° C.

of these two samples are shown in Fig. 3.15.

Fig. 3.15b) illustrates the nanoseeds formed with an amorphous Zn layer on top of the Au layer and Fig. 3.15a) shows those formed without any cap layer. The nanoseeds in Fig. 3.15b) are less dense compared to the nanoseeds in Fig. 3.15a). So, it seems that an amorphous Zn cap layer has the same effect like an amorphous Te cap layer.

Regardless to the observations depending on the density of the nanoseeds and NWs made with a Te or Zn cap layer on top of the Au layer during the nanoseeds formation, the investigations on the morphology of the ZnSe NWs in the next chapter are done without a cap layer.

Chapter 4

Results: Morphology of ZnSe Nanowires

This chapter focuses on the characterization of ZnSe NWs grown with Au-Ga eutectic nanoseeds in the VLS growth mode. The morphology, such as the diameter, the orientation, if they are straight and ordered or not and the density, of the NWs is investigated. The characterization methods are the analysis of SEM and TEM images. SEM images are used to characterize the morphology of the ZnSe NWs with respect to the Au-Ga eutectic nanoseeds, the growth temperature, the growth time, the growth rate, the Zn to Se flux ratio and the substrate orientation. TEM images are studied to analyze the crystal quality of single ZnSe NWs.

4.1 Influence of the Growth Process on the Morphology of ZnSe Nanowires

Control of the morphology of ZnSe NWs is important for practical applications. The ZnSe NWs investigated in this work are used for optic and transport measurements. In both cases the length of the NWs plays a crucial role and the diameter has to be controlled with respect to their applications.

The diameters and the densities of the Au-Ga nanoseeds, which are determined by the thickness of the Au layer, have the main influence on the diameters and the densities of the NWs. Further parameters influencing their diameters and densities are the flux ratio, the growth rate, the growth temperature, the growth time and the substrate orientation.

Based on reports in literature and our experience on the epitaxial ZnSe layer growth, our first try to grow ZnSe NWs was ZnSe NWs grown from Au-Ga eutectic nanoseeds formed with an 1 nm thick Au layer on an oxide free GaAs:Si $\langle 001 \rangle$ substrate, a Se to Zn ratio of 2:1 and growth temperatures above 300° C. A SEM image of these NWs is shown in Fig. 4.1. NWs grown under these conditions have diameters ≤ 10 nm. Each single NW has a different orientation and the density is that high that they influence each other. As a consequence all parameters of the NWs, like diameter, length and their density have to

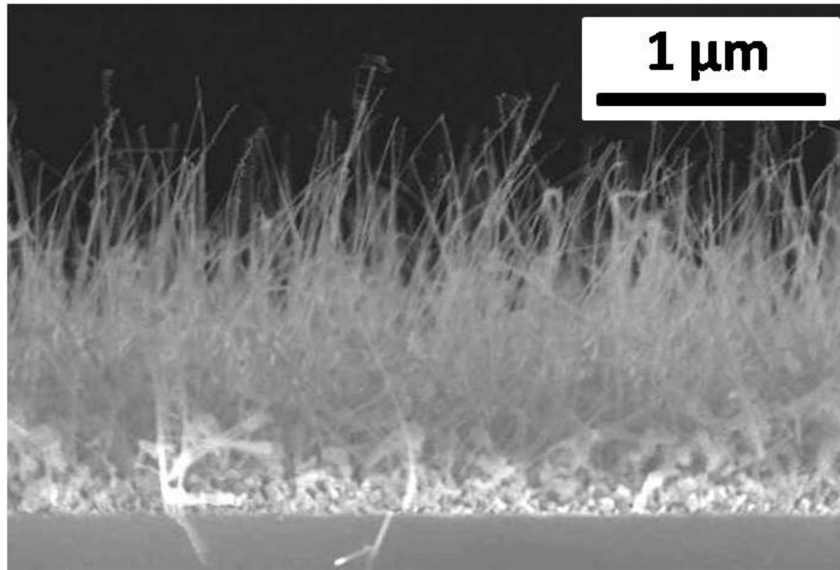

Fig. 4.1: SEM image of kinked and disordered ZnSe NWs grown from nanoseeds, formed with an 1 nm thick Au layer at 500° C for 10 min. The NWs are grown at 400° C for 1h with a Zn to Se flux ratio of 1:2.

be optimized by controlling the growth parameters, such as fluxes, temperature and time.

4.1.1 Diameters and Densities of Nanoseeds and Diameters and Densities of Nanowires

As already mentioned, a crucial task in controlling the diameters and the densities of ZnSe NWs is the influence of the diameters and the densities of the Au-Ga nanoseeds. To investigate this, four samples with NWs grown with nanoseeds formed with different Au layer thicknesses are prepared and studied. The NWs of these samples are grown at 460° C for 1 h and the nanoseeds have been formed at 460° C for 30 min. The Au layer thickness for the formation of the nanoseeds of these four samples is increased from 1 nm to 8 nm. SEM images of these samples are shown in Fig. 4.2.

Fig. 4.2a) shows the SEM image of NWs which are grown with nanoseeds formed with an 1 nm thick Au layer. These NWs are nearly 1 μm long and their diameter is between 10 nm and 20 nm. There are a few thin and straight NWs but most of them are thin, have different orientations and they are kinked. Near the substrate surface the NWs seem to be thicker and curved like "worms". The NWs on the sample illustrated in Fig. 4.2b) are grown with a 3 nm thick Au layer. Most of them are straight and ordered and reveal the orientation, which is given by the substrate. The substrate orientation is $\langle 001 \rangle$ and the NWs show the typical orientations $\langle 111 \rangle$ and $\langle 11-2 \rangle$. The diameter of these NWs is between 20 nm and 60 nm and they are about 800 nm long.

The NWs in Fig. 4.2c) are grown with nanoseeds formed with a 5 nm thick Au layer. The SEM image of this sample reveals a few very thin NWs with diameters $\leq$ 10 nm, but most of the NWs are thick with diameters $\geq$ 60 nm. Thick NWs grow straight and

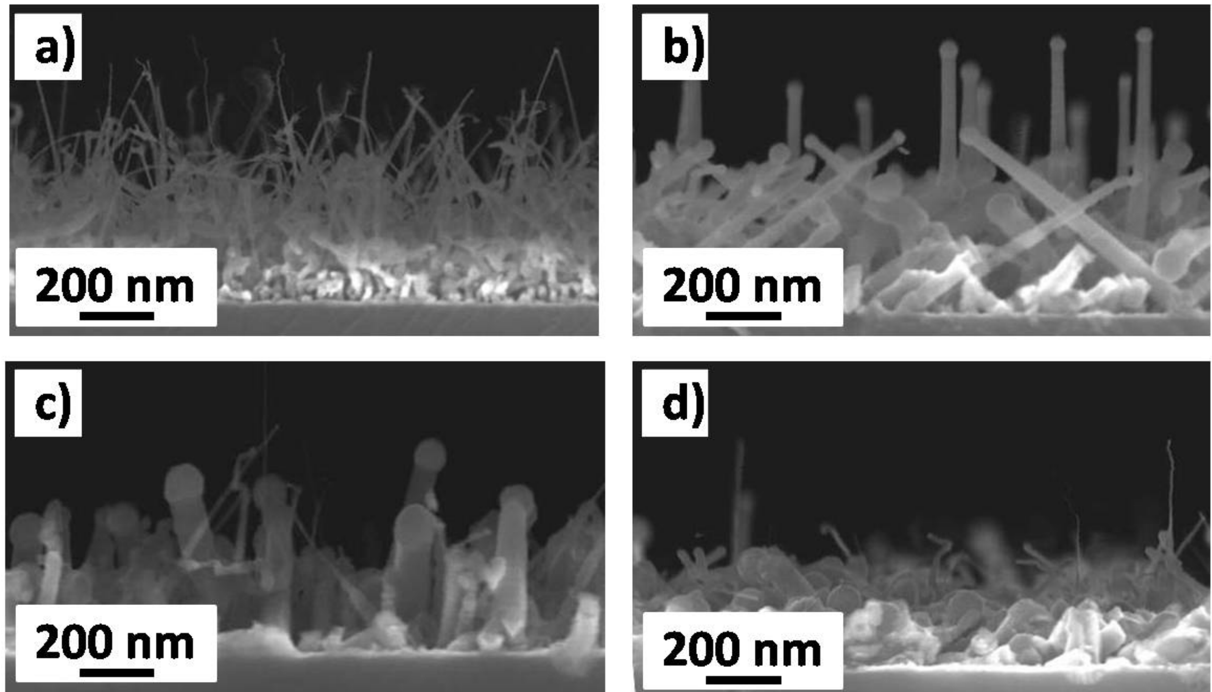

Fig. 4.2: ZnSe NWs grown at 460° C for 1h from nanosseds formed with different Au layer thicknesses a) 1 nm, b) 3 nm, c) 5 nm and d) 8 nm at 460° C for 30 min.

ordered in contrast to thin NWs, which have no specific orientation. NWs, grown with a 8 nm thick Au layer are shown in Fig. 4.2 d). A few NWs of this sample are thin with diameters $\leq$ 10 nm, but most of them are thick with diameters $\geq$ 60 nm, they are kinked and lie on the substrate surface.

As expected, the diameter and the density of the ZnSe NWs reveal the same dependence on the Au layer thickness as the diameter and the density of the Au-Ga eutectic nanoseeds. An increasing Au layer thickness results in larger and less dense Au-Ga eutectic nanoseeds and as a consequence in thicker and less dense ZnSe NWs. The dependencies known from the Au-Ga eutectic nanoseeds are reflected on the NWs at least for the samples shown in Fig. 4.2a) and b). In the case of the samples shown in Fig. 4.2c) and d), it is hard to reveal any dependence because each NW has a different orientation and their diameters are thin $\leq$ 10 nm as well as very thick $\geq$ 60 nm.

First of all this observation leads to the assumption that the Au-Ga nanoseeds formed with a 5 nm or 8 nm thick Au layer are not fully developed. That means the dewetting temperature and the dewetting time has to be adjusted in this case. Although the results in Fig. 3.4 in chapter 3 show that the dependence on the dewetting temperature and time for Au-Ga eutectic nanoseeds formed with an 1 nm or 3 nm thick Au layer is of secondary importance. Independent of the formation of the Au-Ga nanoseeds, another reason for samples with thin and thick kinked NWs, grown with Au layers thicker than 3 nm, might be a wrong growth temperature or a wrong Zn to Se flux ratio.

Apart from this, is the diameter of the NWs, grown with a 3 nm thick Au layer, between 40 nm and 60 nm and thick enough for transport measurements. Compared to

NWs grown with a 1 nm, 5 nm or 8 nm thick Au layer they have a uniform diameter and they are straight and ordered. Hence this 3 nm thick Au layer is used to check the influence of the other growth parameters, such as the growth temperature and the Zn to Se flux ratio, on the morphology of the ZnSe NWs.

4.1.2 Influence of the Growth Temperature on the Morphology of ZnSe Nanowires

The growth temperature is the temperature of the substrate during the NW growth. ZnSe NW growth has been observed for temperatures between 380° C and 550° C. However the temperature range where ZnSe NWs exhibit a uniform, straight and ordered morphology is much smaller. To find this range a set of samples with NWs grown at different growth temperatures on oxide free GaAs:Si substrates with the orientations ⟨001⟩ and ⟨110⟩ are investigated.

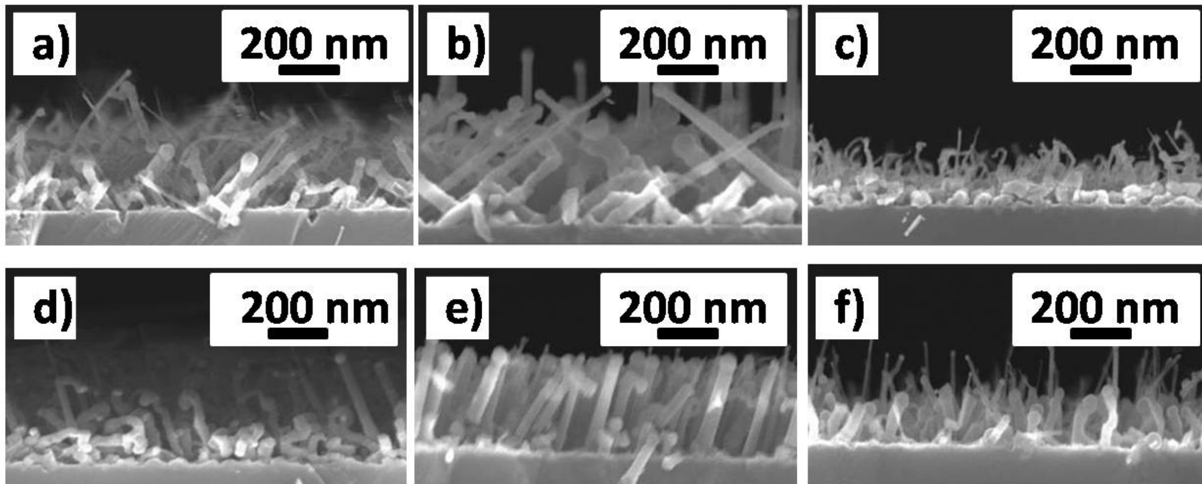

Fig. 4.3: ZnSe NWs on oxide free GaAs:Si ⟨001⟩ a) - c) and ⟨110⟩ d) - f) substrates grown at different substrate temperatures: a) and d) at 400° C, b) and e) at 460° C and c) and f) at 500° C. The Au-Ga eutectic nanoseedsof these samples are formed with a 3 nm thick Au layer.

Fig. 4.3 shows SEM images of NWs grown on GaAs:Si ⟨001⟩ and ⟨110⟩ substrates at 400° C, 460° C and 500° C. Most of the NWs grown at 400° C, shown in Fig. 4.3a) and d), have the typical diameter for a 3 nm thick Au layer between 40 nm and 60 nm, but they have no particular orientation and they are kinked. The NWs grown at 460° C are shown in Fig. 4.3b) and e). They are straight and ordered with directions given by the substrate. Those grown on a GaAs:Si ⟨001⟩ substrate in Fig. 4.3b) show the directions ⟨001⟩, ⟨111⟩ and ⟨11 − 2⟩ and those grown on GaAs:Si ⟨110⟩ substrates in Fig. 4.3e) show the direction ⟨111⟩. The SEM images in Fig. 4.3c) and f) show NWs, which are grown at 500° C. All these NWs have different directions and they are kinked with different diameters ranging from 10 nm to 20 nm up to 40 nm or 60 nm.

The investigations on the substrate temperature show that NWs with a straight and ordered morphology grow at 460° C independent of the used substrate. The temperature

460° C is a few degrees above the temperature where the formation of the nanoseeds changes from solid to liquid. The formation is observed in a change of the characteristic RHEED pattern. At this temperature the Au-Ga eutectic nanoseeds should be liquid and the NW growth should be determined by a supersaturation of them. At 500° C the nanoseeds are also liquid, but the desorption of the NW material from the nanoseeds might be more than at 460° C and the precipitation at the liquid solid interface might be less than at 460° C. Because of that the NWs grown at 500° C are shorter, disordered and kinked. For those grown at 400° C it might be that the nanoseeds are in a solid phase. There is no homogeneous precipitation at the liquid solid interface which might be the reason for kinking.

Another reason for disorder and kinking of the NWs below and above 460°C could be the Ga content versus the Zn to Se flux ratio at these temperatures. The amount of Ga in the nanoseeds on top of the NWs depends on the Zn to Se flux ratio. This is discussed in detail by Zannier *et al.* in [Zann 14]. They made these observation at the same time the investigations on the Zn to Se flux ratio were done during this work. The observations done in this work together with the work of Zannier *et al.* are shown next.

4.1.3 Influence of the Zn to Se Flux Ratio on the Morphology of ZnSe Nanowires

With regards to the layer growth of ZnSe on GaAs at the beginning of this work, the ZnSe NWs are grown with an excess of Se. But further investigations and literature reviews reveal that the control of the morphology of ZnSe NWs is easier in Zn rich conditions. Because of that, the above illustrated dependencies are all done with NWs grown with an excess of Zn. To understand this decision, this chapter focuses in detail on the dependence of the diameters, the growth directions and the densities of ZnSe NWs on the Zn to Se flux ratio.

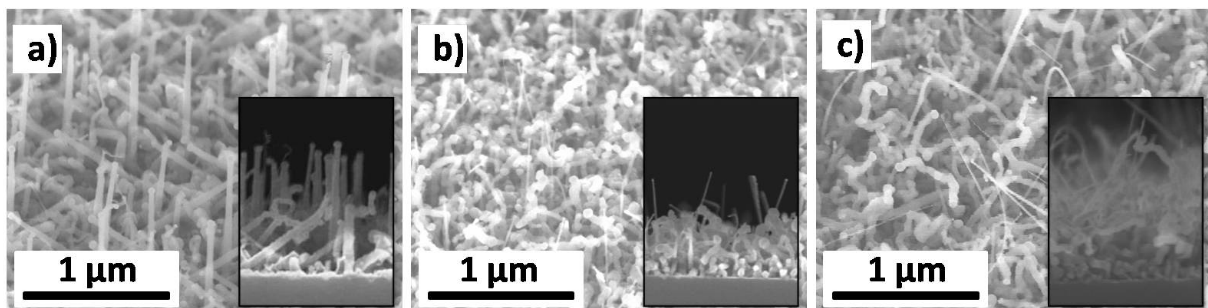

Fig. 4.4: Top view and 90 degree side view SEM images of ZnSe NWs grown at 460° C for 30 min. They are grown from nanoseeds formed with a 3 nm thick Au layer at 460° C with different Zn to Se flux ratios. a) 2:1 , b) 1:1 and c) 1:2.

To investigate these dependencies, three samples with NWs grown with different Zn to Se flux ratios are considered. The nanoseeds of these samples are formed with a 3 nm thick Au layer at 460° C. The growth of the NWs takes place at 460° C for 30 min.

Fig. 4.4 shows topview and 90 degree side view SEM images of these samples. The image in Fig. 4.4a) shows NWs which are grown under an excess of Zn. The Zn to Se flux ratio is 2:1. These NWs have diameters between 40 nm and 60 nm and they are straight and ordered like the NWs discussed before. The NWs on the image in Fig. 4.4b) are grown with a Zn to Se flux ratio of 1:1. The NWs are disordered, non-uniform and kinked with different diameters. The diameters cover the hole range from very thin NWs with diameters around 10 nm to thick NWs with diameters ≥60 nm. NWs grown under an excess of Se are shown in Fig. 4.4c). In this case the Zn to Se flux ratio is 1:2. Most of these NWs are disordered, non-uniform, kinked and very thin with diameters between 10 nm and 20 nm. There are only a few thicker ones, which creep on the substrate surface.

Up to this point, it has been found, that it makes a big difference for the morphology of the NWs if they are grown in Zn or Se rich conditions, although they are grown from the same Au-Ga eutectic nanoseeds, at the same growth temperature for the same time. The best results concerning the morphology of ZnSe NWs grown on oxide free GaAs:Si substrates independent of their orientation reveal ZnSe NWs grown in Zn rich conditions.

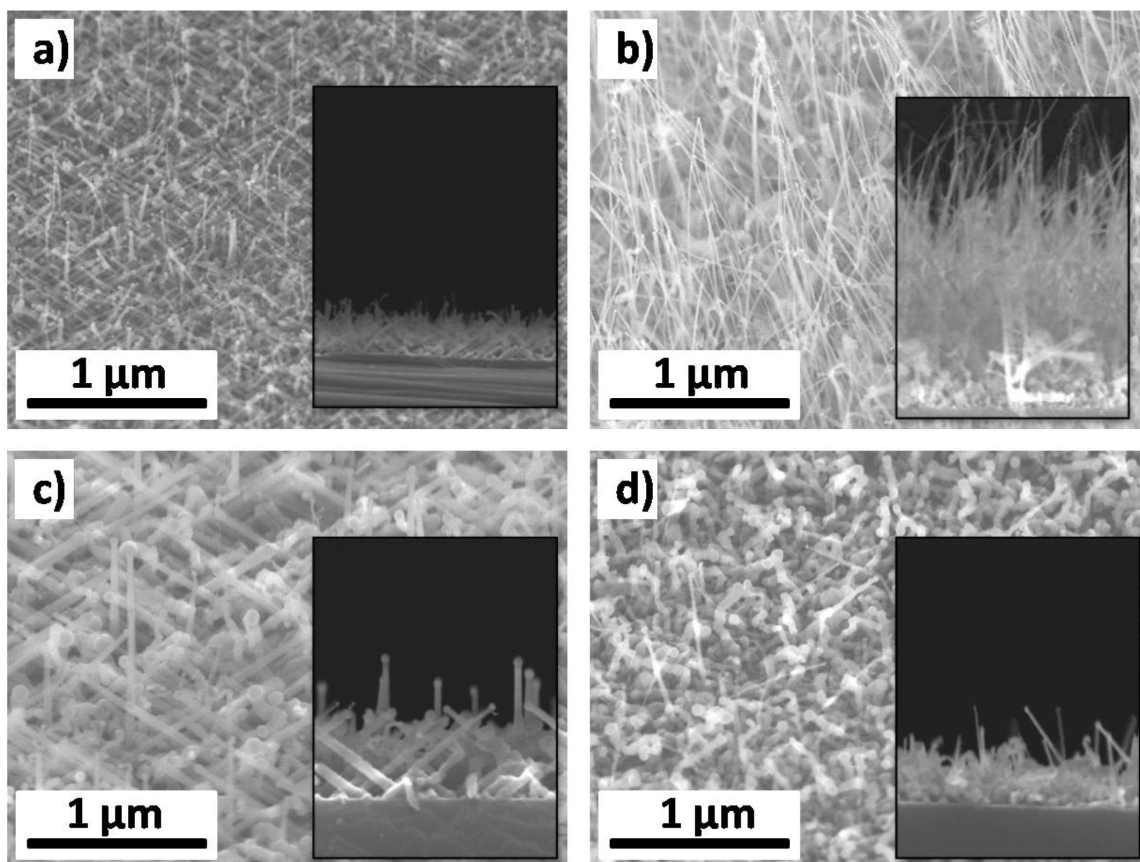

Fig. 4.5: SEM images of ZnSe NWs grown in Zn and Se rich conditions with nonoseeds formed with an 1 nm or 3 nm thick Au layer. a) Zn rich with an 1 nm thick Au layer, b) Se rich with an 1 nm thick Au layer, c) Zn rich with a 3 nm thick Au layer and d) Se rich with a 3 nm thick Au layer.

This is in contrast to the ZnSe layer growth on GaAs:Si substrates where Se rich conditions reveal the best results. Based on these investigations, it can be assumed that the main parameter, which determines the orientation of the NWs and if they are straight or not, is the Zn to Se flux ratio. In contrast, the diameter of the NWs is determined by the Au layer thickness, which is also the main parameter determining the diameter of the the Au-Ga eutectic nanoseeds. These are the two main aspects of the investigations on the control of the morphology of the NWs. To get a clear image of these two dependencies Fig. 4.5 focuses again on these two aspects.

Fig. 4.5a) and b) show SEM images of ZnSe NWs grown with nanoseeds formed with an 1 nm thick Au layer in Zn as well as in Se rich conditions and the SEM images of Fig. 4.5c) and d) show ZnSe NWs grown with nanoseeds formed with a 3 nm thick Au layer in Zn and Se rich conditions. The comparison of the SEM images in Fig. 4.5a) and c) clearly shows the dependence of the diameter on the Au layer thickness of NWs grown in Zn rich conditions. ZnSe NWs grown with nanoseeds formed with an 1 nm thick Au layer in Fig. 4.5a) reveal a diameter around 10 nm and those grown with a 3 nm thick Au thick layer in Fig. 4.5c) reveal diameters between 20 nm and 60 nm. The comparison of Fig. 4.5a) and b) or Fig. 4.5c) and d) shows that NWs grown in Zn rich conditions are straight and ordered and those grown in Se rich conditions are kinked and disordered independent of their diameters. All our investigations reveal that it is difficult to handle the morphology of ZnSe NWs in Se rich conditions. Furthermore it is hard to influence the density of the ZnSe NWs in any case. So the influence of the growth rate, growth time and substrate orientation is investigated next.

4.1.4 The Control of the Morphology of ZnSe Nanowires with Regards to the Growth Rate, Growth Time and Substrate Orientation

To handle the problems with the morphology of the NWs grown in Se rich conditions, the growth rate is lowered. That means, the Zn and Se beam equivalent pressures are in the range of $2{\cdot}10^{-7}$ torr and $6{\cdot}10^{-7}$ torr instead of $7{\cdot}10^{-7}$ torr and $1.2{\cdot}10^{-6}$ torr. Using these fluxes and a growth time of 1 h, the length of the NWs is between 300 nm and 500 nm, depending on the substrate orientation. SEM images of these samples are shown in Fig. 4.6 and they reveal again that the NWs grown in Se rich conditions, shown in Fig. 4.6a), compared to those grown in Zn rich conditions, shown in Fig. 4.6b), are kinked and disordered.

It can be observed that the growth rate of the NWs does not determine wether the NWs grow straight and ordered or kinked and disordered.

Besides that, a detailed observation of the growth time reveals, that the growth time plays a significant role if ZnSe NWs kink or not in Se rich conditions as well as in Zn rich conditions. Fig. 4.7a) shows a SEM image of a sample with ZnSe NWs grown for 90 min in Zn rich conditions and Fig. 4.7b) shows ZnSe NWs grown from the same nanoseeds in the same conditions for 180 min. The NWs in Fig. 4.7a) are straight and ordered over

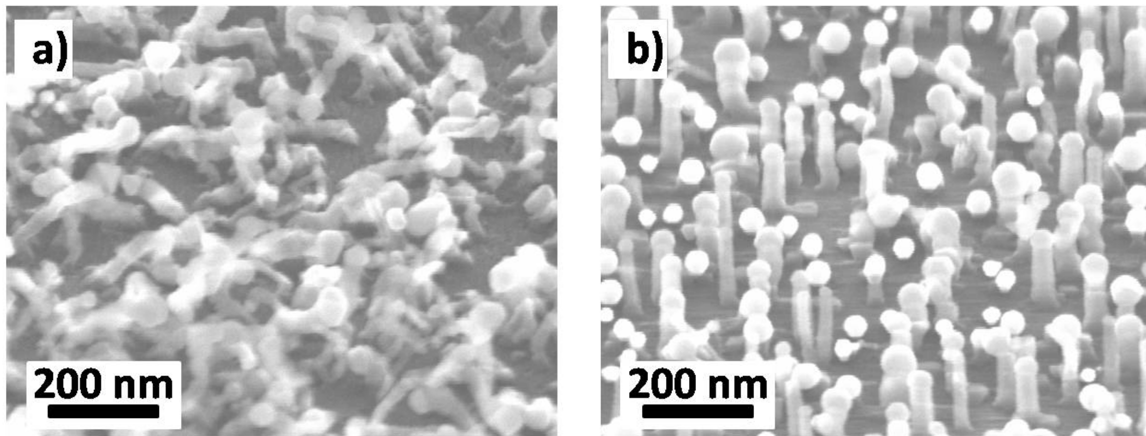

Fig. 4.6: SEM images of ZnSe NWs grown with low Zn and Se fluxes in the range 2 - $6{\cdot}10^{-7}$. a) Se rich and b) Zn rich.

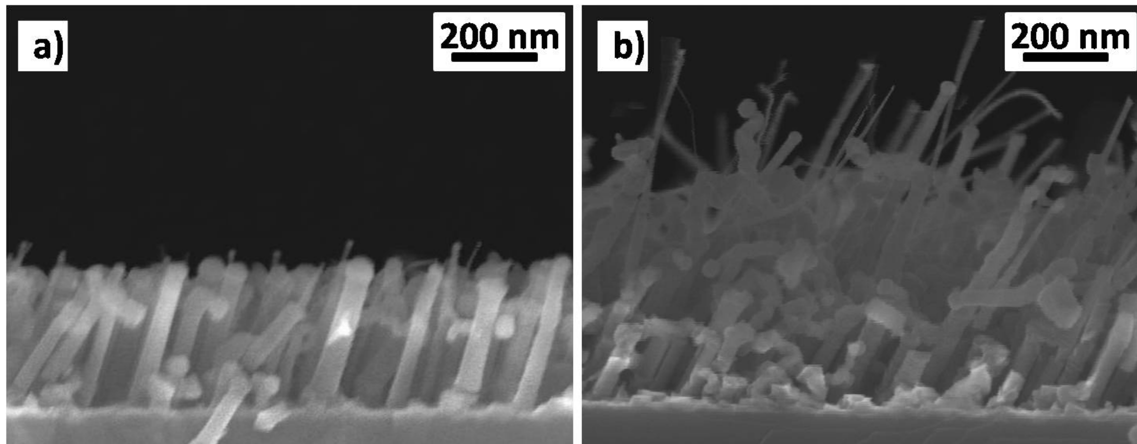

Fig. 4.7: SEM images of ZnSe NWs grown in Zn rich conditions on GaAs ⟨110⟩ for a) 90 min and b) 180 min.

their entire length and the NWs in Fig. 4.7b) start kinking after a while. This observation confirms the fact that the Se atoms react with the Ga atoms of the nanoseeds on top of the NWs, discussed in detail by Zannier *et al.* in [Zann 14].

Zannier *et al.* report in [Zann 14] that the chemical composition of ZnSe NWs and the physical state of the nanoseeds during growth is strongly affected by the Zn to Se flux ratio. They report that in Zn rich conditions ZnSe NWs grow straight and uniform over their entire length with spherical Au-Ga eutectic nanoseeds on top and in Se rich conditions the NWs are kinked and the nanoseeds on top of the NWs are faceted with an irregular profile. Based on SEM images, XPS measurements, HRTEM images and EDX maps they attribute this observation to the fact that the Se exposure alters the chemical composition of the Au-Ga nanoseeds from Au-Ga back to metallic gold. They found out that under Zn rich conditions most of the offered Se atoms react with the existing Zn atoms and built crystalline ZnSe. In this case the growth is VLS driven by liquid Au-Ga eutectic nonoseeds, as long as the excess of Zn and the amount of Ga in the droplet is

big enough. The amount of Ga depends on the growth temperature and the size of the nanoseed, and the excess of Zn depends on the Zn to Se flux ratio. Referred to these parameters the NWs start kinking and the nanoseeds solidify after a certain growth time. If the growth takes place under Se rich conditions, there is an excess of Se atoms reacting with the Ga atoms of the nanoseeds and the nanoseeds start to solidify at the beginning of the growth. At this time the NWs start to kink because the probability for the binding atoms to find a nucleation site before reaching the interface between the nanoseed and the NW is higher and leads to a change in the growth direction of the NW. The conclusion is as long as ZnSe NWs grow in the VLS growth mode, they are straight and as soon as the growth mode changes to VSS because of the supplied Se atoms the NWs start to kink [Zann 14].

The summary of the investigations concerning the diameter and the orientation of the ZnSe NWs done in this work reveals that the best ZnSe NWs are achieved with nanoseeds formed with a 3 nm thick Au layer at 460° C, with a Zn to Se flux ratio of 2:1, a growth temperature around 460° C and a growth time of 1 h. Using these conditions ZnSe NWs are straight and ordered independent of the used substrate orientation.

To highlight these observations, SEM images of ZnSe NWs grown with these conditions on three different GaAs:Si substrates with different orientations ⟨001⟩, ⟨110⟩ and ⟨111⟩ are shown in Fig. 4.8. The growth directions of these NWs reflect the typical substrate orientations. The Au-Ga nanoseeds on top of these NWs are spherical and the wires are around 1 μm long. As a next step, the crystalline quality of these NWs has to be considered.

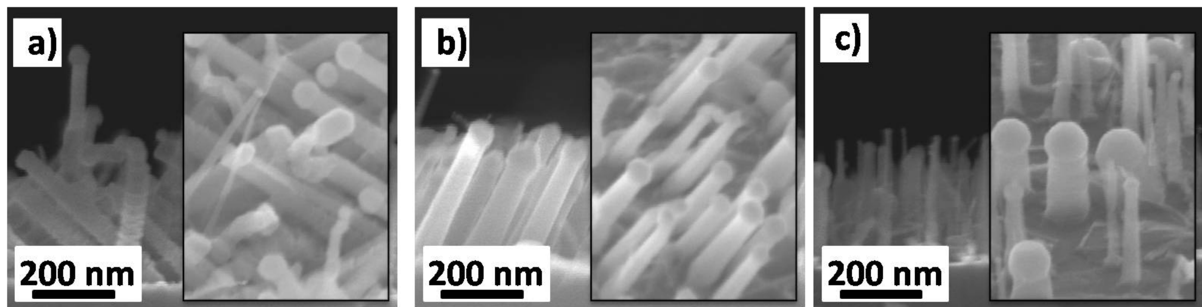

Fig. 4.8: SEM images of ZnSe NWs grown with optimized growth conditions on a) GaAs:Si ⟨001⟩, b) GaAs:Si ⟨110⟩ and c) GaAs:Si ⟨111⟩.

4.2 Crystalline Quality

The crystalline quality is not as easy to observe as the morphology of the ZnSe NWs. To observe the crystalline quality of a ZnSe NW, it is important to look into the NW, it is not enough to investigate the surface of the NW.

Furthermore, it has to be considered that most characterizations methods concerning the crystalline quality, like TEM, make use of single NWs. Because of that, the singular-

ization method used in this work is described at the beginning of this section, before the results of the TEM investigations are discussed.

4.2.1 Singularization of the Nanowires

To singularize NWs means to separate single NWs from the as-grown ensemble of NWs to a new host substrate. There are two ways to singularize NWs. One way is a mechanical strip off of the as-grown sample to the host sample. In this case the as-grown sample lies topdown on the host substrate and the NWs are knocked off with a tweezer, which knocks on the backside of the as-grown sample. Afterwards, the density of the NWs on the host sample is irregular. There are areas with many NWs and areas with a few NWs. The advantage of this method is that this method is fast and straightforward, as long as many NWs in one area are needed. The disadvantage of this method is on the one hand the pressure of the tweezer and on the other hand the irregular distribution of the single NWs. If the pressure of the tweezer is too high, the NWs and the host substrate will be damaged and there will be many residues of the as-grown sample on the host sample above and beyond the NWs. These residues may interfere the investigations on the real NWs.

The second method is to solve the NWs of the as-grown sample in a solvent via a ultrasonic bath and drip the solvent with the NWs on a host substrate with a pipette. As a solvent, it is possible to use pure water, isopropanol or methanol. The best results are obtained with 0.5 ml isopropanol. The 0.5 ml isopropanol together with a small piece of the as-grown sample are put in a small bottle in an ultrasonic bath for 20 s. The frequency of the ultrasonic bath is 87 kHz. The dissolved NWs are transferred to the host substrate with a pipette.

Afterwards, the droplets of the solvent on the host substrate are dried with several methods. One method is, to dry the droplets in air with or without a heating plate. A second method is, to blow dry the droplets with a N_2 gun and the third one, used in this work, is to dry the droplets of the solvent with a spin coater. The drying process with the spin coater reveals the best results regarding on the density and the regular dispersion of the NWs. Compared to the separation of the NWs with a mechanical strip off, the separation with the solvent is more gentle and the distribution of the NWs on the host substrate is more homogeneous.

Besides all the advantages and disadvantages, the experiences, made with the singularization of the NWs during this work, demonstrate that the quality of the separation method depends on the dimension of the NWs, on the state of the host substrate and on the application of the single NWs after separation. As a rough guide independent of the singularization method, one should keep in mind, that small and gentle NWs with diameters ≤ 10 nm do not need as much pressure for singularization as bigger NWs with bigger diamters ≥ 20 nm. Concerning the length of the NWs, it should be considered, that long NWs with a length of 1 μm will break more than one time if the pressure of singularization is to high.

4.2.2 Transmission Electron Microscopy Investigations on ZnSe Nanowires

Against all expectations, that Se rich conditions are the best growth conditions for the ZnSe layer growth, the studies on the morphology of ZnSe NWs on GaAs:Si substrates in the last section exhibits that straight and ordered NWs are grown in Zn rich conditions. Thus, with regards to the applications of ZnSe NWs, not only the control of the morphology of the NWs is important, the crystal structure of the NWs plays a crucial role, too. From the above mentioned parameters the Zn to Se flux ratio should have the main influence on the crystalline quality. Because of that, the investigations on the crystalline quality of the ZnSe NWs should be based on the dependencies on the Zn to Se flux ratio.

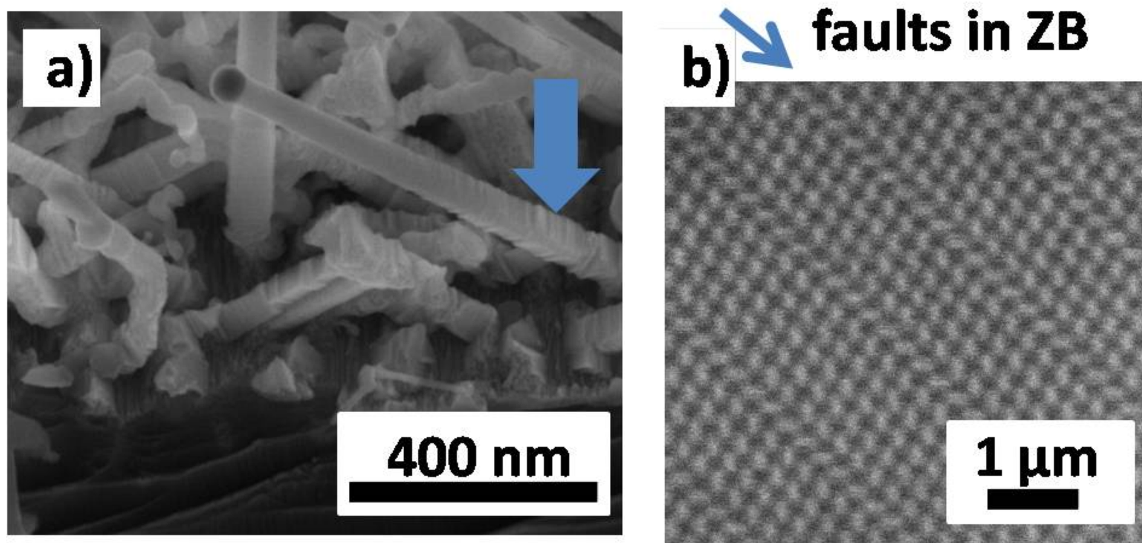

Fig. 4.9: a) SEM image of ZnSe NWs grown in Zn rich conditions with a zick-zack surface at the bottom of the NWs. b) The corresponding HAADF-STEM image of one of these NWs with stacking faults in the zinc blend lattice.

Whereas SEM images show the surface of the NWs, TEM measurements are used to look inside the crystal of the NWs. Fig. 4.9a) shows a SEM image of straight and ordered ZnSe NWs grown under Zn rich conditions and a corresponding HAADF-STEM image of one of these wires in Fig. 4.9b). The HAADF-STEM image shows stacking faults in a zinc blend lattice highlighted with a blue arrow. These stacking faults are already indicated at the zick zack surface of the NWs, highlighted with a second blue arrow in the SEM image in Fig. 4.9a). This zick zack surface is clearly visible at the bottom of the NWs and seems to vanish at the top of the NWs. Therefore further TEM investigation on a single NW are done.

These investigations show that the whole body of the NWs from the bottom to the top reveals ZB and WZ crystal structures. Fig. 4.10A shows a TEM image of the top

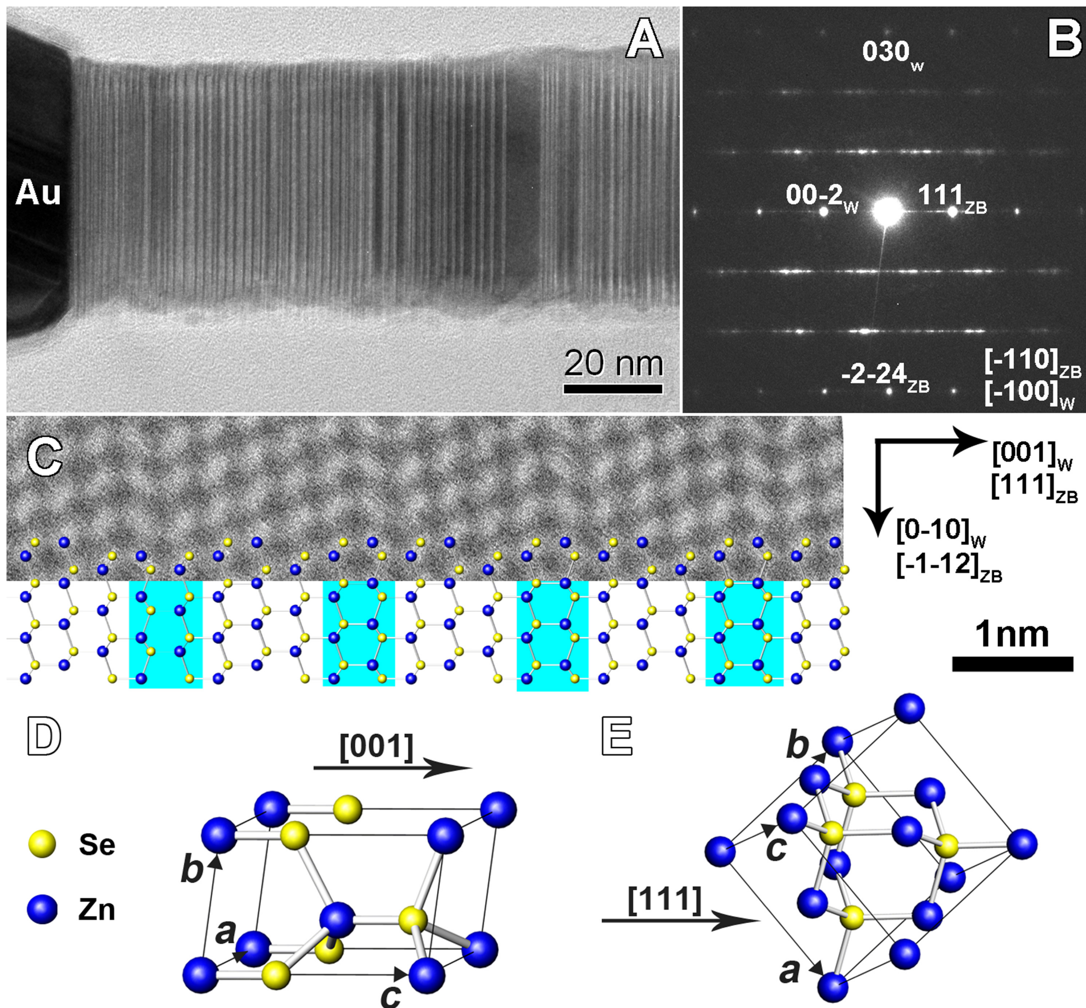

Fig. 4.10: (A) TEM image of a single ZnSe NW, showing a high concentration of stacking faults. The Au-Ga eutectic nanoseed on top of the NW has an amorphous shell. (B) Selected-area electron diffraction pattern of the wire indexing in zinc blend and wurtzite lattices. The distribution of the spots suggests that the wire can be described as a ZB twinned wire grown along the $\langle 111 \rangle$ direction. The diffuse streaks are obtained from the unperiodical domain structure. (C) High-angle annular dark-field scanning transmission electron microscopy image partly overlapped with a sketch of the crystal structure of the wire, showing a distribution of ZB and WZ domains. (D) and (E) are sketches of wurtzite and zinc blend unit cells of ZnSe.

of such a single ZnSe NW. It shows that the concentration of stacking faults is very high even at the top of the NW. It also shows that, the Au-Ga eutectic nanoseed, on top of the NW, has an amorphous shell, the white area around the nanoseed. The corresponding selected-area electron diffraction (SAED) pattern indexing in ZB and WZ lattices is shown in Fig. 4.10B. Referred to the distribution of the spots on the SAED pattern the NW can be described as a ZB twinned NW along the $\langle 111 \rangle$ direction. The diffuse streaks in this pattern indicate that the ZB and WZ domains along the length of the NW are different in size. There is no periodical domain structure. This is already indicated in the TEM image in Fig. 4.10A. To show the distribution of ZB and WZ domains along the length of the NW in detail a high-angle annular dark-field scanning transmission electron microscopy image, which is partly overlapped with a schematic of the crystal structure of the NW, is illustrated in Fig. 4.10C. The ZB domains have a white background and the WZ domains have a blue background. The wurtzite and zinc blend unit cells of ZnSe are shown in Fig. 4.10D and E.

Furthermore, to compare the morphology of thin and thick NWs, TEM measurements on ZnSe NWs grown in Se rich conditions are tried to be done. But these NWs are too thin for ordinary TEM experiments. They vibrate on the supported carbon film because of charging of the wire, which makes it very hard to image them. As a consequence, it is not possible to compare the crystalline quality of the NWs with respect to the Zn to Se flux ratio with TEM during this work.

Because of that we tried to find hints concerning this topic in literature and found the following investigations. In contrast to our observations that ZnSe NWs grown in Zn rich conditions are full of stacking faults Zannier *et al.* report in [Zann 14] that ZnSe NWs grown in Zn rich conditions have a wurtzite crystal structure with the c axes parallel to the growth direction over their entire length and NWs grown in Se rich conditions have also a wurtzite crystal structure but a higher density of stacking faults and a ill-defined growth direction. They claim that independent of the Zn to Se flux ratio the ZnSe NW body consists of stoichiometric ZnSe.

In contrast, our observations show that NWs, grown under Zn rich conditions, are full of stacking faults although their morphology is uniform, straight and ordered, which is congruent with the literature. One reason for the amount of stacking faults could be the diameter of our NWs. The diameter of our NWs is between 50 nm and 100 nm. In [Li 04] they report that the twinning periodicity is linearly proportional to the diameter of the NWs. They say, ZnSe NWs grow along a universal direction, which is perpendicular to the closest packed planes of ZnSe and in cubic ZnSe these are the $\{111\}$ planes.

Concerning this topic, other reports in literature suggest to use a two step growth process for reducing the amount of stacking faults. This two step growth process is a combined growth of NWs and nanoneedles [Aich 08]. In the two step growth process the defect planes are disoriented with respect to the nanoneedle axis, which prohibits that the defects propagate in growth direction. Nevertheless, a disadvantage of this two step growth process is that the NWs are tapered. This is no problem for PL measurements but it is a problem for transport measurements.

Another parameter, apart from the Zn to Se flux ratio, which has an influence on the

crystalline quality, is the growth temperature. This is shown in literature. For example, in [Wang 07], [Cai 08] and [Cai 07] they report that the defect density of a NW can be lowered with the use of a lower growth temperature. But, the experience of this work shows that lower growth temperatures around 400° C cause ZnSe NWs with a bad morphology and as a consequence, it is even impossible to do TEM measurements on these NWs. Because of that, and to get better results concerning the crystalline quality of the NWs without TEM, PLE measurements are also done during this work. The results of these measurements, as well as further PL and transport investigations on ZnSe NWs are summarized and discussed in the next chapter.

Chapter 5

Optical and Transport Investigations of Single ZnSe Nanowires

The requirements on the morphology of NWs are different depending on their applications. For optical investigation ZnSe NWs with embedded CdSe quantum dots are used. The diameter of these NWs is around 10 nm. It is in the order of the exciton Bohr diameter in CdSe, that the carriers in the quantum dots are in a strong confinement regime. In contrast, for transport measurements the diameter of the NWs has to be uniform with a large aspect ratio, to make the NWs suitable as an 1D conducting channel.

5.1 Optical Investigation of ZnSe Nanowires

Concerning their optical applications ZnSe NWs are promising candidates for optoelectronic devices like light-emitting diodes [Knen 04], [Kim 04] or nanolasers [Duan 03]. To modify the electro-optical properties of ZnSe NWs the material composition during growth is changed. It is possible to change the chemical composition along the longitudinal or radial axes. An opportunity to change the chemical composition of ZnSe NWs along the longitudinal axes is the insertion of CdSe quantum dots as photon emitters. Recently, successful incorporation of optical active (Zn,Cd)Se quantum dots into ZnSe NWs has been demonstrated in [Hert 11a]. The embedded quantum dots show single photon emission up to 220 K [Trib 08]. But the polytypism and the high density of stacking faults of ZnSe NWs, already discussed in chapter 4, is a major obstacle for the high performance of optical devices based on ZnSe NWs [Phil 06].

Besides the TEM imaging method, which is widely applied to be the method to gain into a crystal, PL is an important method for measuring the purity and the crystalline quality of semiconductors. Furthermore, the investigations of our group reveal, that photoluminescence excitation spectroscopy (PLE) is a possibility in addition to TEM to get information on the presence of different crystalline modifications in a single NW. These observation also reveal that the ZnSe NWs investigated in this work have a type II band alignement.

5.1.1 Photoluminescence Spectrum of Embedded (Zn,Cd)Se Quantum Dots in As-Grown ZnSe Nanowires

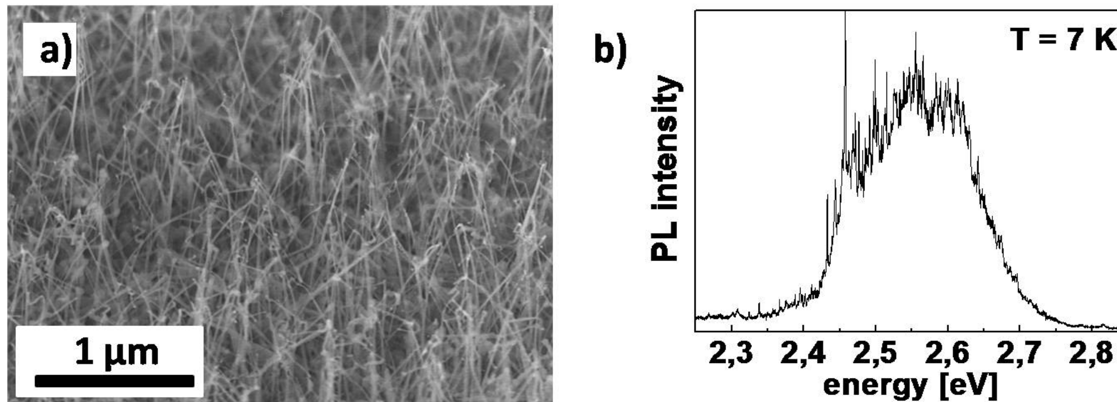

Fig. 5.1: a) SEM image of as-grown ZnSe NWs with embedded CdSe quantum dots. b) PL spectrum of as-grown ZnSe NWs with embedded CdSe quantum dots.

Fig. 5.1a) shows a SEM image of a as-grown ZnSe NW ensemble with embedded CdSe quantum dots. The corresponding PL spectrum is shown in Fig. 5.1b). The spectrum decomposes into an energetically broad ensemble of sharp PL lines at focused optical excitation. The sharp lines of this PL spectrum have their origin in the radiative recombination of neutral or charged excitons or multiexcitons localized in single CdSe quantum dots embedded in single ZnSe NWs and they are not related to impurities. The evidence of this behaviour will be given later.

Further PL investigations on as-grown ZnSe NWs with embedded CdSe quantum dots reveal a energy shift of the broad PL spectrum depending on the average size of the quantum dots. Fig. 5.2a) shows the energy shift of such spectra. The spectra are of ZnSe NW ensembles with embedded quantum dots grown for 20 s, 30 s and 40 s. The PL spectrum for the ZnSe NW ensemble with an embedded quantum dot grown for 20 s is dominated by broad emission lines between 2,25 eV and 2,75 eV. The PL spectrum of the NWs with quantum dots grown for 30 s shows emission lines between 2,15 eV and 2,70 eV and the PL spectrum emitted from the NWs with quantum dots grown for 40 s shows emission lines between 2,05 eV and 2,60 eV. The results exhibit that an increasing Cd content causes a redshift of the PL spectra to lower energies. This is congruent with the band gap relations of ZnSe and CdSe.

But not only the size of the CdSe quantum dot does influence the PL spectrum also the position of the CdSe quantum dot referred to the length of the ZnSe NWs has an influence. To study this in detail, two samples with ZnSe NW ensembles with CdSe quantum dots embedded after 10 min ZnSe growth and after 50 min ZnSe growth were fabricated. Fig. 5.2b) shows the corresponding PL spectra of these two samples.

The black curve in Fig. 5.2b) reveals the spectrum of the ZnSe NW ensemble where the quantum dot is grown on top of the NWs after a ZnSe growth of 50 min. And the

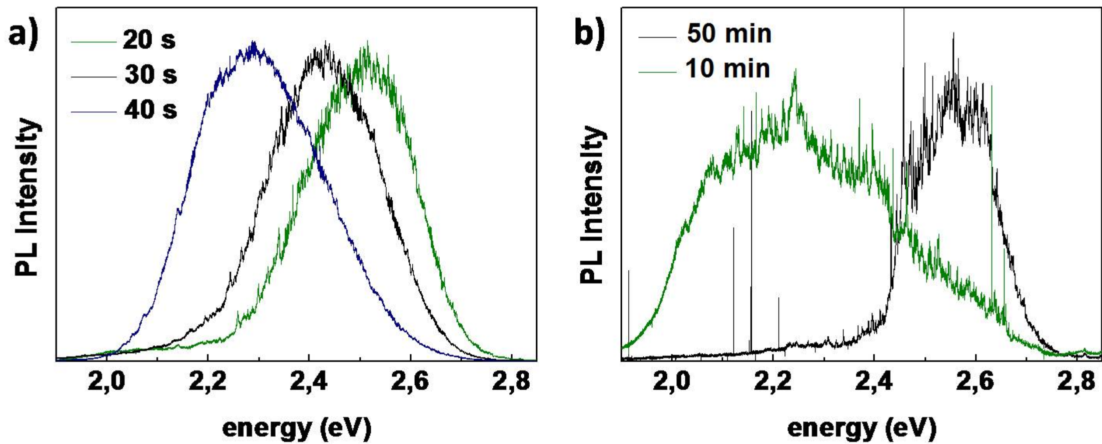

Fig. 5.2: a) PL spectra of as-grown ZnSe NW ensembles with embedded CdSe quantum dots with different dot sizes. The CdSe dots of the green spectrum are grown for 20 s, the ones for the black spectrum for 30 s and those for the blue spectrum for 40 s. b) PL spectra of two as-grown ZnSe NW ensembles with embedded CdSe quantum dots at different positions in the NWs. The black PL spectrum is the spectrum of the ensemble of NWs where the CdSe quantum dots are located at the top of the NWs and the green PL spectrum is the spectrum of those where the CdSe quantum dots are located at the bottom of the NWs.

green curve presents the PL spectrum of the ZnSe NW ensemble where the CdSe quantum dots are grown after 10 min ZnSe growth at the bottom of the NWs. The PL spectrum of the NW ensemble with the CdSe quantum dot at the bottom of the NWs shows emission lines between 1,5 eV and 2,7 eV. The emission lines from the NWs where the quantum dots are embedded at the top of the wires are between 2,4 eV and 2,75 eV. The emission lines in this case are narrower with some really sharp peaks. The sharp lines look like real quantum dot luminescence. In the case of the other emission lines discussed in Fig. 5.2a) and b), it is hard to distinguish if the lines are from real quantum dots or from impurities in the NW body. Because of that, the following investigations are done on ZnSe NWs with CdSe quantum dots embedded at the top of the NWs.

5.1.2 Photoluminescence Spectrum of Embedded (Zn,Cd)Se Quantum Dots in Single ZnSe Nanowires

As mentioned above, the optical transition of the as-grown ZnSe NWs with embedded CdSe quantum dots at the top of the NWs illustrated with the black curve in the PL spectrum in Fig. 5.1b) are related to the radiative decay of neutral or charged excitions or multiexcitons and not to impurities or excitons localized at a structural defect, such as the WZ/ZB junction. This can be verified by the investigation of the dependence of the excitation density and the lattice temperature on the emission intensity of single PL lines of single ZnSe NWs with a embedded CdSe quantum dot.

To study the single NWs with embedded CdSe quantum dots the NWs are mechani-

cally dispersed on a Si substrate. This process is explained in chapter 4. A SEM image of such a single NW is shown in Fig. 5.3a). In most cases, contrary to Fig. 5.3a), they are accumulated and there is more than one NW in the laser focus during a PL measurement, referred to the mechanical dispersion. Because of that, consists the PL spectrum usually of more than one emission line.

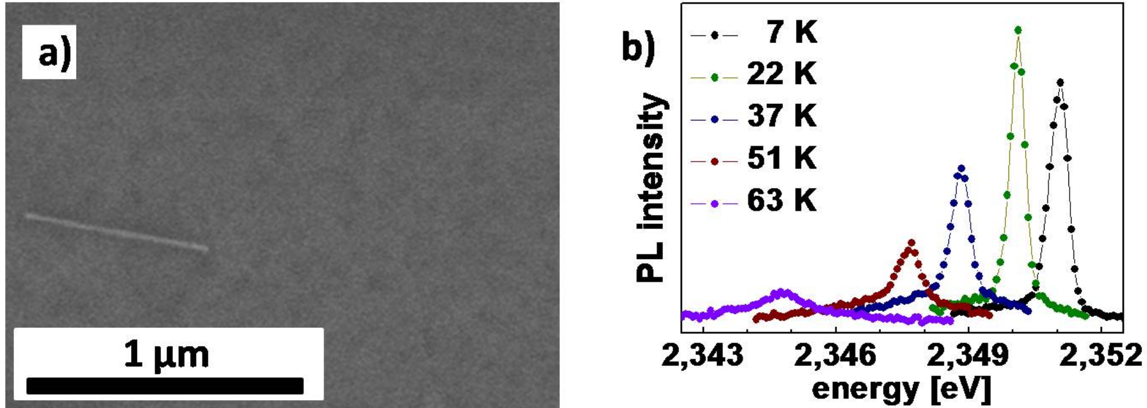

Fig. 5.3: a) SEM image of a single ZnSe NW with a embedded CdSe dot dispersed on a clean Si substrate. b) Temperature evolution of the emission spectrum of a single CdSe quantum dot embedded in a single ZnSe NW.

Fig. 5.3b) shows the corresponding temperature dependent exciton emission of a single quantum dot embedded in a single ZnSe NW. Increasing the sample temperature from 7 K to 63 K exhibits a marked redshift of the emission and a typical line broadening from 500 μeV to 1,5 meV full width at half maximum. This behaviour is comparable to the behaviour of self assembled quantum dots. The redshift has its origin in the material of the quantum dot fundamental band gap and is induced by the temperature evolution of the barrier. The enhanced interaction with acoustic phonons causes the broadening of the emission lines. The emission line at 22 K in Fig. 5.3b), as well as the investigation of further PL lines, exhibit that the emitted PL intensity reaches a maximum at moderate sample temperatures. The PL emission does not decline monotonically as a function of the sample temperature. This behaviour can be explained on the basis of Fig. 5.4.

Fig. 5.4a) shows the dependence of the PL intensity of a representative exciton emission line on the sample temperature in detail and the corresponding quantum dot level energy scheme in b). The quantum dot level energy scheme in Fig. 5.4b) illustrates a split of quantum dot exciton state. The splitting is caused by the electron-hole interaction. State X_B with the angular momentum $J_z = \pm 1$ is an optical active bright state and state X_D with $J_z = \pm 2$ is a dark energetic ground state. At low sample temperatures only bright excitons contribute to PL emission and the dark states are protected against radiative decay by momentum conservation. If the thermal energy of the system becomes comparable to the bright dark energy splitting ΔE, the dark excitons are thermally activated to the bright state. Then the dark excitons contribute to the PL emission.

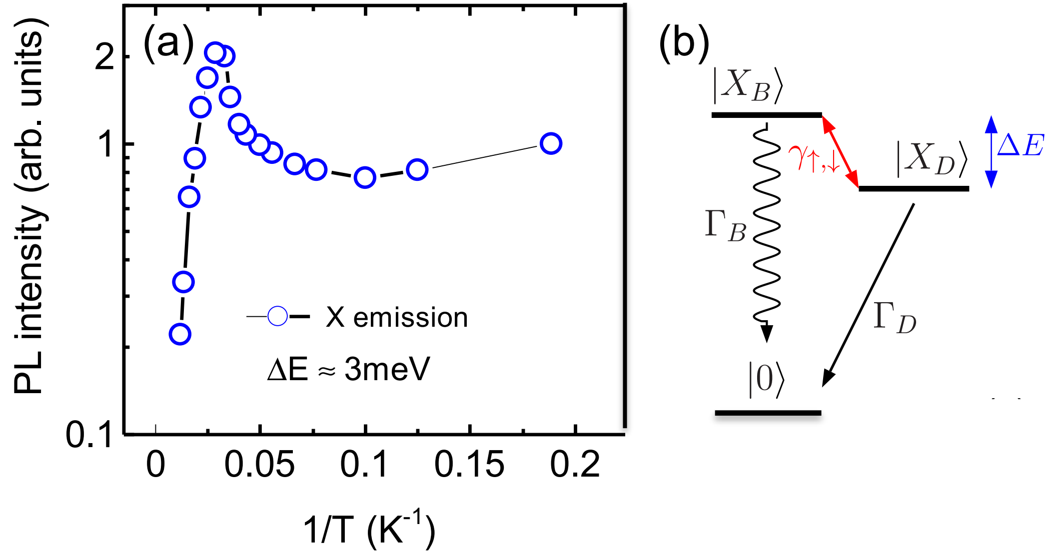

Fig. 5.4: a) Distinct sample temperature dependence of the PL emission. b) Quantum dot energy level scheme.

This repopulation is shown in Fig. 5.4a) with the maximum of the emitted PL intensity at ≈ 35 K estimated to $\Delta E \approx 3$ meV. This corresponds to the bright-dark splitting of CdSe quantum dots embedded in ZnSe NWs [Boun 12] and it is an explanation for the maximum in the temperature dependence of the representative exciton emission line at a moderate sample temperature.

Fig. 5.5b) shows a PL spectrum of a single NW with an embedded CdSe quantum dot. This spectrum shows additional emission lines on the low-energy side of the spectrum with increasing excitation power. Fig. 5.5a) illustrates the excitation density dependence of single emission lines of such a PL spectrum. The blue markers reveal the emission lines which scale linearly with the excitation power and identify the neutral exciton (X) luminescence. Emission lines scaling with larger exponents reveal charged exciton (CX) or biexciton (XX) emission. They are illustrated with black markers in Fig. 5.5a). The different power laws and the dark exciton ground state in the quantum dot energy level scheme of Fig. 5.4b) are the reason that at large excitation densities the biexciton luminescence dominates over the neutral exciton emission. According to the excitation density dependence the low energy lines in Fig. 5.5b) can be identified as biexciton (XX_s) luminescence of two different quantum dots and the high energy lines can be assigned to the radiative decay of neutral excitons (X_s) of two different quantum dots.

The excitation density dependence of the exciton and biexciton emission line as well as the temperature dependence of the exciton emission line confirm that the sharp emission lines of the investigated PL spectra originate from CdSe quantum dots embedded in ZnSe NWs. With the evidence that the PL emission lines of the investigated samples originate from the CdSe quantum dots embedded in ZnSe NWs, the PLE behaviours of these NWs will be studied next.

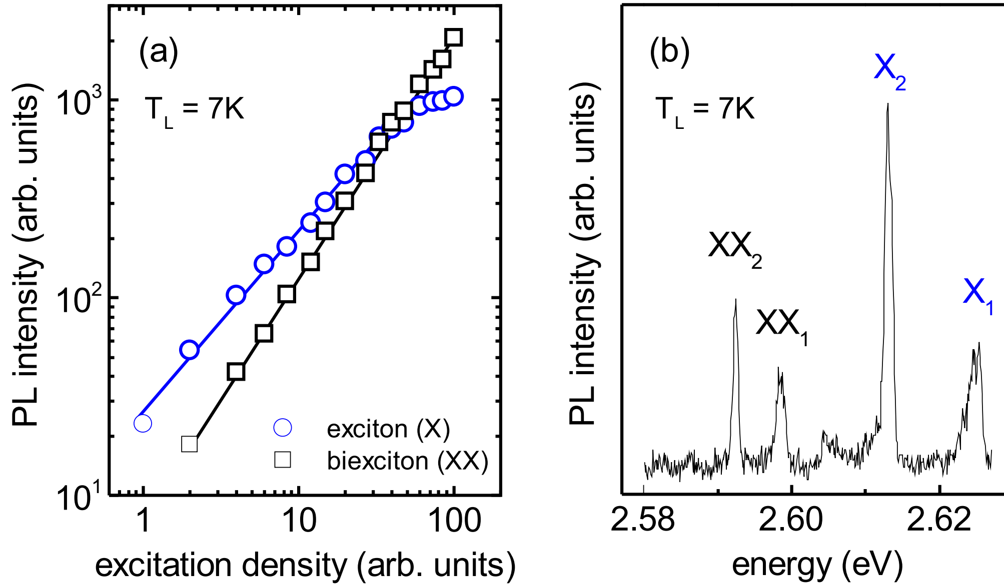

Fig. 5.5: a) Excitation density dependence of single emission lines. b) Lines of a PL spectrum assigned to the radiative decay of neutral excitons (X_s) or biexcitons (XX_s).

5.1.3 Photoluminescence Excitation Spectrum of Single Nanowire Quantum Dots

The photoluminescence excitation (PLE) spectroscopy of embedded CdSe quantum dots in ZnSe NWs studied in this work is used to characterize the polytypic crystal structure of single ZnSe NWs. In contrast to TEM imaging, the characterization method PLE is also applicable to thin NWs $\leq$ 10 nm. Hence, TEM imaging on these NWs is very challenging or nearly impossible, which is already discussed in chapter 4.

Fig. 5.6a) shows a PL/PLE map of two single CdSe quantum dots embedded in two distinct ZnSe NWs and Fig. 5.6b) reveals the corresponding integrated PL intensities of both CdSe quantum dots as a function of the excitation energy. To acquire this map the excitation wavelength of the dye laser is tuned from 4590 Å to 4300 Å in steps of 0,25 Å and the full CCD spectrum is recorded at each wavelength. The horizontal line cuts in the PL/PLE map of Fig. 5.6a) represent PL spectra at a fixed excitation wavelength. The vertical line cuts of this map present excitation spectra at a given detection energy. The verification that the two PL lines originate from two separate quantum dots is given by the analysis of the spectral diffusion [Patt 03].

Studying the PL/PLE map of Fig. 5.6 in detail reveals that excitation energies below the 1s exciton state $E_{X,ZB}$ in cubic ZnSe at 2,80 eV show no PL emission. This is due to the small absorption volume of a single quantum dot. At the fundamental band gap of cubic ZnSe at $E_{g,ZB}$ = 2,82 eV, a broad resonance in the quantum dot PL intensity can be observed. Further tuning of the excitation wavelength to higher excitation energies shows a second resonance at 2,87 eV. This is the excitation energy assigned to the band gap of

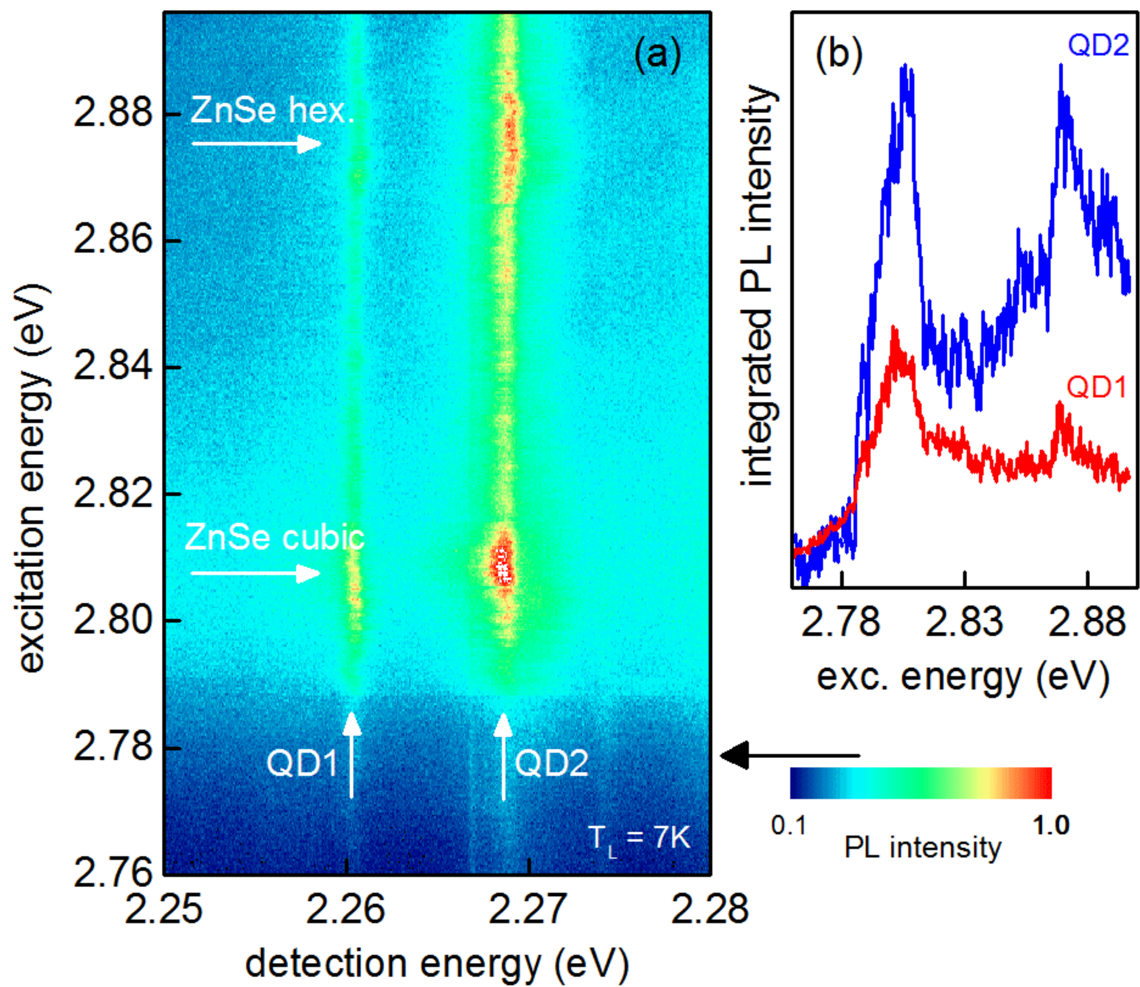

Fig. 5.6: a) PL/PLE map of two single CdSe quantum dots embedded in two distinct ZnSe NWs. b) Integrated PL intensities of the two quantum dots as a function of excitation energy.

the hexagonal ZnSe modification $E_{g,WZ}$ = 2,87 eV. The absorption signatures from both hexagonal and cubic modifications of ZnSe imply that the NWs consist of alternating WZ and ZB domains, which is in agreement with the TEM image in Fig. 4.10 in chapter 4.

Furthermore, it is remarkable that the observed PL emission from the CdSe quantum dots embedded in ZnSe NWs in Fig. 5.6 reveals a resonance at the band gaps of the WZ and ZB modifications of bulk ZnSe. One reason for that is that the $\approx$ 20 meV width of the PLE absorption peaks of our studies involve a small residual deviation from the bulk absorption edges. Here it has to be noticed that, for example, previous studies on highly polytypic InP NWs reveal PL emission at the energetic position of the bulk ZB InP band gap [Bao 08]. This is consistent with the observation of the bulk ZB/WZ absorption edges in the PLE spectrum of this work. Another reason is that the analysis of the conceptual Kronig-Penney models [L Kr 31] shows that the admixture of WZ segments in a predominantly ZB NW body with type II staggered band alignment at the WZ/ZB interfaces leads to a redshift of the fundamental PL transistion [Heis 11]. The radial carrier confinement in the very thin NWs investigated in this work oppose a blueshift to this redshift.

The investigations show that PLE spectroscopy of CdSe quantum dots embedded in ZnSe NWs is a fast and easy characterization method to reveal the polytypic crystal structure of single NWs. Referred to TEM imaging, which is difficult to perform on a daily basis, PLE is an complementary technique that can also be used for thin NWs $\leq$ 10 nm on which TEM imaging is very challanging because of charging and vibration of the NWs during the measurement.

5.1.4 Time-Dependent Quenching of Quantum Dot Photoluminescence in Polytypic ZnSe Nanowires

Independently of the result that PLE spectroscopy can be used for the analysis of the crystal structure of semiconductor NWs, it is difficult to distinguish if the PL signal of a ensemble of NWs is PL of the embedded quantum dot or of impurities of the NWs.

One reason for the difficulties might be the observed time-dependent quenching of the quantum dot PL under cw optical excitation, summarized in Fig. 5.7. To verify this assumption the total, spectrally integrated PL emission from the as-grown NW ensemble is studied. The graphs in Fig. 5.7a) and b) show that a maximum PL emission is recorded when the cw laser source is switched on at 0 s delay. After a few seconds the PL intensity decreases. The decrease is nonexponentially and saturates after a while. This behaviour is shown with the blue curve in Fig. 5.7a). The black curve in Fig. 5.7a) shows the devolution for a ten times increased excitation density. In this case the quenching is faster. The faster quenching with increased excitation densities and the slow time scale of the quenching suggest a charging effect somewhere in the NWs. To recover the PL intensity with thermal cycling or interruption of the laser excitation is not possible.

To rule out that structural damages, like burning the NWs due to the laser heating are responsible for the quenching, the excitation wavelength is tuned below the ZnSe fundamental band gap. It is tuned at 2.80 eV and the NWs are illuminated for several

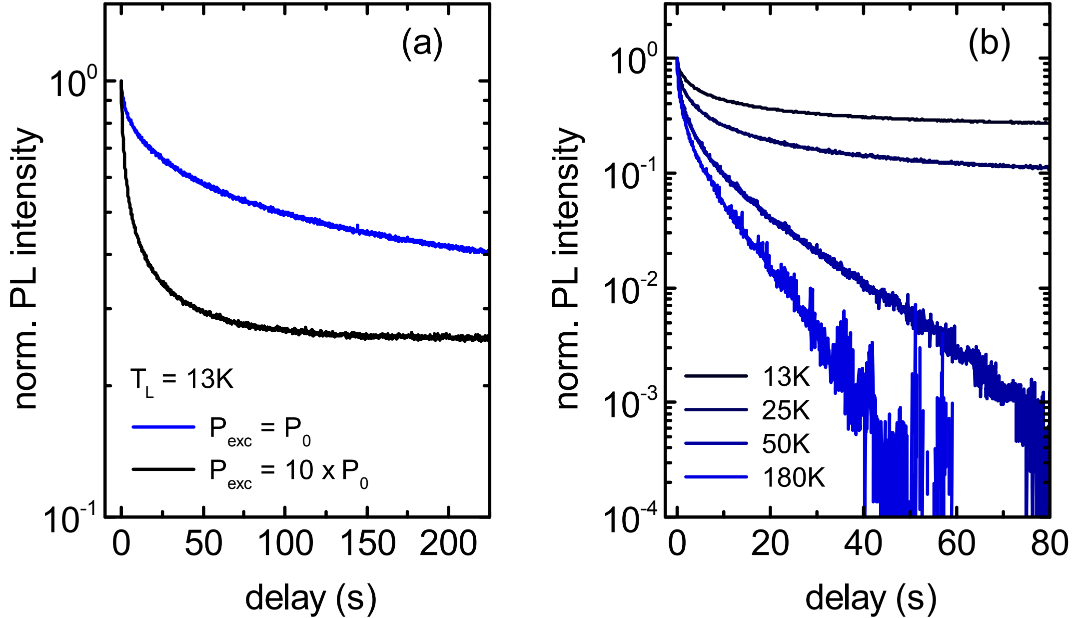

Fig. 5.7: Quenching of the PL emission from as-grown ZnSe NWs with embedded CdSe quantum dots. a) Excitation density dependence of the nonexponential transient PL quenching with a faster quenching at increased excitation densities. b) Sample temperature dependence of the nonexponential transient PL quenching.

minutes at high excitation densities. The results reveal that the detected PL intensity and the time-dependent quenching upon above-band gap excitation is the same with and without previous below-band gap illumination.

Furthermore, reveals the nonexponential transient PL quenching a temperature dependence, which is shown in Fig. 5.7b). The higher the sample temperature, the faster the nonexponential decrease and the longer the delay for saturation. The increasing sample temperatures activate the carriers out of the QD. The thermally activated QD are spatially displaced along the NW axis. The occurring accumulative charge leads to a progressive reduction of the PL saturation level as displayed in Fig. 5.7b).

These observations concerning the PL quenching in the politypic ZnSe NWs suggest a type II band alignment at the WZ/ZB interface. A typ II band alignment is predicted for bulk ZnSe [Mura 94] and for polytypic NWs of different compound semiconductors [Bao 08], [Kusc 14]. The NWs investigated in this work reveal alternating WZ and ZB domains, which are a few nm thin. Due to that, the electron and hole wave functions are delocalized along the wire axis and not defined to a single domain. The free charge carriers which are created with above-band gap optical excitation are captured either by the CdSe quantum dots embedded in the NWs or they are separated due to their axially displaced concentration of their wave functions. If they are captured by the CdSe quantum dot, they contribute to the PL emission. If they are separated, the electrons are concentrated in ZB-rich regions and the holes are concentrated in WZ-rich regions of the NWs [Bao 08]. This spatial separation of electrons and holes, which suppresses the

radiative recombination of the photocarriers, occurs only in a polytypic structure with a staggered typ II band alignment. Without radiative recombination the charging of the NWs increases and leads to a band bending. The band bending causes a depletion of the quantum dots and as a consequence the NWs turn dark and do no longer contribute to the PL spectrum.

In summary reveals the PL quenching process no spectral shift or transformation of the PL spectrum. The charging affinity of individual NWs can not be attributed to the inhomogeneous broadening of the PL emission band in Fig. 5.1 caused by size and composition fluctuations among the quantum dot ensemble. The charging interpretation is confirmed by the excitation density, the excitation wavelength and the lattice temperature dependence of the PL quenching. As already mentioned, the black curve in Fig. 5.7a) reveals an accelerated charging process with increased excitation density. This can be attributed to the amount of free band carriers which increase with increasing excitation density. No charging of the NWs and hence no quenching of the PL emission occurs with below-band gap excitation. Moreover activate elevated sample temperatures out of the QDs, which are tappered at the WZ/ZB interface with staggered type II band alignment. The occurring space charge leads to a band bending and to a depletion of the QDs.

The NWs which are considered in this section concerning their optical properties are all ZnSe NWs with an embedded CdSe quantum dot. Their diameters are ≤ 10 nm and their length is ~ 1 μm. These dimensions are the favourable dimensions of NWs which are used for optical investigation. The dimensions of NWs used for transport measurements are different. This will be pointed out and discussed in the next section.

5.2 ZnSe Nanowires for Transport Measurements

To do transport measurements on single NWs the as-grown NWs are isolated from the growth substrate and ohmic contacts are formed with an elaborated process. The singularization of the NWs is done with different methods, shown in chapter 4. Especially for transport measurements the NWs are isolated in isopropanol and the resulting suspension is transferred with a pipette to a prepared Si substrate. To get an homogeneous distribution of the NWs a spincoater is used to evaporate the excess of isopropanol.

The prepared Si substrates are pre-structured with a coordinate system for localizing the NWs. After the localization of the NWs, contacts for each NW are designed with E-beam lithography and at the end the corresponding metal for the contacts is evaporated. If this process works fine transport measurements would have been done and the transport behaviour of the NWs would have been investigated.

5.2.1 Coordinate Systems to Localize the Single Nanowires

Contacting single NWs for transport measurements is challenging because of their size and the difficulties of defining their position on the substrate during or after singularization. Although there are some interesting approaches referred to the positioning of the NWs

right now, the contact mask for each NW is different and has to be redesigned for every single NW. This is the reason for the fact that E-beam lithography is used. To localize the NWs a localization pattern fabricated with optical lithography covering a 1 cm^2 big piece of a p-doped Si wafer is designed. To have the possibility to use a back gate the p-doped Si-wafer is covered with a 2850 Å thick SiO_2 layer. The deviation of the thickness of the SiO_2 layer is around ± 3 %. The localization pattern on top of this substrate is a kind of coordinate system and shown in Fig. 5.8.

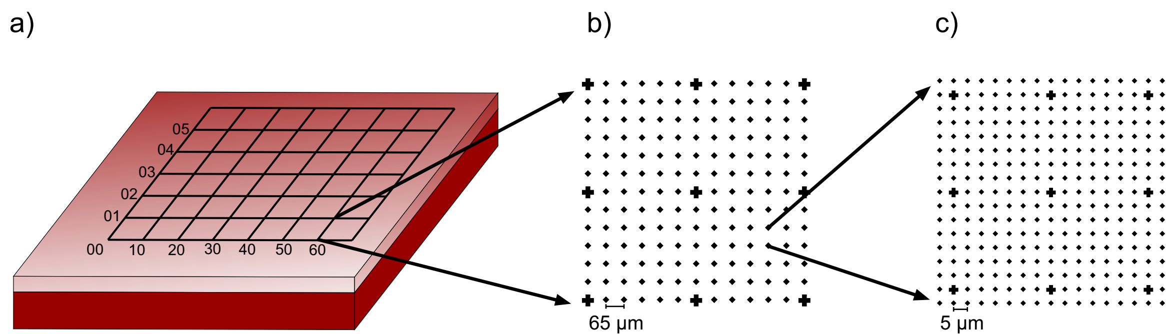

Fig. 5.8: a) Schematic illustration of the silicon substrate with the coordinate system on top. b) The optical lattice of each square of the coordinate system with alignment markers. c) Another fragmentation of the optical lattice done with E-beam lithography for short NWs with a length ≤ 1 μm.

Fig. 5.8a) illustrates the schematic of the coordinate system on top of an 1 cm^2 big piece of a p-doped Si wafer. This coordinate system is a 7×6 grid with a lattice constant of 1 nm. Each square of the 7×6 grid has a lattice with alignment markers. The size of this lattice is 780×780 μm^2 and it is shown in Fig. 5.8b). The distance between the alignment markers is 65 μm. The alignment markers are rhombus-shaped and they have an edge length of 4 μm. For a better orientation there are crosses on every edge, in the middle of every edge length and in the middle of the lattice. The coordinate system and its lattices are formed with optical lithography and finished with a metallization of a 3 nm thick Ti layer and a 30 nm thick Au layer. This system is used for NWs with sizes in the range of the resolution of a optical microscope.

If the NWs are smaller than the resolution of the above mentioned coordinate system, a finer grid is needed. This grid is shown in Fig. 5.8c) and it is a fragmentation of the lattice in Fig. 5.8b). The lattice of Fig. 5.8c) is patterned by E-beam lithography and finished with the same metallization process as the lattice in Fig. 5.8b), a 3 nm thick Ti layer and a 30 nm thick Au layer. The squares of the system in Fig. 5.8c) have an edge length of 1 μm and a distance of 5 μm. In this case the NWs are located with a scanning electron microscope. The advantage of this process is that it offers the possibility to contact very small NWs with diameters around 10 nm and a length shorter than 1 μm, but it has many disadvantages corresponding the stress on the NWs during contacting.

The enabled coordinate systems are the basis to localize small NWs independent of

their dimension. The NWs contacted in this work have the dimension that it is possible to locate them with a optical microscope, to stress the NWs as little as possible during contacting.

5.2.2 Contacts on Single Nanowires

To contact a single NW an electron lithographic method is elaborated. The first step of this method is localizing the NWs. As already mentioned for this step a Si substrate covered with a coordinate system of Au-Ti alignment markers shown in Fig. 5.8 is used. Independent of the fact if the NWs are localized with a optical microscope or a SEM the position of the NWs is determined by four square alignment markers. These alignment markers generate a plane. With the aid of this plane the position of the NWs is defined with an image editing program. The contacts of the NWs, the direct leads, the leads to the bonding pads and the bonding pads itself are designed with the program Elphy Plus of Raith. With this program it is possible to import the square alignment markers, the size and the position of the NWs from the image true to the scale.

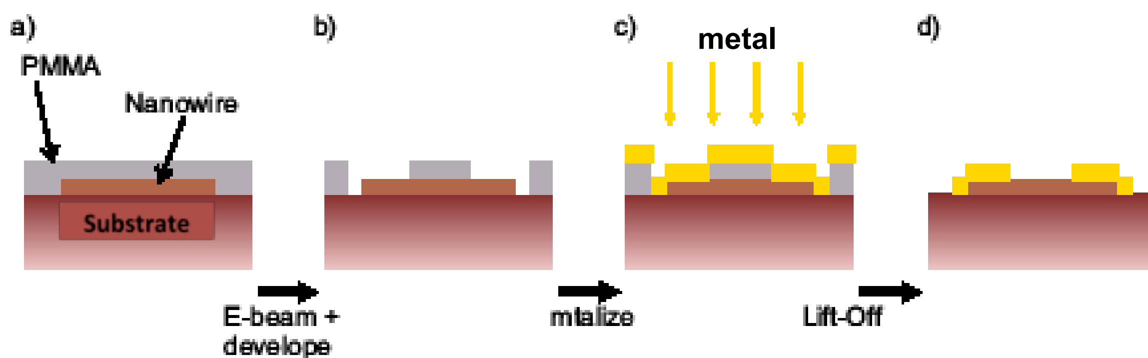

Fig. 5.9: Schematic of the different steps of the Ebeam lithography process. a) Si substrate with a single ZnSe NW covered with a layer PMMA. b) Designed contacts after Ebeam exposure and development. c) Metalization of the whole sample. d) Single NW with contacts after lift off.

Parallel to the design of the contacts the sample with the NWs on top is covered with a photo resist PMMA 950 K 4,5 % Anisol. The thickness of this PMMA layer is 260 nm if it is spin coated with 3000 U/min for 40 s and baked out at 180° C for 2 min. The steps of the Ebeam lithography process are shown in a schematic in Fig. 5.9. Fig. 5.9a) shows the substrate with a NW on top covered with PMMA. The photo resist is needed to define the contacts, the direct leads, the leads to the bonding pads and the bonding pads with E-beam lithography. This is done with 30 kV, a 20 μm aperture and a dose of 512 $\frac{\mu C}{cm^2}$. The exposed structures are developed with a mixture of H_2O and isopropanol for 1 min. The ratio of the mixture is 1 to 3. A schematic of the sample after exposure and development is shown in Fig. 5.9b). The used photo resist is a positive resist. The exposed structures are free of PMMA after development and the residuals of PMMA in Fig. 5.9b) prevent that there is a contact after metallization. To get rid of the oxide

and the PMMA residues at the exposed structures without damaging the NW surface the sample is put in a mixture of HF:H_2O = 1:200 for 5-7 s and rinsed with pure water for 2 min shortly before matallization [Liu 95]. Subsequently the electrical leads are formed by evaporation of metal layers and a lift of procedure, shown in Fig. 5.9c) and d). Fig. 5.9c) reveals the schematic where the whole sample is covered with a metal layer and Fig. 5.9d) shows the sample with a contacted NW. The thickness of the metallization layer has to be as thick as the diameter of the NWs that the whole NWs are covered with metal. In most cases we use 150 nm Al, 10 nm Ti and 30 nm Au. Al is used because of its work function of 4,1 eV which is close to the electron affinity of ZnSe of 4.69 eV [Fijo 96]. Ti is used to prevent a Al-Au alloy. Lift off is done with acetone at 50° C for 30 min. At the end the sample is sticked into a chip carrier with a backside gate for measurements.

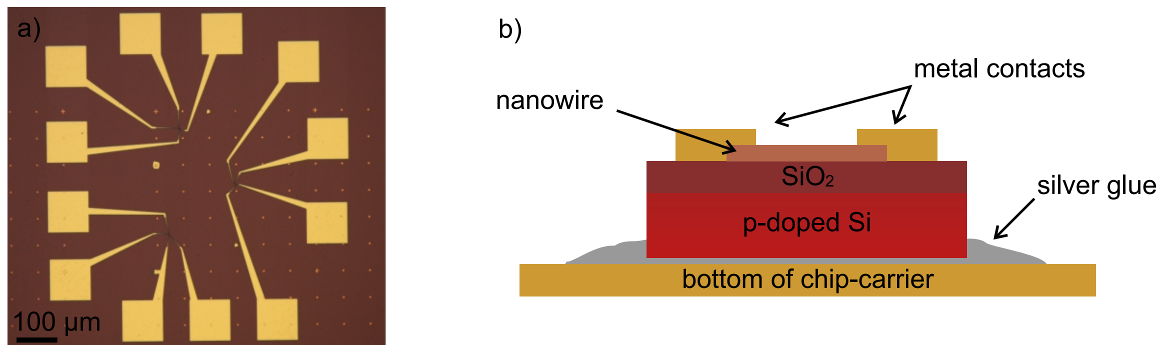

Fig. 5.10: a) NoMarski image of a sample with three NWs, the direct contact, the electrical leads, the leads to the bonding pads and the bonding pads. b) Schematic of the whole sample glued in a chip carrier.

To get an impression of the sample Fig. 5.10a) shows a NoMarski image of the whole sample after contacting. This image illustrates 3 NWs with the direct contacts, the leads, the leads to the bonding pads and the bonding pads and Fig. 5.10b) shows the sample glued in a chip carrier. For the transport measurements discussed in the next section the contacts of the chip carrier are connected with the bonding pads by wires. To create a backside gate one wire is bonded from one contact to the bottom of the chip carrier.

5.2.3 Transport Measurements

The measurements done in this work are all done at room temperature. A schematic of the circuit is shown in Fig. 5.11. Fig. 5.11a) is for bias voltages ±2 V and Fig. 5.11b) for higher bias voltages. The voltage channel around the sample in Fig. 5.11a) is for the backside gate. The additional resistance in series with the gate voltages limits the current in the case of a breakthrough of the SiO_2 insulating layer. It is a 1 GΩ resistance. To apply a higher voltage than the maximum ±10 V of the voltage card a voltage amplifier is added for some measurements.

The circuit in Fig. 5.11b) is for bias voltages higher than ±2 V with the assumption that the ratio between the resistances of the sample and the resistance in series is consis-

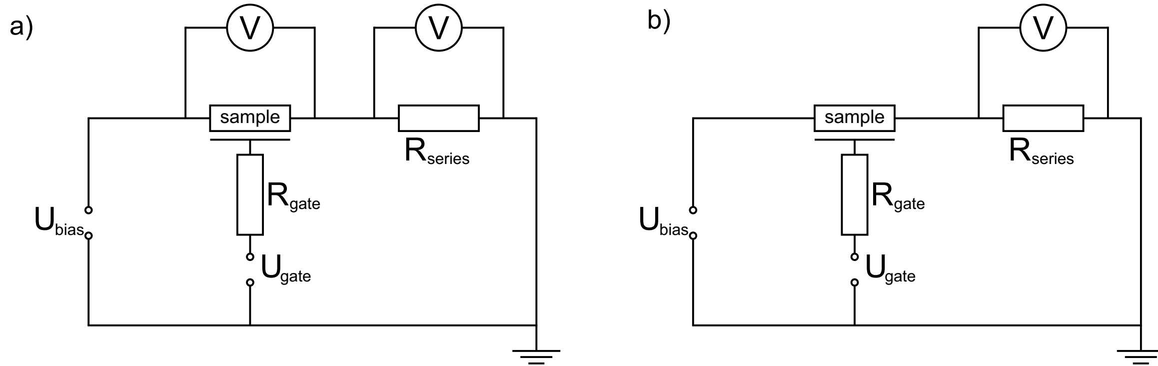

Fig. 5.11: Schematic of the measurement setup a) for bias voltages up to ±2 V and b) higher bias voltages.

tent with a voltage drop at the resistance in series not more than 2 V for all bias voltages. The voltage amplifier can be used further on. The current is calculated with the voltage drop on the resistance in series. A voltage measurement on the sample is not possible with this circuit.

To start the transport measurements, it is necessary, in any case, to check the SiO_2 with regards to its insulating behaviour. To check these behaviours a voltage is applied on the gate and the voltage drop at the gate and a 1 GΩ resistance in series is measured. The resistance of the 285 nm thick SiO_2 layer is 100 GΩ for a ±10 V range. The insulating layer tolerates ±70 V by room temperature without any breakthrough. By reference to this leakage current through the gate it is possible to interpret the transport measurements on the NWs. Even, if the NWs are not conducting, there is a leakage current through the SiO_2 layer. The resistance of the wire is in this case at least 100 kΩ. And, as long as the distance between two contacts is around 200 nm in the range of the thickness of the SiO_2 layer, the leakage current between two contacts will be in the same range as the gate leakage current.

It is possible that the results for the measured leakage currents are limited by the values of the measurement setup. To check this the resistance in series and the 1:1 voltage amplifier are replaced by a current amplifier. The current amplifier regulates the current down like it generates a virtual ground state and the amplifier reveals a corresponding opposite directed current. The voltage of this current is measured by a digital multimeter. Now it is possible to measure a current in the range of pA. The measurements depending on the leakage current through the oxide layer done with this circuit confirm the measurements with the 1:1 voltage amplifier. The results of the measurements of the resistance between two contacts are the same as the results measured with the 1:1 voltage amplifier.

For all these measurements, it has to be considered that a leakage current through the current amplifier, caused by the gate voltage, limits the accuracy of the current measurement. The operating range of the current amplifier is adjusted in relation to the output voltage during the measurement. The output voltage should not reach the full-scale deflection of the current amplifier as well as the leakage current. That means the

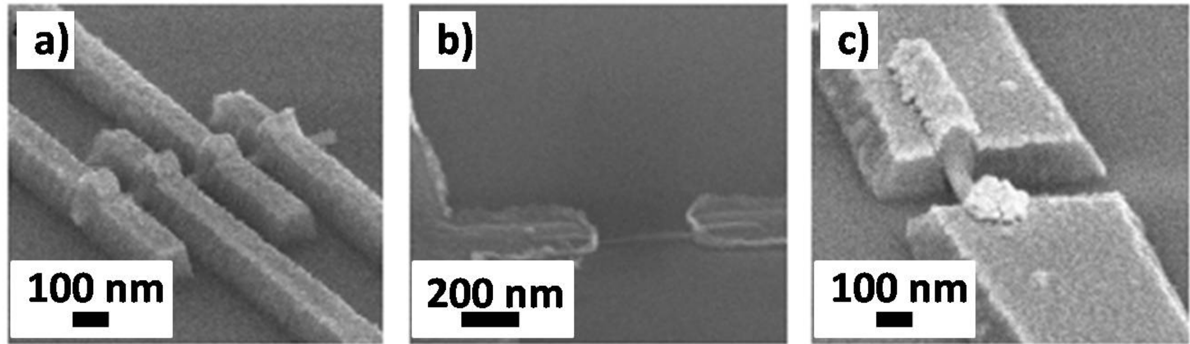

Fig. 5.12: SEM images of several ZnSe NWs with different contacts. a) ZnSe NW with a 4 point contact. b) and c) ZnSe NWs with 2 point contacts. The NWs in a) and c) are grown in Zn rich conditions at 480° C and the NW in b) is grown in Se rich conditions at 480° C.

gate voltage limits the accuracy of the measurement.

Based on the circuit in Fig. 5.11 and the above mentioned settings, measurements on different NWs were done. The measurements were done on ZnSe NWs grown in Zn rich conditions with diameters between 40 nm and 60 nm, as well as on NWs grown in Se rich conditions with diamters $\leq$ 10 nm, and 2 point, as well as 4 point contacts are elaborated. SEM images of three samples with different NWs and several contacts on top are shown in Fig. 5.12. Fig. 5.12a) is a SEM image of a single NW grown in Zn rich conditions with 4 contacts, Fig. 5.12b) shows a NW grown in Se rich conditions with 2 contacts and Fig. 5.12c) shows a NW grown in Zn rich conditions with 2 contacts. The results of the measurements on these samples exhibit that it is a big challenge to do transport measurements on ZnSe NWs. There are different reasons based on the contact resistance why this is so hard. First of all the size of the NW and the size of the contact area are very important for the calculation of the resistance. The resistance between two contacts is nearly the sum of the two contact resistances at the metal ZnSe interface and the resistance of the NW between these contacts. Fig. 5.12a) shows a 40 nm thick ZnSe NW with four Al/Ti/Au contacts. The contacts are 200 nm thick and the distance between the contacts is 100 nm. The contact area of this wire is approximately $A_c \approx 1.3 \cdot 10^{-10}$ cm^2, if the upper part of the cylinder of the wire is contacted. The corresponding resistance is $R_c = \rho_c \cdot 8.0 \cdot 10^9$ cm^2. For a wire with $A \approx 1.3 \cdot 10^{-11}$ cm^2 is the resistance $R = 1.6 \cdot 10^6$ cm^{-1}. To get a feeling for the effect of the dimension of the NW on the resistance, the intrinsic resistance $\rho_c = 10^{-3}$ Ωcm^2 for highly doped ZnSe layers is inserted in this equation [Slob 03]. The results show a minimum contact resistance of 8 MΩ for such a ZnSe NW.

But not only the dimension of the contacts determines the high contact resistance. The ex-situ contacts could be another reason. It is not possible to contact the NWs in-situ compared to the contacts on small ZnSe structures shown in [Slob 03]. Although the Au nanoseed on top of each NW is a in-situ contact, it has no influence on the contact resistance. This in-situ contact together with an ex-situ contact is used in Fig. 5.12c). Based on the oxidation problem of the ex-situ contacts hydrofluoric acid was used before

contacting without any improvement concerning the contact resistance.

Besides the nature of the contacts the used metal has a significant influence on the barrier between the NW and the contact, too. In most cases Al is used for contacting, because of the potential barrier of Al on ZnSe which is lower than the potential barrier of Au on ZnSe [Swan 69]. As long as undoped ZnSe NWs are studied in this work the Al contact might not be a problem. But as soon as iodine is used for doping the ZnSe NW, it has to be considered that iodine has not only an influence on the conductance of the wire but also on the Al contact.

Independent of the used Al, the value of the intrinsic resistance is dependent on the doping of the material. On highly doped ZnSe ohmic contacts are possible. With a decreasing doping, rises the contact resistance [Miya 92]. Undoped ZnSe has resistance values in the range $\rho > 10^4$ Ωcm [Yone 84]. With the above mentioned dimensions of the NWs the resistance of a NW is around 100 GΩ. The resistance of the SiO_2 layer is in the same range. So, undoped ZnSe NWs could be another reason for the lack of transport measurements. Because of that we also measured NWs with a ZnSe:I shell around the ZnSe NWs, but the measurement on these NWs does not change anything compared to the leakage current.

Another factor is the crystal quality of the ZnSe NWs investigated in this work. As already discussed they are full of stacking faults. This might also be a problem for transport measurements.

Although the transport measurements done during this work are not reproducible right now, we were able to start the measurements on our ZnSe NWs, because of the elaborated contacts. We presented a method to contact single NWs independent of their size and the next step should be the control of the morphology or the crystalline quality of the NWs with the aid of transport measurements.

Chapter 6

Summary

In the present PhD thesis the control of the morphology, such as the diameter, the length, the orientation, the density, and the crystalline quality of 1D ZnSe NWs grown by MBE for optical and transport applications has been achieved. The basic information and the experimental techniques used during this work are presented in chapter 1 and 2.

The investigated ZnSe NWs are gown on Si doped GaAs substrates with Au-Ga nanoseeds as catalyst. The investigations showed that the morphology of the ZnSe NWs is mostly determined by the size of the Au-Ga nanoseeds. So the nanoseed formation process was investigated in detail for different Au layer thicknesses, for different dewetting temperatures and times, summarized in the first experimental part of this thesis in chapter 3. It has been found, that the thickness of the Au layer has the main influence on the diameter and the density of the Au-Ga nanoseeds. The thicker the Au layer the thicker the diameter of the nanoseeds and the lower the density of them. But it has to be considered that there is a relation between the diameter and the density of the nanoseeds. It is not possible to tune the density of the nanoseeds independent of their diameter with the Au layer thickness, the dewetting temperature or the dewetting time. Because of that, Ga free catalyst particles and the effect of the NW materials on the quantitative formation of the nanoseed has been investigated. At the end, it has been found that it is possible to lower the density of the nanoseeds independent of their diameter with a cap layer of Te or Zn on top of the Au layer during the dewetting process.

The next experimental part, the optimization of the NWs itself, is illustrated in chapter 4. As already mentioned it has been found that the diameter and the density of the NWs is mostly determined by the diameter and the density of the Au-Ga nanoseeds. Further investigations showed that the morphology of the ZnSe NWs is also determined by the growth temperature, the Zn to Se flux ratio, the growth rate, the growth time and the substrate orientation. It has been found that the Zn to Se flux ratio is another crucial parameter. The Zn to Se flux ratio determines if the NWs are straight, ordered and oriented, or not. The other parameters, such as growth rate, growth time and substrate orientation, have no significant influence on the growth of the NWs as long as the Zn to Se flux ratio is optimal. To achieve these dependencies the NWs are studied by RHEED observations in-situ during growth and ex-situ by the observation of SEM images. The

investigation of TEM images exhibits that the crystal of the ZnSe NWs is full of stacking faults.

The last chapter of this thesis, chapter 5, is concentrated on optical and transport applications. For optical measurements special ZnSe NWs with a diameter $\leq$ 10 nm and a length of around 1 μm with and without CdSe nanoinclusions have been grown. The measurements showed that these inclusions are embedded optical active CdSe quantum dots with a energetic structure, which is comparable to that of conventional self-assembled QDs. Furthermore, reveals the excitation spectrum the presence of ZB and WZ modifications of ZnSe, which is in line with the polytypic crystal structure seen in TEM imaging and it has been shown that the polytypic ZnSe NWs have a staggered type II band alignment at the WZ/ZB interface.

Another approach was used for growing ZnSe NWs for transport measurements. Concerning this topic a process of singularization, a localization pattern and a contacting process was developed. Dependent on the size of the NWs there are two ways to singularize and locate the NWs on the localization pattern. The contacts of these NWs and their leads are designed, defined with E-beam lithography and formed with the evaporation of metal layers. First measurements with NWs of different size and with different measurements configurations have been done. During these measurements some difficulties were arising, for example, with the reproducibility of these measurements. Thus, our group started to investigate NWs of other materials. Based on the investigations, concerning the formation of the Au-Ga nanoseeds, done during this work, they started to elaborate and study CdTe NWs with a HgTe shell.

To sum up the perceptions concerning the dependencies of the different investigated parameters on the formation of the nanoseeds and the main dependencies during the NWs growth can be used as a basis for the NW growth independent of the NW material. Furthermore, it is possible to control the growth and the morphology of ZnSe NWs with the elaborated dependencies. It is possible to grow NWs with diameters $\leq$10 nm or with diameters of 60 nm with different length. These NWs are ordered and oriented with respect to the substrate. But the crystalline quality of the ZnSe NWs should be improved especially for transport measurements.

Zusammenfassung

Diese Doktorarbeit beschäftigt sich mit dem Wachstum und der Charakterisierung von ZnSe Nanodrähten. Das Ziel dieser Arbeit ist es, sowohl die Morphologie, d.h. den Durchmesser, die Länge, die Orientierung und die Dichte der ZnSe Nanodrähte, als auch deren Kristallqualität für optische Anwendungen und Transportmessungen zu kontrollieren. Die verwendeten Grundlagen und experimentellen Techniken werden in Kapitel 1 und 2 erklärt.

Die untersuchten ZnSe Nanodrähte sind auf Silizium dotierten GaAs Substraten gewachsen. Die Forschungsarbeiten an diesen Drähten haben gezeigt, dass die Morphologie der Nanodrähte hauptsächlich durch die Größe der Au-Ga nanoseeds bestimmt wird. Daher wurde der Prozess in dem die Au-Ga nanoseeds geformt werden im Detail, für verschiedene Goldschichtdicken, für verschiedenen dewetting Temperaturen und Zeiten, beobachtet. Die Ergebnisse dieser Untersuchungen werden im ersten experimentellen Teil in Kapitel 3 zusammengefasst. Die Dicke der Goldschicht hat den meisten Einfluss auf den Durchmesser und die Dicht der Au-Ga nanoseeds. Je dicker die Goldschicht ist umso größer ist der Durchmesser der Au-Ga nanoseeds und umso geringer ist deren Dichte. Des Weiteren ist aufgefallen, dass es eine Beziehung zwischen dem Durchmesser der Au-Ga nanoseeds und deren Dichte gibt. Es ist nicht möglich die Dichte der Au-Ga nanoseeds, mit Hilfe der Goldschichtdicke, der dewetting Temperatur oder Zeit, unabhängig von deren Durchmesser zu verändern. Daher wurden sowohl nanoseeds ohne Gallium als auch der Einfluss der einzelnen Materialien, die zum Nanodrahtwachstum benötigt werden, auf die Bildung der nanoseeds untersucht. Als Ergebnis wurde gezeigt, dass man die Dichte der nanoseeds unabhngig von ihren Durchmessern mit Hilfe einer Tellur oder Zink Lage auf der Goldschicht während des dewetting Prozesses verändern kann.

Der zweite Experimentelle Teil, die Optimierung der Nanodrähte, ist in Kapitel 4 zusammengefasst. Wie bereits erwähnt wird der Durchmesser und die Dichte der Nanodrähte hauptsächlich durch den Durchmesser und die Dichte der Au-Ga nanoseeds bestimmt. Weitere Untersuchungen haben ergeben, dass die Morphologie der ZnSe Nanodrähte auch durch die Wachstumstemperatur, das Flussverhältnis von Zink und Selen, die Wachstumsrate und die Orientierung des Substrates bestimmt wird. Das Flussverhältnis von Zn und Se bestimmt ob die Nanodrähte gerade, orientiert und in eine bestimmte Richtung wachsen oder nicht. Die anderen Parameter, wie die Wachstumstemperatur, die Wachstumsrate oder die Orientierung des Substrates haben keinen signifikanten Einfluss auf das Wachstum der Nanodrähte, wenn das Flussverhältnis von Zn und Se, das Richtige ist. Die gefundenen Abhängigkeiten wurden mit Hilfe von RHEED Beobachtungen in-situ

während des Wachstums und ex-situ mit der Interpretation von SEM Bildern gefunden. Zudem haben TEM Untersuchungen gezeigt, dass die Nanodrähte voll von Versetzungen sind.

Das letzte Kapitel, Kapitel 5 beschäftigt sich sowohl mit der optischen Anwendung von ZnSe Nanodrähten als auch mit Transportmessungen an diesen ZnSe Nanodrähten. Für die optischen Untersuchungen wurden ZnSe Nanodrähte mit einem Durchmesser $\leq$10 nm und einer Länge von ungefähr 1 μm mit und ohne CdSe Unterbrechungen gewachsen. Die Messungen haben gezeigt, dass die Unterbrechungen optisch aktive CdSe Quantenpunkte sind. Die energetische Strucktur dieser Quantenpunkte ist vergleichbar mit der energetischen Struktur von konventionellen selbst organisierten Quantenpunkten. Das Anregungsspektrum dieser Quantenpunkte weist sowohl Zinkblende als auch Wurtzit Modifikationen von ZnSe auf. Das ist in Übereinstimmung mit den polytypischen ZnSe Nanodrähten, die die TEM Bilder zeigen. Des Weiteren zeigen die polytypischen ZnSe Nanodrähte ein Typ II band alignment am Wurtzit Zinkblende Übergang.

In dieser Arbeit wurden nicht nur Nanodrähte für optische Messungen gewachsen sondern auch Nanodrähte für Transportmessungen. Für die Transportmessungen wurde ein Prozess zum vereinzeln der Nanodrähte, ein Koordinatensystem zur Lokalisierung der Nanodrähte und ein Prozess zum Kontaktieren der Nanodrähte entwickelt. Abhängig von der Größe der Nanodrähte wurden sowohl zwei Methoden gefunden um die Drähte zu vereinzeln als auch zwei Koordinatensysteme entwickelt um die Drähte zu lokalisieren. Die Kontakte wurden entwickelt, mit E-beam Lithographie definiert und anschließend mit aufdampfen von Metall geformt. Mit Hilfe der Kontakte wurden erste Messungen an verschieden großen Drähten und in verschiedenen Messkonfigurationen untersucht. Während dieser Messungen sind Probleme aufgetreten, unter anderem mit der Reproduzierbarkeit dieser Messungen. Aus diesem Grund wurden auch Nanodrähte aus anderen Materialien untersucht. Mit der Hilfe, des in dieser Arbeit entwickelten Prozesses zur Bildung der Au-Ga nanoseeds wurden CdSe Nanodrähte mit einem HgTe Mantel entwickelt und untersucht.

Zusammenfassend wurde in dieser Dissertation gezeigt, dass sowohl die gefundenen Abhängigkeiten von den untersuchten Parameter bei der Bildung der Au-Ga nanoseeds, als auch die gefundenen Abhängigkeiten von bestimmten Parametern während des Wachstums der Nanodrähte, als Basis für das Wachstum von Nanodrähten unabhängig vom Material verwendet werden können. Des Weiteren kann mit den gefundenen Abhängigkeiten das Wachstum und die Morphologie von ZnSe Nanodrähten kontrolliert werden. Es können ZnSe Nanodrähte mit Durchmessern $\leq$10 nm oder mit Durchmessern von 60 nm mit unterschiedlichen Längen, geordnet und in eine bestimmte Richtung orientiert gewachsen werden. Die Kristallqualität der ZnSe Nanodrähte muss dennoch verbessert werden, vor allem in Bezug auf Transportmessungen.

Bibliography

[Ahu 03] Y. Ahu and Y. Bando. *Chem. Phys. Lett.*, Vol. 377, p. 361, 2003.

[Aich 08] T. Aichele, A. Tribu, C. Bougerol, K. Kheng, R. Andre, and S. Tatarenko. *Applied Physics Letters*, Vol. 93, No. 143106, pp. 1 – 4, 2008.

[Aich 09] T. Aichele, A. Tribu, G. Sallen, J. Bocquel, E. Bellet-Amalric, C. Bougerol, J.-P. Poizat, K. Kheng, R. Andr, S. Tatarenko, and H. Mariette. *Journal of Crystal Growth*, Vol. 311, pp. 2123 – 2127, 2009.

[Appe 08] J. Appenzeller, J. Knoch, M. T. Bjrk, H. Riel, H. Schmid, and W. Riess. *IEEE Transactions on Electron Devices*, Vol. 55, No. 11, pp. 2827 – 2845, 2008.

[Arno 03] M. S. Arnold, P. Avouris, Z. W. Pan, and Z. L. Wang. *The Journal of Physical Chemistry B*, Vol. 107, pp. 659 – 663, 2003.

[Bao 08] J. Bao, D. C. Bell, F. Capasso, J. B. Wagner, T. Martensson, J. Trgardh, and L. Samuelson. *Nano Letters*, Vol. 8, No. 3, pp. 836 – 841, 2008.

[Basu 08] J. Basu and R. Divakar. *Journal of Applied Physics*, Vol. 104, No. 064302, pp. 1 – 8, 2008.

[Bell 10] E. Bellet-Amalric, M. Elouneg-Jamroz, C. Bougerol, M. D. Hertog, Y. Genuist, S. Bounouar, J. Poizat, K. Kheng, R. Andre, and S. Tatarenko. *Physica Status Solidi C*, Vol. 7, No. 6, pp. 1526 – 1529, 2010.

[Bell 12] E. Bellet-Amalric, M. Elouneg-Jamroz, P. Rueda-Fonseca, S. Bounouar, M. D. Hertog, C. Bougerol, R. Andr, Y. Genuist, J. Poizat, K. Kheng, J. Cibert, and S. Tatarenko. *Journal of Crystal Growth*, Vol. 378, pp. 233 – 237, 2012.

[Boun 12] S. Bounouar, C. Morchutt, M. Elouneg-Jamroz, L. Besombes, R. Andr, E. Bellet-Amalric, C. Bougerol, M. D. Hertog, K. Kheng, S. Tatarenko, and J. P. Poizat. *Physical Review B*, Vol. 85, No. 035428, pp. 1 – 6, 2012.

[Brau 99] W. Braun. *Springer Tracts in Modern Physics*, Vol. 154, 1999.

[Cai 05] Y. Cai, S. Chan, I. Sou, Y. Chan, D. Su, and N. Wang. *Materials Research Society Symposium*, Vol. 838E, pp. 014.11.1 – 014.11.6, 2005.

[Cai 06] Y. Cai, S. Chan, I. Sou, Y. Chan, D. Su, and N. Wang. *Advanced Materials*, Vol. 18, pp. 109 – 114, 2006.

[Cai 07] Y. Cai, S. K. Chan, I. K. Sou, Y. F. Chan, D. S. Su, and N. Wang. *Nano Micro Small*, Vol. 3, No. 1, pp. 111 – 115, 2007.

[Cai 08] Y. Cai, T. L. Wong, S. K. Chan, I. K. Sou, D. S. Su, and N. Wang. *Applied Physics Letters*, Vol. 93, No. 233107, pp. 1 – 3, 2008.

[Chan 06] S. K. Chan, Y. Cai, N. Wang, and I. K. Sou. *Applied Physics Letters*, Vol. 88, No. 013108, pp. 1 – 3, 2006.

[Chan 07] S. K. Chan, Y. Cai, N. Wang, and I. K. Sou. *Journal of Crystal Growth*, Vol. 301 – 302, pp. 866 – 870, 2007.

[Chan 08] S. K. Chan, S. K. Lok, G. Wang, Y. Cai, Y. J. Wang, N. Wang, and I. K. Sou. *Appl. Phys. Lett.*, Vol. 92, No. 183102, pp. 1–3, 2008.

[Chau 00] C. Chauvet, E. Tournie, and J.-P. Faurie. *Physical Review B*, Vol. 61, No. 8, pp. 5332 – 5336, 2000.

[Chen 09] C. Cheng and Y. Chen. *Materials Chemistry and Physics*, Vol. 115, pp. 158 – 160, 2009.

[Chua 13] S. Chuang, Q. Gao, R. Kapadia, A. C. Ford, J. Guo, and A. Javey. *Nano Letters*, Vol. 13, pp. 555 – 558, 2013.

[Coll 05] A. Colli, S. Hofmann, A. C. Ferrari, C. Ducati, F. Martelli, S. Rubini, S. Cabrini, A. Franciosi, and J. Robertson. *Applied Physics Letters*, Vol. 86, No. 153103, pp. 1 – 3, 2005.

[Cui 00] Y. Cui, X. Duan, J. Hu, and C. M. Lieber. *The Journal of Physical Chemistry B*, Vol. 104, No. 22, pp. 5213 – 5216, 2000.

[Cui 01] Y. Cui, J. Lauhon, M. S. Gudiksen, J. Wang, and C. M. Lieber. *Applied Physics Letters*, Vol. 78, No. 15, pp. 2214 – 2216, 2001.

[Cui 03] Y. Cui, Z. Zhong, D. Wang, W. U. Wang, and C. M. Lieber. *Nano Letters*, Vol. 3, No. 2, pp. 149 – 152, 2003.

[Dick 08] K. A. Dick. *Progress in Crystal Growth and Characterization of Materials*, Vol. 54, No. 3-4, pp. 138 – 173, 2008.

[Duan 03] X. Duan, Y. Huang, R. Agarwal, and C. M. Lieber. *Nature (London)*, Vol. 421, pp. 241 – 245, 2003.

[Elli 81] R. P. Elliot and F. A. Shunk. *Journal of Phase Equilibria*, Vol. 2, No. 3, pp. 356 – 358, 1981.

[Fan 05] Z. Y. Fan and J. G. Lu. *Applied Physics Letters*, Vol. 86, No. 123510, pp. 1 – 3, 2005.

[Fan 08] Z. Y. Fan, J. C. Ho, Z. A. Jacobson, R. Yerushalmi, R. L. Alley, H. Razavi, and A. Javey. *Nano Letters*, Vol. 8, No. 1, pp. 20 – 25, 2008.

[Fijo 96] J. F. Fijo and P. H. Holloway. *Critical Reviews in Solid State and Materials Sciences*, Vol. 21, No. 2, pp. 77–128, 1996.

[Giva 75] E. I. Givargizov. *Journal of Crystal Growth*, Vol. 31, pp. 20 – 30, 1975.

[Gudi 02] M. S. Gudiksen, L. J. Lauhon, J. Wang, D. Smith, and C. M. Lieber. *Nature*, Vol. 415, pp. 617 – 620, 2002.

[Hayd 08] O. Hayden, R. Agarwal, and W. Lu. *Nano Today*, Vol. 3, No. 5-6, 2008.

[Heis 11] M. Heiss, S. Conesa-Boj, J. Ren, H.-H. Tseng, A. Gali, A. Rudolph, E. Uccelli, F. Peiro, J. R. Morante, D. Schuh, E. Reiger, E. Kaxiras, J. Arbiol, and A. F. i Morral. *Physical Review B*, Vol. 83, No. 045303, pp. 1 – 10, 2011.

[Herm 89] M. A. Herman and H. Sitter. *Springer Verlag*, 1989.

[Herm 96] M. A. Herman and H. Sitter. *Springer Series in Material Science, Springer Verlag*, 1996.

[Hert 11a] M. den Hertog, M. Elouneg-Jamroz, E. Bellet-Amalric, S. Bounouar, C. Bougerol, R. Andr, Y. Genuist, J. Poizat, K. Kheng, and S. Tatarenko. *Journal of Crystal Growth*, Vol. 323, pp. 330 – 333, 2011.

[Hert 11b] M. den Hertog, M. Elouneg-Jamroz, E. Bellet-Amalric, S. Bounouar, C. Bougerol, R. Andr, Y. Genuist, J. Poizat, K. Kheng, and S. Tatarenko. *Journal of Applied Physics*, Vol. 110, No. 034318, pp. 1 – 9, 2011.

[Hoch 05] A. Hochbaum, R. Fan, R. He, and P. Yang. *Nano Letters*, Vol. 5, No. 3, pp. 457 – 460, 2005.

[Hoch 10] A. I. Hochbaum and P. D. Yang. *Chemical Reviews*, Vol. 110, pp. 527 – 546, 2010.

[Holl 95] A. F. Holleman, E. Wiberg, and N. Wiberg. *de Gruyter*, 1995.

[Huan 01] Y. Huang, X. Duan, Y. Cui, L. J. Lauhon, K.-H. Kim, and C. M. Lieber. *Science*, Vol. 294, No. 5545, pp. 1313 – 1317, 2001.

[Jian 07] Y. Jiang, W. J. Zhang, J. S. Jie, X. M. Meng, X. Fan, and S. T. Lee. *Advanced Functional Materials*, Vol. 17, pp. 1795 – 1800, 2007.

[Jie 06] J. S. Jie, W. J. Zhang, Y. Jiang, X. M. Meng, Y. Q. Li, and S. T. Lee. *Nano Letters*, Vol. 6, No. 9, pp. 1887 – 1892, 2006.

[Jie 10] J. S. Jie, W. J. Zhang, I. Bello, C. S. Lee, and S. T. Lee. *Nano Today*, Vol. 5, pp. 313 – 336, 2010.

[Jo 03] S. H. Jo, J. Y. Lao, Z. F. Ren, R. A. Farrer, T. Baldacchini, and J. T. Fourkas. *Applied Physics Letters*, Vol. 83, No. 23, pp. 4821 – 4823, 2003.

[Juli 79] P. M. Julien-Pouzol, S. Jaulmes, M. Guittard, and F. Alapini. *Acta Cryst.*, Vol. B35, pp. 2848 – 2851, 1979.

[Kali 00] P. K. Kalita, B. K. Sarma, and H. L. Das. *Bulletin Materials Science*, Vol. 23, No. 4, pp. 313 – 317, 2000.

[Keem 04] K. Keem, H. Kim, G. T. Kim, J. S. Lee, B. Min, K. Cho, M. Y. Sung, and S. Kim. *Applied Physics Letters*, Vol. 84, No. 22, pp. 4376 – 4378, 2004.

[Kess 12] M. Kessel. *Masterarbeit, Universität Würzburg*, 2012.

[Kim 00] T.-J. Kim and P. H. Holloway. *Noyes Publications/William Andrew Publishing*, 2000.

[Kim 04] H. M. Kim, Y. H. Cho, H. lee, S. I. Kim, S. R. Ryu, D. Y. Kim, T. W. Kang, and K. S. Chung. *Nano Letters*, Vol. 4, No. 6, pp. 1059 – 1062, 2004.

[Kind 02] H. Kind, H. Q. Yan, B. Messer, M. Law, and P. Yang. *Advanced Materials*, Vol. 14, No. 2, pp. 158 – 160, 2002.

[Kitt 05] C. Kittel. *Oldenburg*, Vol. 14, 2005.

[Knen 04] R. Knenkamp, R. Word, and C. Schlegel. *Applied Physics Letters*, Vol. 85, No. 24, pp. 6004 – 6006, 2004.

[Kone 04] R. Konenkamp, R. C. Word, and C. Schlegel. *Applied Physics Letters*, Vol. 85, No. 24, pp. 6004 – 6006, 2004.

[Kusc 14] P. Kusch, E. Grelich, C. Somaschini, E. Luna, M. R. ans L. Geelhaar, H. Riechert, and S. Reich. *Physical Review B*, Vol. 89, No. 045310, pp. 1 – 5, 2014.

[L Kr 31] R. d. L. Kronig and W. G. Penney. *Proceedings of the Royal Society London A*, Vol. 130, pp. 499 – 513, 1931.

[Lauh 02] L. J. Lauhon, M. S. Gudiksen, D. Wang, and C. M. Lieber. *Nature*, Vol. 420, pp. 57 – 61, 2002.

[Lee 02] C. J. Lee, T. J. Lee, S. C. Lyu, Y. Zhang, H. Ruh, and H. J. Lee. *Applied Physics Letters*, Vol. 81, No. 19, pp. 3648 – 3650, 2002.

[Li 03] D. Li, Y. Wu, R. Fan, P. Yang, and A. Majumdar. *Applied Physics Letters*, Vol. 83, No. 15, pp. 3186 – 3188, 2003.

[Li 04] Q. Li, X. Gong, C. Wang, J. Wang, K. Ip, and S. Hark. *Advances Materials*, Vol. 16, No. 16, 2004.

[Li 06] Y. Li, F. Qian, J. Xiang, and C. M. Lieber. *Materials Today*, Vol. 9, No. 10, pp. 18 – 27, 2006.

[Liu 95] L. Liu, G. Lindauer, W. B. Alexander, and P. H. Holloway. *Journal of Vacuum Science and Technology B*, Vol. 13, p. 2238, 1995.

[Long 98] M. Longo, N. Lovergine, A. M. Mancini, A. Passaseo, G. Leo, M. Mazzer, M. Berti, and A. V. Drigo. *Applied Physics Letters*, Vol. 72, No. 3, pp. 359–361, 1998.

[Lope 95] M. Lopez. *Journal of Crystal Growth*, Vol. 150, pp. 68 – 72, 1995.

[Lu 05] W. Lu, J. Xiang, B. P. Timko, Y. Wu, and C. M. Lieber. *Proceedings of National Academy of Science of the united States of America*, Vol. 102, No. 29, pp. 10046 – 10051, 2005.

[Lu 06] W. Lu and C. M. Lieber. *Journal of Physics D: Applied Physics*, Vol. 39, No. 21, pp. R387 – R406, 2006.

[Maha 07] S. Mahapatra, K. Brunner, and C. Bougerol. *Applied Physics Letters*, Vol. 91, No. 153110, pp. 1 – 3, 2007.

[Mart 04] T. Martensson, P. Carlberg, M. Borgstrm, L. Montelius, W. Seifert, and L. Samuelson. *Nano Lett.*, Vol. 4, No. 4, pp. 699 – 702, 2004.

[Mass 86] T. B. Massalski, L. J. Murray, and L. H. Bennett. *Ed American Society for Metals*, 1986.

[Mess 09] M. E. Messing, K. Hillerich, J. Johansson, K. Deppert, and K. A. Dick. *Gold Bulletin*, Vol. 42, No. 3, pp. 172 – 181, 2009.

[Miro 02] S. B. Mirov, V. V. Fedorov, K. Grahaw, I. S. Moskalev, V. V. Badikov, and V. Panyutin. *Optics. Letters*, Vol. 27, No. 11, pp. 909 – 911, 2002.

[Miya 92] T. Miyajima, H. Okuyama, and K. Akimoto. *Japanese Journal of Applied Physics*, Vol. 31, No. 12B, pp. L1743–L1745, 1992.

[Moor 90] W. J. Moore. *de Gruyter*, 1990.

[Mura 94] M. Murayama and T. Nakayama. *Physical Review B*, Vol. 49, No. 7, pp. 4710 – 4724, 1994.

[Nguy 10] T. D. Nguyen, J. M. Nagarah, Y. Qi, S. S. Nonnenmann, A. V. Morozov, S. Li, C. B. Arnold, and M. C. McAlpine. *Nano Letters*, Vol. 10, pp. 4595 – 4599, 2010.

[Nirm 99] M. Nirmal and L. Brus. *Accounts of Chemical Research*, Vol. 32, pp. 407 – 414, 1999.

[Owen 45] E. A. Owen and E. A. O. Roberts. *Journal of the Institute of Metals*, Vol. 71, p. 213, 1945.

[Park 04] W. I. Park and G. C. Yi. *Advanced Materials*, Vol. 16, No. 1, pp. 87 – 90, 2004.

[Park 05] J. Y. Park, Y. S. Yun, Y. S. Hong, H. Oh, J. J. Kim, and S. S. Kim. *Applied Physics Letters*, Vol. 87, No. 123108, pp. 1 –3, 2005.

[Pato 05] F. Patolsky and C. M. Lieber. *materialstoday*, Vol. 8, No. 4, pp. 20 – 28, 2005.

[Patt 03] B. Patton, W. Langbein, and U. Woggon. *Physical Review B*, Vol. 68, No. 125316, pp. 1 – 9, 2003.

[Pers 04] A. I. Persson, M. Larsson, S. Stenstrm, B. Ohlsson, L. Samuelson, and L. Wallenberg. *Nature Materials*, Vol. 3, pp. 677 – 681, 2004.

[Phil 06] U. Philipose, T. Xu, P. Sun, H. E. Ruda, Y. Q. Wang, and K. L. Kavanagh. *Journal of Applied Physics*, Vol. 100, No. 084316, pp. 1 – 6, 2006.

[Phil 08] U. Philipose, A. Saxena, H. E. Ruda, P. J. Simpson, Y. Q. Wang, and K. L. Kavanagh. *Nanotechnology*, Vol. 19, No. 215715, pp. 1 – 6, 2008.

[Qian 04] F. Qian, Y. Li, S. Gradecak, D. Wang, C. J. Barrelet, and C. M. Lieber. *Nano Lett.*, Vol. 4, No. 10, pp. 1975 – 1979, 2004.

[Qian 05] F. Qian, S. Gradecak, Y. Li, C. Y. Wen, and C. M. Lieber. *Nano Letters*, Vol. 5, No. 11, pp. 2287 – 2291, 2005.

[R Ja 07] J. M. anf R. Jalilian, G. U. Sumanasekera, and F. P. Zamborini. *Small*, Vol. 3, No. 5, pp. 722 – 756, 2007.

[Sari 02] D. Sarigiannis, J. D. Peck, G. Kioseoglou, A. Petrou, and T. J. Mountiziaris. *Applied Physics Letters*, Vol. 80, No. 21, pp. 4024 – 4026, 2002.

[Schw 99] K. W. Schwarz and J. Tersoff. *Physical Review Letters*, Vol. 102, No. 206101, pp. 1 – 4, 2099.

[Sega 67] B. Segall and D. T. F. Marple. *North-Holland Publishing Company*, 1967.

[Shib 88] N. Shibata, A. Ohki, and A. Katsui. *Journal of Crystal Growth*, Vol. 93, pp. 703 – 707, 1988.

[Slob 03] A. Slobodskyy, C. G. G. Slobodskyy, C. R. Becker, G. Schmidt, and L. Molenkamp. *Physical Review Letters*, Vol. 90, No. 24, pp. 246601–1 – 246601–4, 2003.

[Swan 69] R. K. Swank, M. Aven, and J. Devine. *Journal of Applied Physics*, Vol. 40, No. 1, pp. 89–97, 1969.

[Sze 69] S. M. Sze. *John Wiley Sons*, 1969.

[Tafr 97] M. J. Tafreshi, K. Balakrishma, and R. Dhansekaran. *Journal of Materials Science*, Vol. 32, pp. 3517 – 3521, 1997.

[Tche 06] M. Tchernycheva, J. C. Harmand, G. Patriarche, L. Travers, and G. E. Cirlin. *Nanotechnology*, Vol. 17, pp. 4025 – 4030, 2006.

[Thel 03] C. Thelander, T. Martensson, M. T. Bjork, B. J. Ohlsson, M. W. Larsson, L. R. Wallenberg, and L. Samuelson. *Applied Physics Letters*, Vol. 83, No. 10, pp. 2052 – 2054, 2003.

[Thel 05] C. Thelander, H. A. Nilsson, L. E. Jensen, and L. Samuelson. *Nano Letters*, Vol. 5, No. 4, pp. 635 – 638, 2005.

[Thel 06] C. Thelander, P. Agarwal, S. Brongersma, J. Eymery, L. F. Feiner, A. Forchel, M. Scheffler, W. Riess, B. J. Ohlsson, U. Gsele, and L. Samuelson. *Materials Today*, Vol. 9, No. 10, pp. 28 – 35, 2006.

[Tian 07] B. Z. Tian, X. L. Zheng, T. J. Kempa, Y. Fang, N. F. Yu, G. H. Yu, J. L. Huang, and C. M. Lieber. *Nature*, Vol. 449, pp. 885 – 890, 2007.

[Treu 75] R. G. Treuting and S. M. Arnold. *Acta Metallurgia*, Vol. 5, No. 598, 1975.

[Trib 08] A. Tribu, G. Sallen, T. Aichele, R. Andr, J. P. Poizat, C. Bougerol, S. Tatarenko, and K. Kheng. *Nano Letters*, Vol. 8, No. 12, pp. 4326 – 4329, 2008.

[Trib 09] A. Tribu, G. Sallen, T. Aichele, C. Bougerol, R. Andr, J. P. Poizat, S. Tatarenko, and K. Kheng. *Physica Status Solidi B*, Vol. 246, No. 4, pp. 846 – 849, 2009.

[Voor 85] P. W. Voorhees. *Journal of Statistical Physics*, Vol. 38, pp. 231 – 252, 1985.

[Wagn 64] R. S. Wagner and W. C. Ellis. *Applied Physics Letters*, Vol. 4, No. 5, pp. 89 – 90, 1964.

[Wan 04] Q. Wan, Q. H. Li, Y. J. Chen, T. H. Wang, X. L. He, J. P. Li, and C. L. Lin. *Applied Physics Letters.*, Vol. 84, No. 18, pp. 3654 – 3656, 2004.

[Wang 05] H. T. Wang, B. S. Kang, F. Ren, L. C. Tien, P. W. Sadik, D. P. Norton, S. J. Pearton, and L. Lin. *Applied Physics Letters*, Vol. 86, No. 243503, pp. 1 –3, 2005.

[Wang 07] Y. Q. Wang, U. Philipose, T. Xu, H. E. Ruda, and K. L. Kavanagh. *Semiconductor Science and Technology*, Vol. 22, pp. 175 – 178, 2007.

[Wang 09] M. C. Wang and B. D. Gates. *Materials Today*, Vol. 12, No. 5, pp. 34 – 43, 2009.

[Wu 10] D. Wu, Y. Jiang, L. Wang, S. Y. Li, B. Wu, X. Z. Lan, Y. Q. Yu, C. Y. Wu, Z. B. Wang, and J. Jie. *Applied Physics Letters*, Vol. 96, No. 123118, pp. 1 – 3, 2010.

[Xu 12] H. Xu, Y. Guo, W. Sun, Z. Liao, T. Burgess, H. Lu, Q. Gao, H. H. Tan, C. Jagadish, and J. Zou. *Nanoscale Research Letters*, Vol. 7, No. 589, pp. 1 – 6, 2012.

[Yan 11] H. Yan, H. S. Choe, S. W. Nam, Y. J. Hu, S. Das, J. F. Klemic, J. C. Ellenbogen, and C. M. Lieber. *Nature*, Vol. 470, pp. 240 – 244, 2011.

[Yang 94] K. Yang, L. J. Schowalter, and T. Thundat. *Applied Physics Letters*, Vol. 64, No. 13, pp. 1641–1643, 1994.

[Yone 84] K. Yoneda, Y. Hishida, T. Toda, H. Ishii, and T. Niina. *Applied Physics Letters*, Vol. 45, pp. 1300 – 1302, 1984.

[Zann 14] V. Zannier, V. Grillo, F. Martelli, J. R. Plaisier, A. Lausi, and S. Rubini. *Nanoscale*, Vol. 6, pp. 8392 – 8399, 2014.

Publication

S. Bieker, R. Pfeuffer, T. Kiessling, N. Tarakina, C. Schumacher, W. Ossau, G.Karczweski and L. W. Molenkamp *Polytypism and band alignment in ZnSe nanowires revealed by photoluminescence spectroscopy of embedded (Zn,Cd)Se quantum dots*, Physical Review B 91, 125301 (2015).

Danksagung

An dieser Stelle danke ich allen, die mich während meiner Promotionszeit begleitet haben und mich in jeglicher Art und Weise unterstützt haben.

Als erstes möchte ich mich bei Prof. Dr. Laurens W. Molenkamp bedanken, für die Möglichkeit diese Dissertation am Lehrstuhl Experimentelle Physik III durchzuführen, sowie für Hilfestellungen, Diskussionen und die Bereitstellung der Infrastruktur für mein Projekt.

Außerdem möchte ich mich bei PD. Dr. Charles Gould für die Betreuung des Projekts und die zahlreichen Diskussionen und Ratschläge bedanken.

Ganz besonders möchte ich mich bei Prof. Dr. Grzegorz Karczweski bedanken für seine Unterstützung in jeglicher Hinsicht sowie für die zahlreichen Denkanstöße, Diskussionen und Erklärungen, von denen ich im Laufe der letzten Jahren profitieren durfte.

Vielen Dank an Dr. Claus Schuhmacher der immer ein offenes Ohr hatte und mir mit Rat und Tat zur Seite stand.

Danke an die Mitglieder der MBE Arbeitsgruppe - Chritopher Ames, Felicitas Gerhard, Maximillian Kessel, Philipp Leubner, Christoph Pohl, Raimund Schlereth, Steffen Schreyeck, Mirko Trabel, Martin Winnerlein und alle Diplomanden, Masteranden und Bachelors - für die gute Zusammenarbeit, das hervorragende Arbeitsklima bei jeder auch noch so mühsamen Arbeit und für die zahlreichen hilfreichen Gespräche und Anregungen.

Danke an die Spintronics Arbeitsgruppe für die Hilfe bei der Lithographie und elektronischen Charakterisierung und danke an die Optik Arbeitsgruppe für die optische Charakterisierung meiner Proben und die zahlreichen Diskussionen.

Ein herzliches Dankeschön an Petra Wolf-Müller, Jana Hinterberger, Carmen Bundschuh, Volkmar Hock und Martin Zipf für eure Hilfe bei jeglichen Problemen in der MBE oder im Reinraum. Ohne euch wäre diese Arbeit nicht zustande gekommen.

Für die einzigartige Atmosphäre im Büroalltag möchte ich meinen Kollegen Holger Thirschmann und Philipp Leubner danken.

Danke Feli, Danke Tsveti, Danke Gracy für eure Freundschaft und Unterstützung im-

mer wieder einen klaren Kopf zu bewahren.

Danke auch an alle anderen EP3ler für die hervorragende Zusammenarbeit.

Ein besondere Dank gilt meinen Freunden ausßerhalb der Physik und meinem Freund Matthias Schirmer für die emotionale Unterstützung. Ihr habt mich auf andere Gedanken gebracht und mir die Augen geöffnet für die wirklich wichtigen Dinge außerhalb der Physik. Danke, dass es euch gibt.

Herzlich bedanke ich mich bei meinen Eltern, Gudrun und Josef Pfeuffer, und meinem Bruder, Sebastian Pfeuffer, die alle ihren eigenen, ganz besonderen und wichtigen Teil zu meiner Arbeit beigetragen haben und mich in jeder Hinsicht zu jeder Zeit unterstützt haben und mir mit Rat und Tat zur Seite standen.